博士論文

Indications of Muon Neutrino Oscillation in a 250km Long Baseline Experiment (250km 長基線実験における ミューオンニュートリノ振動の示唆)

平成15年1月

神戸大学大学院自然科学研究科

岩下 大器

Taiki IWASHITA

Abstract

K2K is a long-baseline neutrino oscillation experiment extending from KEK, the high energy accelerator research organization in Ibaraki prefecture, to Kamioka. K2K is the first long-baseline neutrino oscillation experiment in the world to use an accelerator. It was designed to confirm the presence of muon neutrino oscillation observed in the Super-Kamiokande collaboration. It also aims to quantitatively measure the oscillation parameters Δm^2 and $\sin^2 2\theta$. In this thesis, the first result of spectrum analysis of neutrino oscillation three years into the K2K experiment is reported.

The K2K neutrino beam is produced with a 12 GeV proton synchrotron. Numerous beam monitors along the beam line measure beam intensity and direction. Near and far detectors along the beam are used to compare neutrino flux at two points. The near detector is 300m downstream from the target. It measures the neutrino spectrum and the number of neutrino events directly after neutrino production. It consists of the 1kt water Čerenkov detector and the fine grain detector (FGD) system. We have constructed a scintillating fiber (SciFi) detector as the main component of the FGD. The far detector, Super-Kamiokande (SK), is 250km downstream from the target. Neutrino oscillation is observed as a reduction of muon neutrino flux and the distortion of the energy spectrum at far detector. K2K's sensitive region is $\sin^2 2\theta \sim 1$, $\Delta m^2 \sim 10^{-2}$ to $10^{-3} eV^2$ for $\nu_\mu \rightarrow \nu_\tau$. Analysis of atmospheric neutrinos at SK (1144 day exposure) suggests the allowed region is $\sin^2 2\theta \sim 1$ and $\Delta m^2 \sim 10^{-3} \sim 5 \times 10^{-3} eV^2$ for $\nu_\mu \rightarrow \nu_\tau$ mode.

The analysis and results in this thesis were obtained using the SciFi detector, one of the most important components of the near detector. The SciFi detector is a tracker made of scintillating fibers, consisting of 20 layers of fiber sheets interspersed with 19 layers of water target. IITs (image intensifier tubes) intensify the track information on secondary charged particles from neutrino interaction. CCD cameras record this information. This thesis develops and describes anal-

ysis techniques to reconstruct tracks from CCD camera images. With the track information from the SciFi detector and downstream detectors, 12317 neutrino events captured by the K2K SciFi detector over a three year period were reconstructed. Combining the SciFi data with the 1kt water Čerenkov detector data, a view of the neutrino energy spectrum at the near detector was obtained.

Fifty six beam neutrino events at SK were observed. With an expectation of $80.1^{+6.2}_{-5.4}$ events at the near detector assuming no oscillation, the result indicates the probability of no oscillation is less than one percent. Additionally, a maximum likelihood analysis using spectrum shape was performed. Twenty-nine one-ring muon type events were used to reconstruct neutrino energy. In a two-flavor oscillation framework, the allowed region of Δm^2 is between 1.5×10^{-3} and 3.9×10^{-3} eV^2 at 90% C.L. at $\sin^2 2\theta = 1.0$, which is consistent with the results of the SK collaboration using atmospheric neutrinos.

Acknowledgements

First I would like to express my deepest appreciation to the initiators of this K2K experiment, Professor Koichiro Nishikawa at Kyoto University and Professor Kenzo Nakamura at KEK. Thank you for allowing me to participate.

I am also grateful to Prof. T. Hara, Prof. S. Aoki, and Dr. A. C. Suzuki, who offered guidance to me as an undergraduate at Kobe University. I would not have been able to undertake this project without their help.

I was fortunate to work alongside Prof. M. Sakuda and Dr. T. Ishida at KEK during the construction, operation and analysis phases of the SciFi detector project. I am grateful for the opportunity to share their challenges, their concerns, and their aspirations. The body of this thesis comes from work undertaken in cooperation with them.

I give special thanks to Dr. Y. Hayato at KEK. His work on the electronics at SciFi is indispensable.

Dr. H. Park and Dr. S. Boyd, and Dr. H. Ishino as PostDoc at KEK, Dr. B.J. Kim from Seoul National University, and Ms. H. Yokoyama from Tokyo University of Science (SUT) all made great contribution for the analysis software.

Acknowledgements go out to Mr. S. Echigo, Mr. K. Tashiro and Mr. M. Kitamura at Kobe University for preparing me to take on the challenge of this work. I must mention the SciFi construction and maintenance work carried out by Mr. M. Onchi, Mr. K. Sato, Mr. G. Kume, Mr. K. Takenaka, Mr. K. Fujii and Mr. Y. Tanaka, all from Kobe University, Dr. T. Kadowaki and Mr. S. Kishi from SUT, and Dr. S. Matsuno from the University of Hawaii. I will never forget the time we spent together.

Ms. E. J. Jeon from the Graduate University for Advanced Studies, Ms. U. Golebiewska from Warsaw University, Prof. C. W. Walter and Prof. E. Kearns from Boston University, Dr. E. Sharkey from Stony Brook University New York (SUNY) all worked alongside me on the SciFi detector.

Numerous people made my stay at KEK a happy and pleasant one. I give

special thanks to Dr. A. Sakai at KEK (now with Fujitsu Ltd.), Dr. T. Maruyama from Tohoku University (now at Chicago University.), Dr. M. Kohama from Kobe University (now with Riken), Dr. M. Yoshida at KEK, Dr. T. Inagaki from Kyoto University (now at SPring-8), Mr. J. H. Choi from Chonnam National University, Mr. M. Nakamura from Niigata University, Mr. H. Maesaka, Mr. S. Mukai, and Mr. A. Shima from Kyoto University.

If this thesis is a good one, it is due to the help of the following people: Dr. T. Hasegawa from Tohoku University and Dr. J. Hill from SUNY, who worked hard to provide a stable neutrino beam; Prof. T. Kobayashi, Dr. Y. Oyama, and Dr. T. Ishii at KEK, who operated and led analysis at the near detector; Prof. T. Nakaya, Mr. I. Kato from Kyoto University, Dr. S. Mine from the University of California, and Dr. C. Mauger from SUNY, who kindly allowed me to use data from the 1kton Čerenkov detector; Prof. Y. Totsuka, Prof. Y. Suzuki, Prof. T. Kajita, Prof. K. Kaneyuki, Prof. M. Nakahata, Prof. Y. Itow, Dr. J. Kameda, Dr. M. Miura, Mr. S. Nakayama, Mr. S. Yamada, and Dr. Y. Obayashi at Super-Kamiokande , who graciously allowed me to conduct a neutrino oscillation analysis. Thank you all so much.

I also thank Ms. T. Otaki, Ms. M. Takatsuki, Mr. S. Nishiyama, Mr. S. Noda, Mr. Y. Suga, Mr. F. Nakata, and Ms. M. Sekiguchi, all from Kobe University.

My deepest gratitude goes out to Prof. H. Takeda, and Prof. M. Nozaki at Kobe University, who introduced me to the beautiful world of the elementary particle.

Finally, I wish to thank my family for their support over the past three years.

Thank you all so very much.

Contents

List of Figures

List of Tables

Chapter 1

Introduction

1.1 The Neutrino in the Last Century

1.1.1 Neutrino Mass

The neutrino is one of the most remarkable particles in current high energy physics. It is a neutral lepton of zero or very small mass.

In 1930, W. Pauli [1] postulated the existence of a very light neutral particle with spin 1/2 as a solution to the problem of the continuous energy spectrum of the electron from β-decay $n \rightarrow p + e^-$. In 1956, F. Reines and C. Cowan [2] showed direct evidence of neutrino existence from the inverse β-decay, $\bar{\nu_e} + p \rightarrow e^+ + n$. Neutrinos have the same generations as the charged leptons: the electron, the muon, and the tauon. These are called electron-neutrino (ν_e), muon-neutrino (ν_μ), and tau-neutrino(ν_τ), respectively.

Neutrino mass has been a mystery for a long time. The modern standard model [3, 4, 5] assumes that neutrinos have no mass, given that even if they did it would be very small. Though there is no basis for this assumption, this standard model explains observations very well.

Meanwhile, the investigation into neutrino mass has continued. The most sensitive experiment for ν_e mass uses β-decay of Tritium [6]:

$$ {}^3_1\mathrm{H} \rightarrow {}^3_2\mathrm{He} + \mathrm{e}^- + \bar{\nu}_\mathrm{e} \tag{1.1} $$

If $\bar{\nu_e}$ has a finite mass, the end point of the electron energy spectrum shifts from that calculated, assuming ν_e mass is 0. The current upper limit on the mass of ν_e adopted by Particle Data Group (PDG) [12] is 3 eV.

Table 1.1: Current mass limits for three types of neutrino by PDG [11]

Flavor	Mass limit	Experiment
ν_e	3 eV	Tritium β decay
ν_μ	190 keV(90% C.L.)	Pion decay at rest
ν_τ	18.2 MeV(95% C.L.)	Tau decay in e^+e^- collider

For ν_μ, momentum measurements of muon from pion decay at rest

$$\pi \rightarrow \mu + \nu_\mu \tag{1.2}$$

give the best mass limit [7]. PDG's value is 190keV.

For ν_τ, the best limit is 18.2 MeV, which is obtained from kinematics of tauon decay in ALEPH [8]:

$$\tau \rightarrow 2\pi^-\pi^+\nu_\tau \tag{1.3}$$

$$\tau \rightarrow 3\pi^-2\pi^+\pi^0\nu_\tau. \tag{1.4}$$

The current mass limits for the three types of neutrino are summarized in Table 1.1.

1.1.2 Neutrino Oscillation

Neutrino oscillation is a means of studying the small mass of neutrinos and their mixing [9, 10]. Here is an example of two-flavor neutrino oscillation.

We assume ν_e and ν_μ have finite and different masses and mix with angle θ between weak and mass eigenstates. We can get

$$\begin{pmatrix} \nu_e \\ \nu_\mu \end{pmatrix} = \begin{pmatrix} \cos\theta & \sin\theta \\ -\sin\theta & \cos\theta \end{pmatrix} \begin{pmatrix} \nu_1 \\ \nu_2 \end{pmatrix}, \tag{1.5}$$

where $\nu_l = (\nu_e, \nu_\mu)$, $\nu_i = (\nu_1, \nu_2)$ are the weak and mass eigenstates, respectively. This can be written simply:

$$|\nu_l> = U_{li}|\nu_i>, \tag{1.6}$$

where

$$U \equiv \begin{pmatrix} \cos\theta & \sin\theta \\ -\sin\theta & \cos\theta \end{pmatrix}. \tag{1.7}$$

The neutrino beam generated as a weak eigenstate, $|\nu_l>$, is evolved in time as

$$|\nu_l(t)>=\sum_i U_{li}e^{-iE_it}|\nu_i>,\ =\sum_i\sum_{l'}U_{li}U_{l'i}e^{-iE_it}|\nu_{l'}> \tag{1.8}$$

after time t. We use the approximation

$$E_i = p + \frac{m_i^2}{2p}. \tag{1.9}$$

Oscillation probability of ν_l to $\nu_{l'}$ after t becomes

$$P(\nu_l \to \nu_{l'}) = |<\nu_{l'}|\nu_l(t)>|^2 = \sum_i\sum_{i'}U_{li}U_{l'i}U_{li'}U_{l'i'}\times\cos\left[(E_i-E_{i'})\,t\right]. \tag{1.10}$$

Using distance L $(L=t)$

$$P(\nu_l \to \nu_{l'}) \;=\; \sin^2 2\theta \sin^2\left(\frac{\Delta m^2}{4E}L\right), \tag{1.11}$$

where

$$\Delta m^2 \;=\; m^2_{\nu_2} - m^2_{\nu_1}. \tag{1.12}$$

When we use eV^2, GeV and km as units for Δm^2 , E, and L, the mixing probability is

$$P(\nu_l \to \nu_{l'}) = \sin^2 2\theta\ \sin^2\left(1.27\cdot\frac{\Delta m^2[eV^2]\cdot L[km]}{E[GeV]}\right). \tag{1.13}$$

In a neutrino oscillation experiment, we can measure Δm^2 , and not the neutrino mass directly.

1.1.3 The Atmospheric Neutrino Anomaly

Primary cosmic rays dominated by protons and α particles interact with nuclei in the atmosphere of the earth to produce π mesons and K mesons. π decays like

$$\begin{aligned}\pi &\to \mu + \nu_\mu \\ \mu &\to \mathrm{e} + \nu_\mathrm{e} + \nu_\mu.\end{aligned} \tag{1.14}$$

Neutrinos generated in the atmosphere are called "atmospheric neutrinos." The ratio ν_μ / ν_e should be 2/1 from the reactions in 1.14. Systematic error due to the uncertainty of flux of primary cosmic rays can be reduced from $\sim$ 30% to

Table 1.2: R of atmospheric neutrino for neutrino observatories around the world. "Sub-GeV (Multi-GeV)" indicates events with visible energy less (more) than 1.33 GeV.

Experiment	R(Eqn.1.15)	Citation
Kamiokande(Sub-GeV)	$0.60^{+0.06}_{-0.05} \pm 0.05$	[13]
Kamiokande(Multi-GeV)	$0.57^{+0.08}_{-0.07} \pm 0.07$	[13]
IMB	$0.54 \pm 0.05 \pm 0.07$	[14]
Frejus	$1.00 \pm 0.15 \pm 0.08$	[15]
NUSEX	$0.99^{+0.35}_{-0.25}$	[16]
Soudan2	$0.51^{+0.05}_{-0.07} \pm 0.14$	[17]
SK(Sub-GeV)	$0.635 \pm 0.033 \pm 0.053$	[18]
SK(Multi-GeV)	$0.604^{+0.065}_{-0.58} \pm 0.087$	[18]

5% by by taking the double ratio of the number of observed neutrino and the simulated one:

$$R \equiv \frac{N(\nu_\mu + \bar{\nu}_\mu)/N(\nu_e + \bar{\nu}_e)_{data}}{N(\nu_\mu + \bar{\nu}_\mu)/N(\nu_e + \bar{\nu}_e)_{simulation}} \tag{1.15}$$

Kamiokande found that R was 0.6, meaning that the observed data showed a deficit of $\sim$ 40% [13]. IMB [14], Soudan2 [17], and Super-Kamiokande (SK) [18] also show results consistent with Kamiokande. This deficit is called the "atmospheric neutrino anomaly." Results from neutrino observatories around the world are summarized in Table 1.2. These results suggest that the number of ν_μ is smaller than expected and/or the number of ν_e is larger than expected.

1.1.4 Observation of Atmospheric Neutrino Oscillation by the SK Collaboration

The SK collaboration also observed clear asymmetry between upward-going and downward-going ν_μ s [18]. Distance from the production point to the SK detector varies from $\sim$ 10km to $\sim$ 10^4km, depending on the zenith angle of the flight direction of the neutrinos. If atmospheric ν_μ s oscillate into another type of ν as in Eq. 1.13, the number of events will change along with the zenith angle. Figure 1.1 shows the zenith angle distribution of neutrino events observed in SK, shown with simulation results assuming oscillation and no oscillation.

The distribution was well explained by $\nu_\mu \rightarrow \nu_\tau$ neutrino oscillation where the parameters are $\Delta m^2 = 3.2 \times 10^{-3}\mathrm{eV}^2$ and $\sin^2 2\theta = 1$. The SK collaboration concluded that they had observed neutrino oscillation.

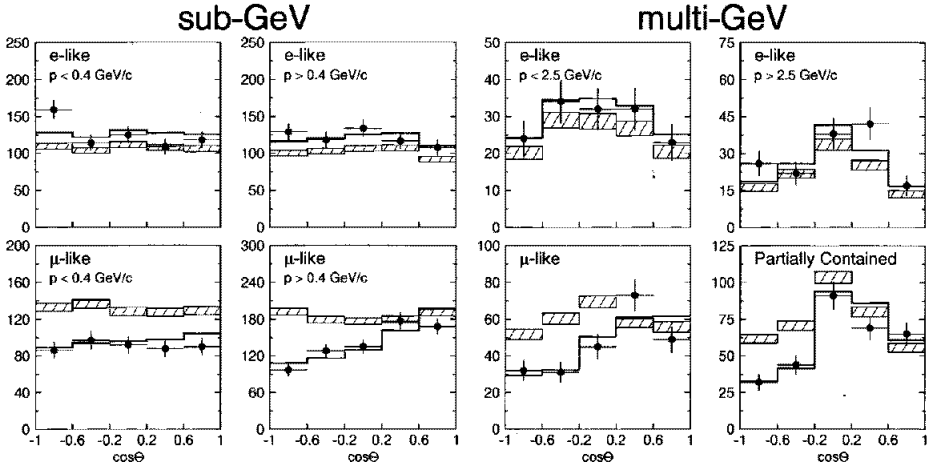

Figure 1.1: The zenith angle distribution of μ-like and e-like events. Observed neutrino events in SK (cross) and simulation assuming oscillation (line) and no oscillation (hatched box). The distribution is well explained by $\nu_\mu \rightarrow \nu_\tau$ neutrino oscillation where the parameter is $\Delta m^2 = 3.2 \times 10^{-3}\mathrm{eV}^2$, $\sin^2 2\theta = 1$. "Sub-GeV (Multi-GeV)" indicates events in which visible energy is less (more) than 1.33 GeV.

1.2 The K2K Experiment

The KEK E362 experiment is colloquially known as K2K (KEK to Kamioka). It is the first long-baseline neutrino oscillation experiment in the world that uses an accelerator. It was approved in 1994. We produce an artificial muon neutrino beam at the KEK 12 GeV proton synchrotron and observe it using the SK neutrino detector at a distance of 250km.

The main purpose of the K2K experiment is to confirm the SK collaboration observation of muon neutrino oscillation. It also aims to quantitatively measure the oscillation parameters, Δm^2 and $\sin^2 2\theta$. The method is as follows:

- If neutrino oscillation occurs, the number of muon events at the far site will

be fewer then the number of events expected in a null-oscillation model.

- In addition, we will observe some distortion of the neutrino energy spectrum because the probability of neutrino oscillation varies according to its energy. Figure 1.2 shows distorted E_ν spectrums at K2K in one Δm^2 case. ($\Delta m^2 = 0.005\text{eV}^2$, $\sin^2 2\theta = 1$)

- For every parameter set (Δm^2 , $\sin^2 2\theta$), the energy spectrum is calculated and compared with the observed one.

- From the likelihood analysis, we determine the allowed region of parameters.

In the K2K experiment, the mean neutrino energy $< E_\nu >$ is 1.4GeV and the distance L is 250km. The sensitive region is $\Delta m^2 \geq 2 \times 10^{-3}\text{eV}^2$, and $\sin^2 2\theta \sim 1$ (Figure 1.3) for $\nu_\mu \rightarrow \nu_\tau$ mode.

1.3 Overview of this thesis

After three years of work on the K2K experiment, this thesis details the first result of spectrum analysis.

An overview of the K2K experiment is described in Chapter 2. The scintillating fiber (SciFi) detector was built to measure the neutrino energy spectrum at the near site.

The construction of the SciFi detector and its hardware setup is discussed in Chapter 3. Chapter 4 explains the neutrino simulation procedure, undertaken to predetermine detector performance and detect systematic errors of measurement prior to an actual run. The analysis technique, as well as neutrino event selection, is described in Chapter 5. Event counting, a summary of error estimation, and a comparison between observation at the far site and the expectations at the near site are described in Chapter 6. Matching simulated data to observed data, we measure the neutrino energy spectrum with the near detectors (including the 1kton detector) in Chapter 7. Chapter 8 details event selection at the far site.

Finally in Chapter 9, using information on the number of events and spectrum shape, we perform a neutrino oscillation analysis.

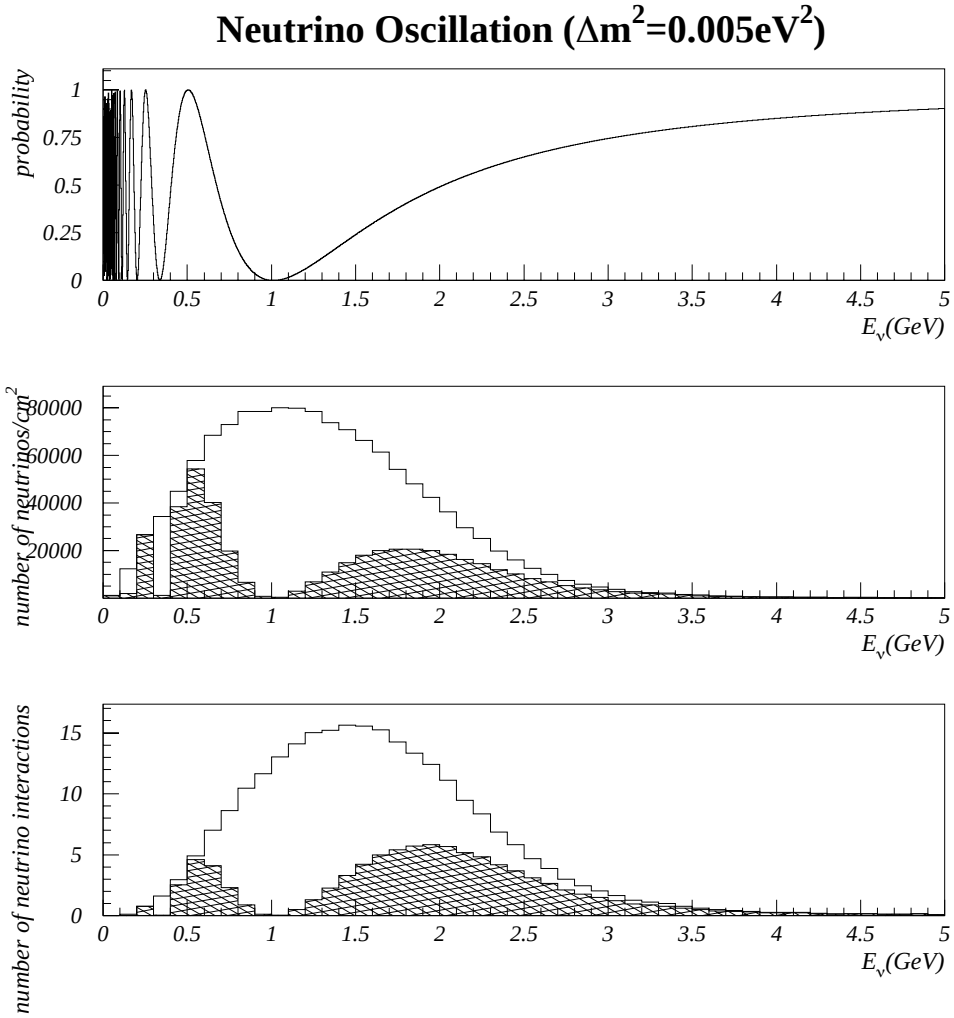

Figure 1.2: Neutrino energy spectrum distortion in K2K in the case of the oscillation at ($\Delta m^2 = 0.005\text{eV}^2$, $\sin^2 2\theta = 1$). The top figure shows the probability of neutrino oscillation as a function of energy. The middle figure shows the neutrino flux at SK. The histogram shows the expected neutrino flux by MC [units are "number of neutrinos/cm^2/10^{20}POT(Protons On Target)"]. The hatched area is the expected flux times the oscillation probability. The bottom figure shows the neutrino flux times the total cross section of neutrino interaction with water, which corresponds to the expected number of events at SK.

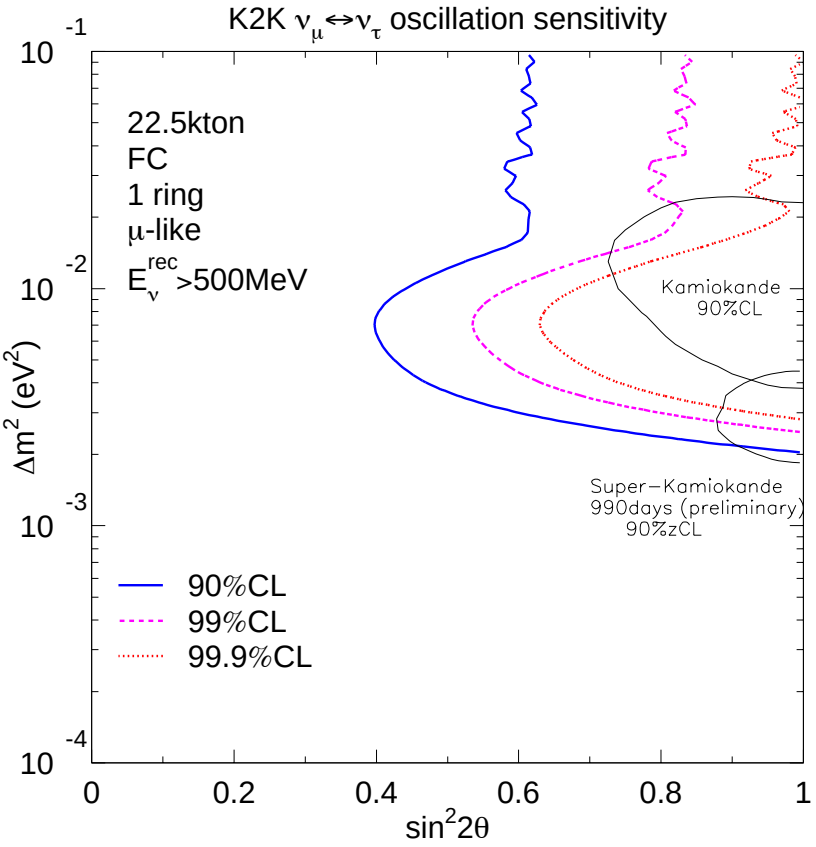

Figure 1.3: Sensitive region of the K2K experiment for $\nu_\mu \rightarrow \nu_\tau$ mode. The right side of three lines correspond 90%, 99%, and 99.9% C.L. Allowed regions of oscillation parameters in Kamiokande and Super-Kamiokande are overlaid.

Chapter 2

Setup of the K2K Experiment

A schematic overview of the K2K experiment is shown in Figure 2.1. The neutrino beam produced by the 12GeV proton synchrotron (PS) (a) travels through the neutrino beam line (b). There are several monitors along the beam line: proton beam line monitors, a pion monitor, and muon monitors. The proton beam line monitors normalize the live time of the detectors and predict neutrino flux. The pion monitor estimates flux ratio at the near and far detectors. The muon monitors measure the direction of the neutrino beam. The neutrino flux at the near detector (c) is measured and compared with that at Super-Kamiokande, the far detector (d). The 12GeV PS, the beam line, and the near detector were constructed on-site at KEK. A GPS system (e) controls targeting and time synchronization between KEK and the far detector.

This chapter describes the components used to conduct the K2K experiment, from upstream to downstream.

2.1 12 GeV Proton Synchrotron

The 12 GeV proton synchrotron (PS) is located at KEK (High Energy Accelerator Research Organization) in Ibaraki Prefecture, Japan. The accelerator consists of a 750keV Cockcroft Walton accelerator, a 40 MeV linac injector, a 500 MeV booster, and the main ring, a 12 GeV synchrotron.

Proton beams are extracted from the "EP1" beam channel in the main ring every 2.2 seconds. This is known as "fast extraction" as all of the protons are kicked out in 1.1μ sec. The typical number of protons per pulse (PPP) is 5.6×10^{12}. There are nine rf packets in the main ring and therefore protons are transported

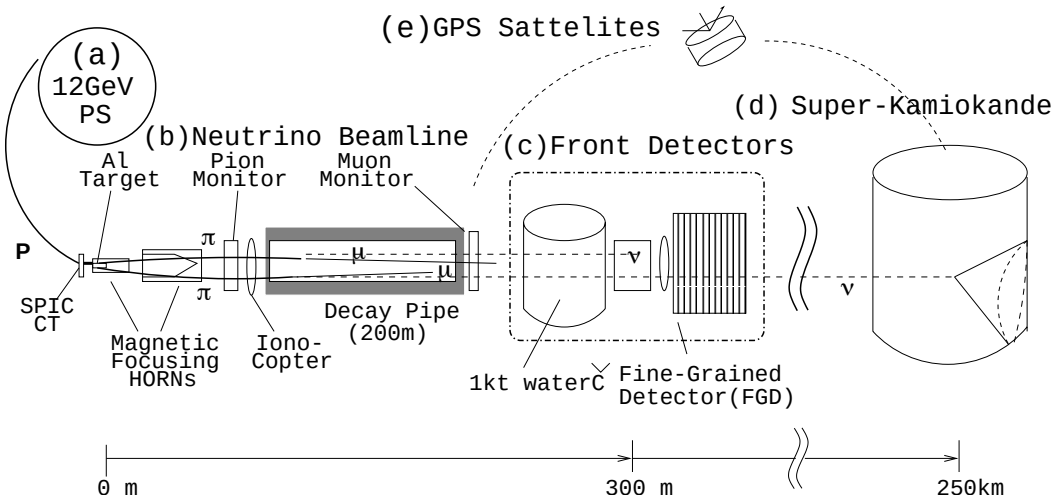

Figure 2.1: Schematic overview of K2K experiment.

to the beam line in nine bunches.

2.2 Proton Beam Line

In 1994, with approval granted for the K2K experiment, the proton beam line was built to extract and bend the primary proton beam in the direction of the far detector.

The arc section of the beam line consists of 18 bending magnets and 18 quadrupoles. The transport efficiency of the beam line is approximately 85%.

2.2.1 Beam Line Monitors

The proton beam line has 13 CTs (current transformers) and 28 SPICs (segmented plates ionization chambers). The CTs are coils sensitive to the beam current. They are used as beam intensity monitors and they determine the absolute number of protons to within 10%. SPICs obtain profiles of the proton beams. A SPIC consists of three 28 μm thick copper sheets. The middle sheet is a cathode plane (-HV). The other two are horizontal and vertical readout (GND) planes. Figure 2.4 shows a schematic view of a SPIC. The readout planes have 32 channels giving x and y readouts. For more detail on the K2K SPICs, please see reference [19].

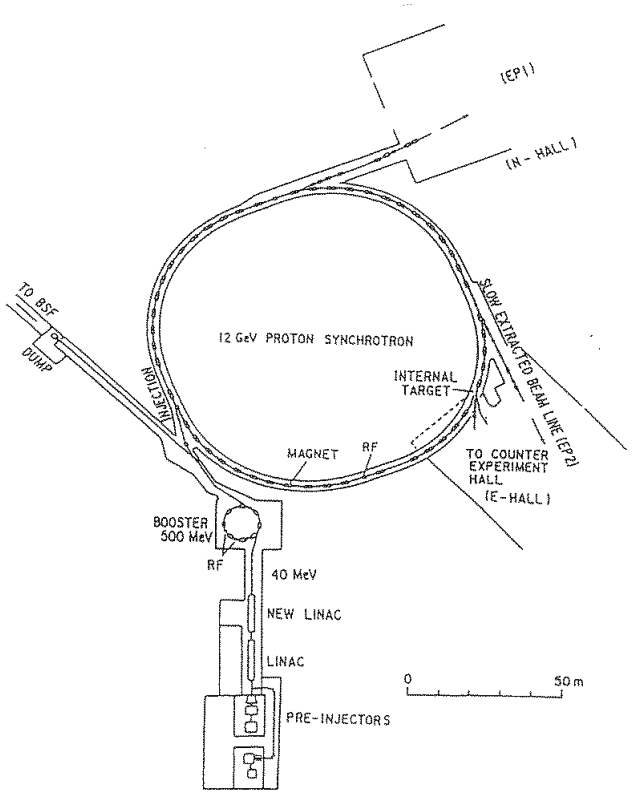

Figure 2.2: KEK-12GeV proton synchrotron consists of a 750keV Cockcroft Walton accelerator, a 40 MeV linac injector, a 500 MeV booster, and a 12GeV main ring.

2.3 Target and Magnetic Horns

The target is made of aluminum. It was 20mm in diameter in June 1999 and 30mm from November 1999. The 66cm length corresponds to a 1.5 interaction length.

The two magnetic horns which focus the pions are also made of aluminum.

The horns are driven every 2.2 seconds with a 2 msec. long 250 kA pulsed current. They need to be synchronized with the fast extracted beam (1.1 μsec. bunch width) to generate toroidal magnetic fields.

Figure 2.5 is a schematic view of the target and magnetic horns. The first horn is 2.5 meters long and 0.60 meters in diameter. The second horn is 2.8 meters long and 1.7 meters in diameter. It is located eight meters downstream

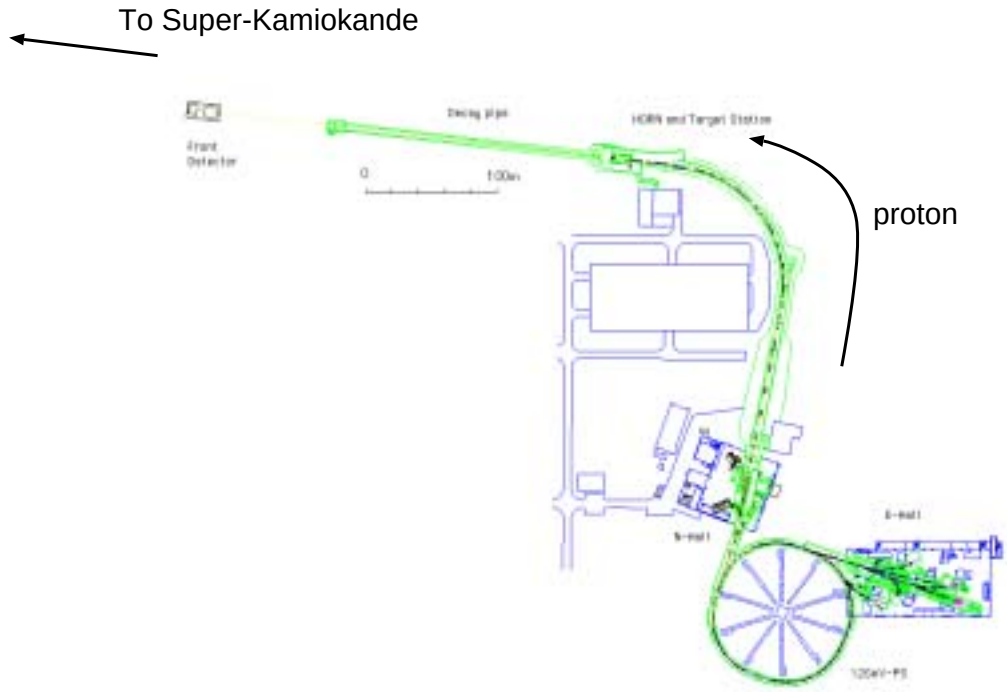

Figure 2.3: Proton beam line.

of the first horn.

The strength of the magnetic field B(kGauss) at R(cm) distance from the beam center is given by;

$$B = \frac{I}{5.0 \cdot R}, \tag{2.1}$$

where I is the current supplied to the horn magnets (kA). According to the calculation, we have 50 kGauss at R = 1cm. Simulated neutrino flux above 0.5 GeV with magnetic horns supplied at 250 kA current is approximately 22 times greater than at 0 kA (Figure 2.6).

Not only the diameter of the target was changed; the current supplied to the magnetic horns was increased from 200 kA to 250 kA. This will be taken into consideration when we analyze the neutrino data.

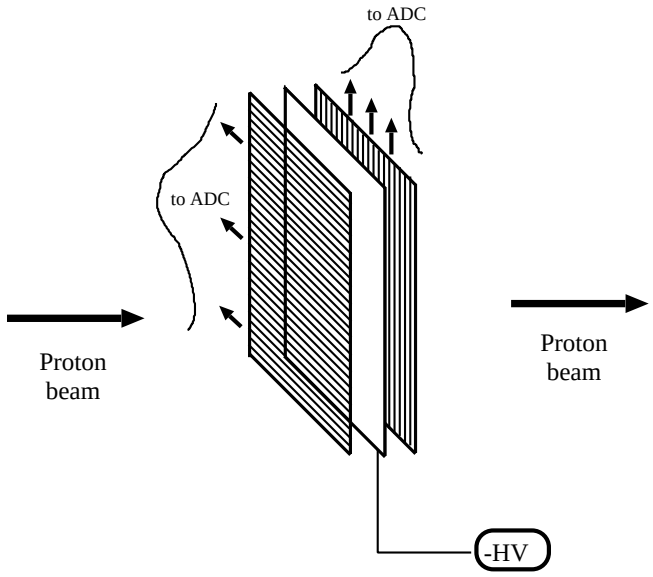

Figure 2.4: Schematic view of a SPIC.

2.4 Secondary Particle Monitors

The pion monitor and muon monitors monitor secondary particles after they pass the target [24]. The pion monitor measures the momentum and the angle of pions immediately after they pass the second horn. The muon monitors measure the intensity and position distribution of muons produced by pion decay.

2.4.1 Pion Monitor

The pion monitor is a gas Čerenkov detector. Charged particles traveling in a medium at a velocity faster than the velocity of light in that medium emit Čerenkov radiation. Photons are emitted in a cone with respect to the direction of the particle. See subsection 4.3.2 for more detail on Čerenkov radiation.

The pion monitor consists of a gas vessel, a pie-shape spherical mirror, and photo detectors (Figure 2.7). Čerenkov radiation emitted in gas reflects off the spherical mirror and is detected by photo detectors. The gas vessel is filled with Freon gas. Increasing the gas pressure from 0.34atm to 1.70atm changes the refractive index of the gas from 1.00047 to 1.00236, which corresponds to a Čerenkov threshold of pions at 4.6GeV/c to 2.0GeV/c. The photo detector is a 20 photomultiplier tube (PMT) array.

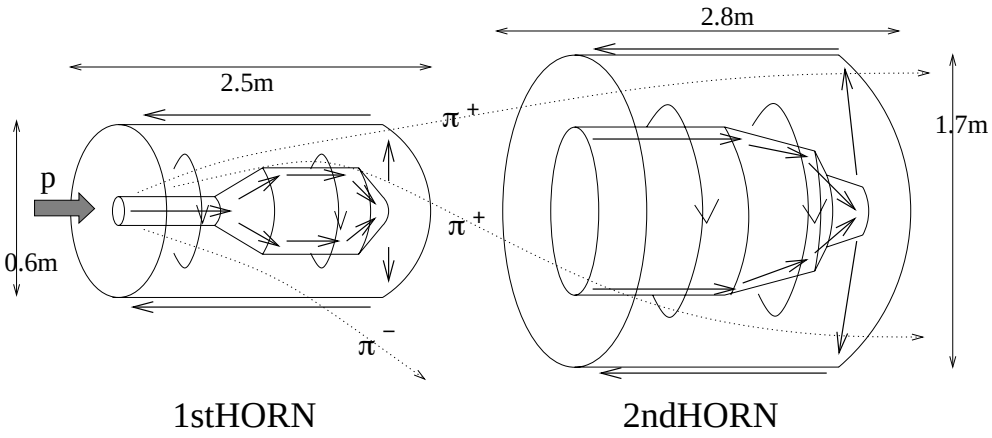

Figure 2.5: Target and magnetic horn. The target is an aluminum rod. Both horns only focus positive pions.

The pion production angle can be measured by detecting Čerenkov light (Figure 2.8). Changing the refractive index of gas, this measurement is taken in several gas refractive index values, from which pion momentum distribution is obtained. With this distribution of pions in P_μ - θ_μ space, we can estimate neutrino flux in the neutrino beam at the near and far detectors [24]. Using this calculated flux ratio, the expected number of events at the far detector can be derived from the number of events at the near detector. (Chapter 6).

Measurements were taken with the pion monitor in June and November 1999. (The pion monitor is not on the beam line during normal neutrino beam runs.)

2.4.2 Muon Monitors

Muon monitors monitor beam direction and stability on a spill-by-spill basis. Since we monitor muons from the reaction $\pi^+ \rightarrow \mu^+ + \nu_\mu$, the profile center of muons is the same as of muon neutrinos.

The muon monitors are 200m downstream of a decay volume filled with He gas. They consist of a silicon pad detector (SPD) and a ionization chamber (Figure 2.9). The SPD has 25 silicon pads. The ionization chamber has 36 and 32 channels for the X and Y readout electrodes, respectively.

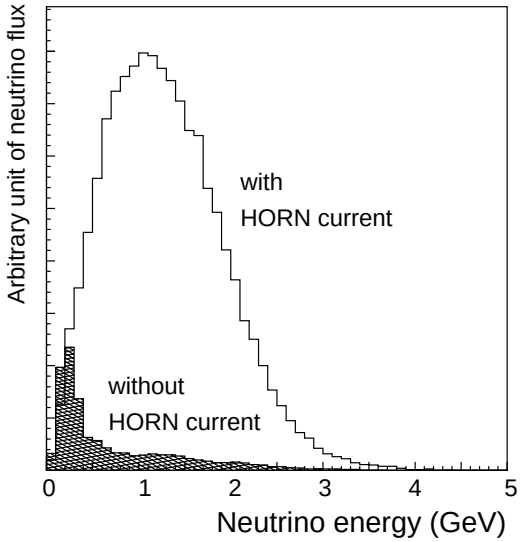

Figure 2.6: Estimated neutrino flux with horn current 0kA and 250kA (simulation). The hatched and white areas correspond to 0kA and 250kA, respectively. 250kA horn current focuses neutrinos 22 times greater than at 0kA.

2.4.3 Beam Line DAQ

CAMAC ADCs convert the data from the beam line monitors into a digital signal, which is then processed by six IBM-PC compatible machines (PCs) connected via a PC-CCP bus interface system [20].

Figure 2.10 shows the beam line DAQ system.

2.5 Near Detectors

The near detectors are located 300m downstream of the target. Figure 2.11 is an overview of the near detectors. The near detector hall is 16m in depth and 24m in diameter. From upstream to downstream, it houses the 1kt water Čerenkov detector, veto counters, the scintillating fiber detector (SciFi detector), trigger counters, lead glass counters (LG), and the muon range detector (MRD).

The near detectors aside from the 1kt are collectively called the fine grain detector (FGD). The 1kt has a high efficiency for muons below 1 GeV/c, and full 4π solid angle coverage, but a low efficiency for muons above 1.5 GeV/c since the muon exits the detector. FGD (which includes SciFi and MRD) has a

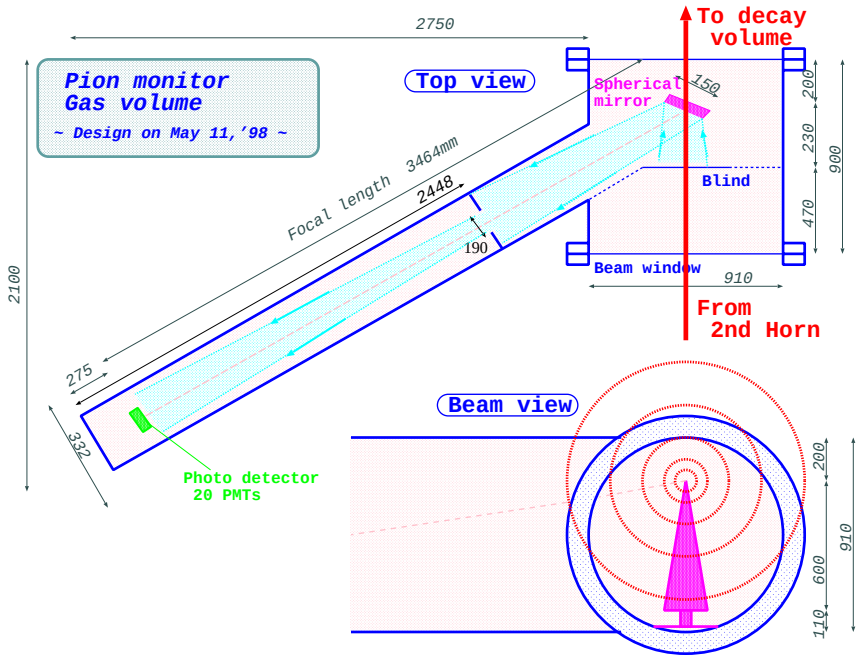

Figure 2.7: Pion monitor.

high efficiency for muons above 1GeV/c, and it has higher resolution of position, providing rich track information around the interaction vertex.

2.5.1 1kton Water Čerenkov Detector (1kt Detector)

The ring image water Čerenkov detector is the most upstream of the near detectors. Čerenkov detectors detect Čerenkov radiation emitted by charged particles traveling in water at a velocity faster than the velocity of light in the water. They are emitted in a cone with respect to particle direction. The analysis technique used for this detector is the same used for the far detector.

The detector is a cylindrical tank 10.8m tall and 10.8m in diameter. It is filled with 1000 tons of pure water, from which it derives the name "1kt". The inner detector (ID) is 8.6m in diameter and 8.6m tall. It surrounded by the outer detector (OD). The ID and the OD are optically separated.

The ID has 680 20-inch PMTs to detect charged particles produced by neutrino interaction. The photo cathode coverage is 40%. The OD vetoes incoming particles; it has 68 eight-inch PMTs.

The 1kt detector measures flux normalization in order to estimate the ex-

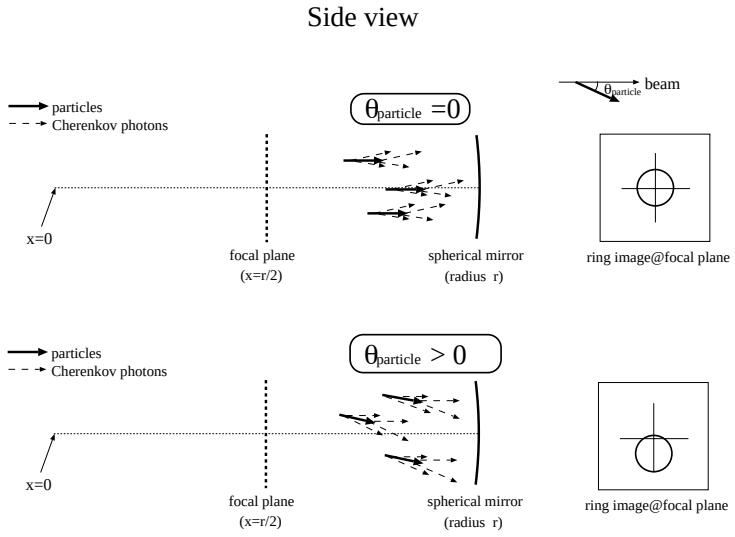

Figure 2.8: Pion monitor measures the angle and momentum of pions.

pected number of events at SK. Little systematic error is expected as the target material (water) and analysis technique are same at the far detector, Super-Kamiokande (Section 2.6).

The 1kt detector has water purification system to remove small dust, bacteria and metal ions from the water. Water purity is continually monitored through the measurement of electrical resistance. The temperature of water is around 10°C.

2.5.2 Scintillating Fiber (SciFi) Detector

The SciFi detector is a tracking detector made up of scintillating fiber (SciFi) sheets interspersed with water target tanks [25]. Where other components of the near/far detectors were used in earlier experiments, this SciFi detector was newly developed for K2K. The SciFi detector will be fully described in Chapter 3).

2.5.3 Trigger/Veto Counters, Lead Glass Counter, Muon Range Detector

Sixty four-meter long trigger and veto scintillation counters lie downstream and upstream of the SciFi detector respectively.

A lead glass counter (LG) triggers counters downstream of the SciFi detector.

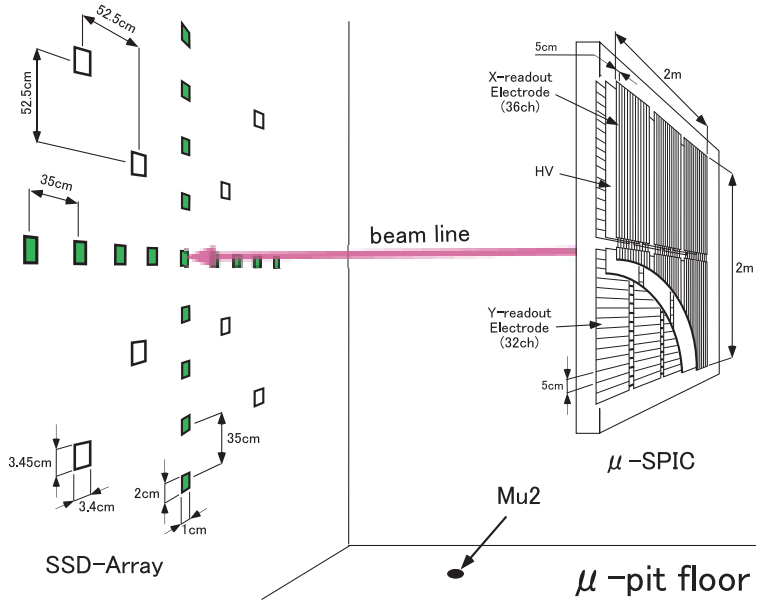

Figure 2.9: Muon monitors.

Attached to each of the six hundred cylindrical lead glass cells is a light guide which carries light to the PMT. The LG measures the contamination of ν_e in a ν_μ beam. This contamination is reported to be 2%, which is consistent with our prediction based on the Monte Carlo simulation [21].

The muon range detector (MRD) is the biggest of the near detectors. It is made up of an iron target and drift chambers.

All of these components were used in the Tristan experiment and recycled for K2K.

2.5.4 Data Aquisition (DAQ) System of Near Detectors

Figure 2.12 shows the DAQ system of the near detector. Two types of front-end computer collect data from the detectors. The 1kt Čerenkov detector runs Sun Bit3 on a VME crate. FGD runs HP-RT on a VME crate. We have 3 HP-RT, one of which handles trigger/veto counters, LG, and MRD. The other two are for the SciFi detector. Section 3.4 describes the SciFi DAQ in detail.

The trigger signal for FGD of each spill is given by the kicker magnet in the proton beam-line.

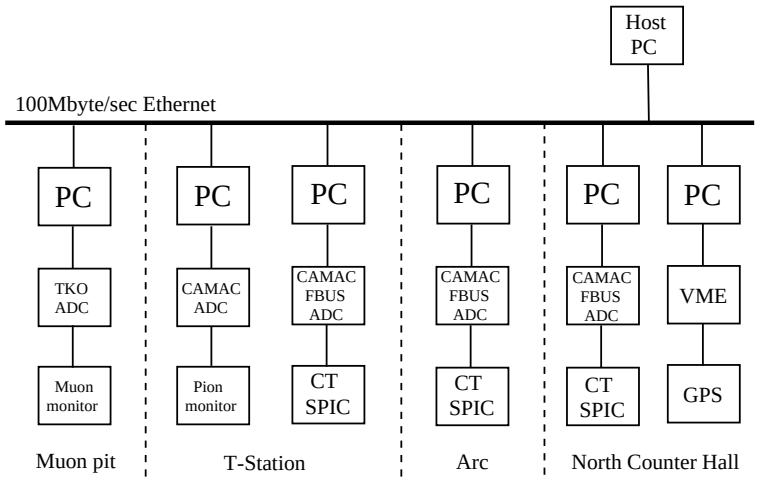

Figure 2.10: Beam line DAQ.

2.6 Far Detector

2.6.1 Super-Kamiokande

Super-Kamiokande (SK) was developed in 1996 as a successor to KamiokaNDE (Kamioka Neutrino Detector). It was constructed in a Kamioka mine in Mozumicho, Gifu Prefecture, Japan.

SK is huge, with a fiducial volume of 25ktons, yet because it is 1000m underground, the number of cosmic ray background events is smaller ($\sim 10^{-5}$) than if it were at ground level.

The detector consists of a 50kton pure water cylindrical tank, a water and air purification system, and photo multiplier tubes (PMTs). Like the 1kt detector, SK is a ring image water Čerenkov detector.

The tank is optically separated into two parts: an inner detector (ID) and an outer detector (OD). The ID is a cylinder 36.2m tall and 33.8m in diameter. The OD encases the ID. The gap between the ID and OD walls is 2m at the barrel, and 2.2m at the top and bottom. The ID has 11460 20-inch PMTs. Photo cathode coverage is 40%. The insensitive section of ID is covered with a black sheet so as not to reflect light. The OD has 1885 eight-inch PMTs. The insensitive part of OD is covered with a reflective Tyvek sheet to collect additional light.

2.6.2 Water Purification System

The pure water in the SK tank comes from a spring in the Kamioka mine. We have a water purification system in order to filter radioactive materials and to maintain good transparency (Figure 2.14. It supplies approximately 50 tons of ultra-pure water per hour. The water temperature is kept at 13°C to kill bacteria.

2.6.3 DAQ System

The inner detector DAQ system is shown in Figure 2.15. Analog-to-digital conversion is performed by 946 TKO modules known as ATM (analog timing modules) [26]. Timing (TDC) and charge (ADC) data from each PMT are read by eight online computers through the SMP (super memory partner) modules of VME. These electronics and computers are housed in five huts at the top of the SK tank.

2.7 Global Positioning System (GPS)

The K2K experiment requires precise information on the position of both the neutrino beam line and SK. Additionally, time synchronization between KEK and SK is necessary to perform event selection against continuous background events. Clocks at both sites need to be synchronized to within an accuracy of μs. For these reasons, K2K uses Global Positioning System (GPS) [23].

GPS consists of 27 satellites maintained by the US Department of Defense. Each satellite has an atomic clock. The clock time and the position of the satellite is regularly calibrated with the others in the system. Four to six satellites supply the GPS receiver with position and time information. The KEK GPS receiver is in the north counter hall. It calculates its precise latitude, longitude, and altitude, as well as the calibrated time in the form a Coordinated Universal Time (UTC) time stamp. It has an average resolution is 40 ns and a maximum fluctuation of 150 nsec.

Figure 2.16 shows the time synchronization system. Two GPS clocks run in parallel at each site, providing hardware backup as well as a check on data quality. At KEK, the two receivers are in the beam line control room and the antennae are on the room roof. At SK, the GPS receiver is in a building near the mine entrance and it is connected to a VME receiver at the central electronics hut by 2km optical fiber. It sends one UTC time stamp signal every second, which the VME receiver

converts into UTC time. The VME receiver sends calibration trigger signals to an LTC module. The LTC module has a 50 MHz clock synchronized to these trigger signals. The LTC module receives timing signals either of beam extraction at KEK or an event trigger at SK. A computer records the LTC count of the event triggered time, the calibration triggered time, and the UTC time from the VME module. The UTC time of the triggered events is calculated by interpolation of the calibrated UTC time in off-line analysis, as shown in Figure 2.16.

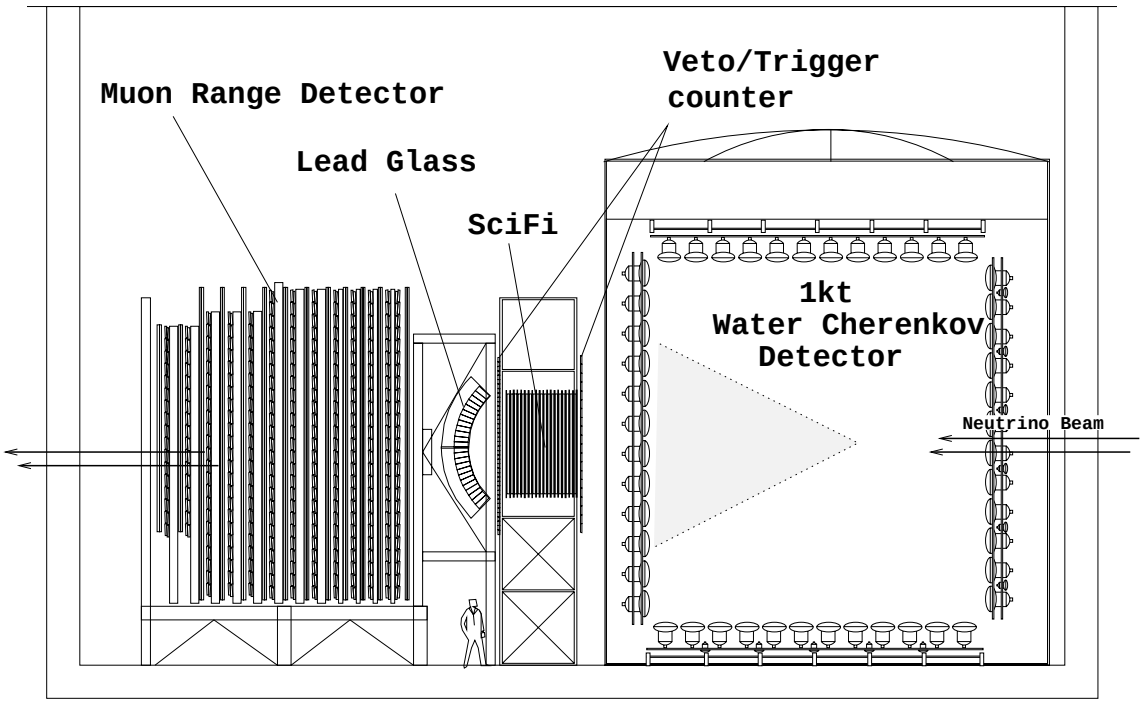

Figure 2.11: K2K near detectors.

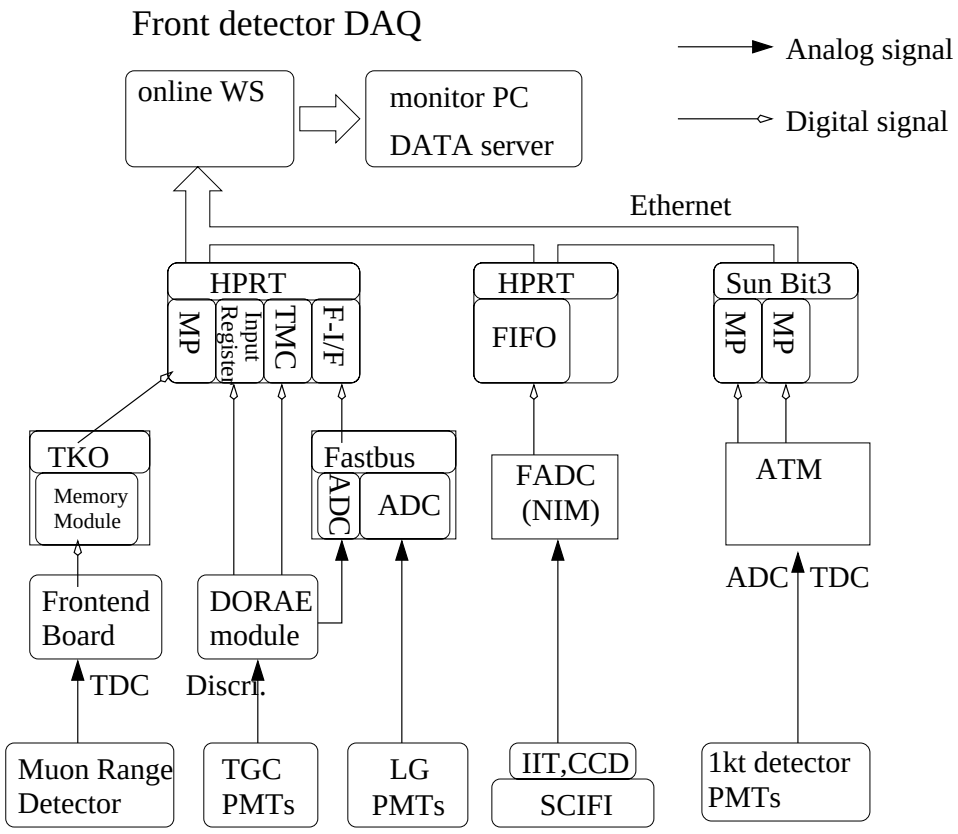

Figure 2.12: DAQ system of the near detector.

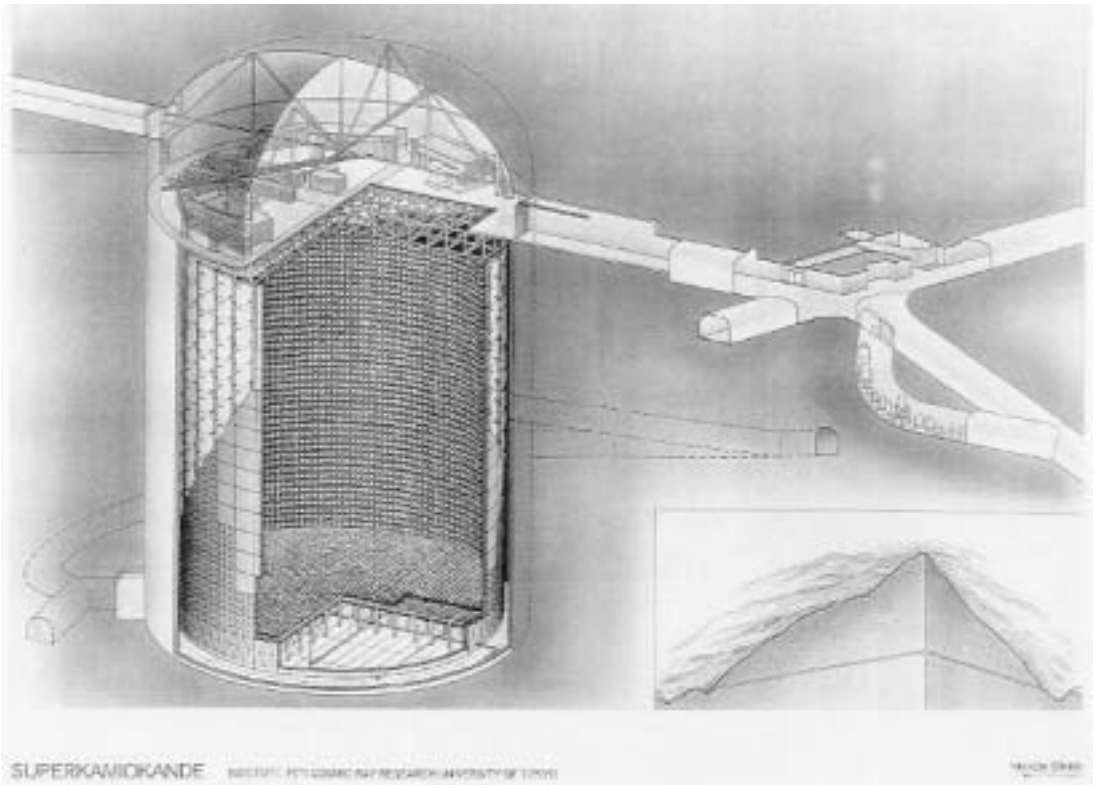

Figure 2.13: Far detector Super Kamiokande.

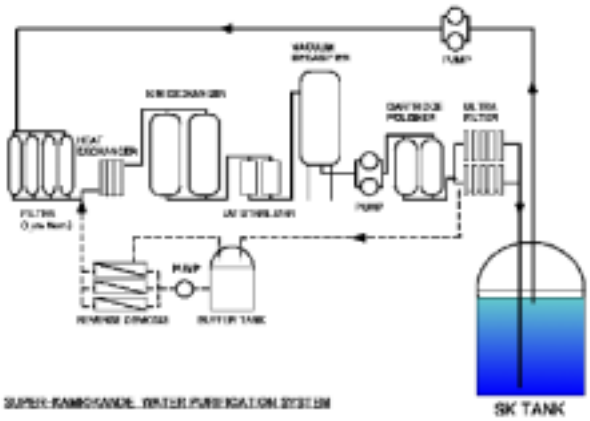

Figure 2.14: SK water purification system.

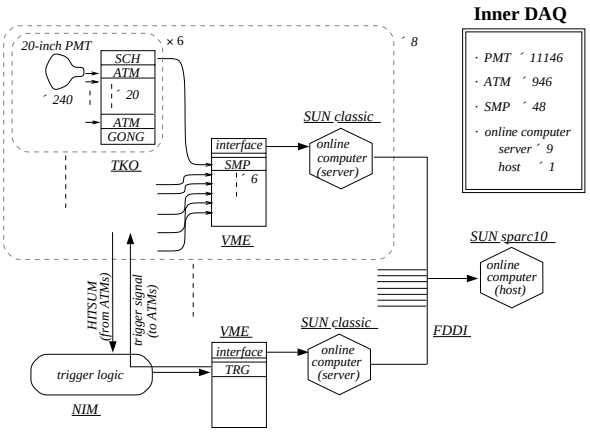

Figure 2.15: The data acquisition system for the inner detector.

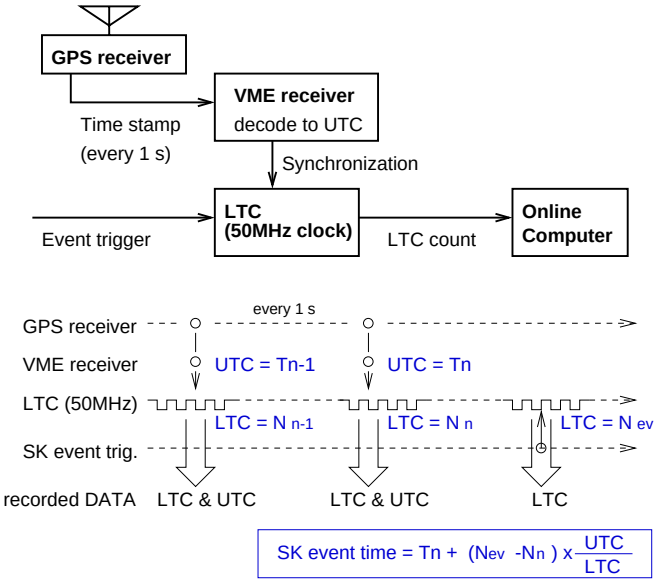

Figure 2.16: Overview of GPS system at SK. Block diagram (upper) and the timing chart (lower) are shown.

Chapter 3

SciFi Detector

3.1 Overview

SciFi (scintillating fiber) is a variety of optical fiber made from a scintillator. Nowadays SciFis are used in numerous components of particle detectors. One of K2K's fine grain detectors (FGD) is a SciFi detector. It consists of fiber tracking layers interspersed with water target tanks.

Figure 3.1 shows an overview of the SciFi detector. The SciFi detector has 20 240cm-wide tracking layers. Each layer consists of an X-tracking layer and a Y-tracking layer [the X, Y axes are perpendicular to the beam direction (Z axis)].

X and Y layers are glued onto each side of a 260cm$\times$260cm honeycomb board 1.6cm in thickness. The distance between two tracking layers is 9cm. Between the 20 tracking layers are 19 water-filled aluminum tanks. The aluminum wall is 0.18cm thick. The water target eliminates a common Super-Kamiokande detector systematic error.

3.2 Construction

3.2.1 Scintillating Fiber

Charged particles excite and ionize atoms when passing through a medium. With scintillator material, the excitation energy re-emerges as visible light during de-excitation.

Fiber made out of scintillator material is used as opt fiber and is wrapped with clad, which has a smaller refraction index. This is called "Scintillating Fiber (SciFi)". Our SciFi, Kuraray SCSF-78M, has a polystyrene scintillator core and

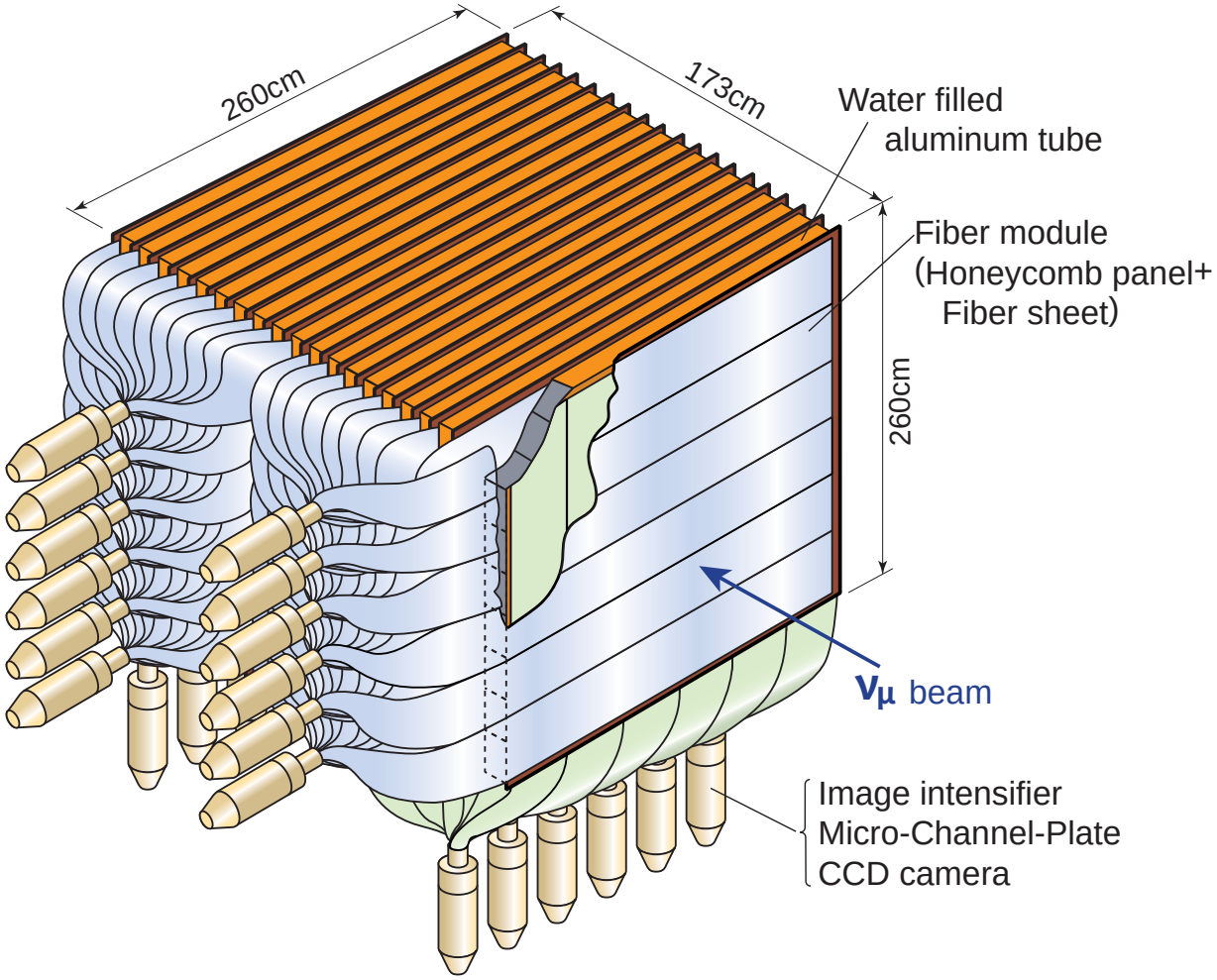

Figure 3.1: Overview of the SciFi detector.

a polymethyl methacrylate (PMMA) inner clad. These have refraction indices of 1.59 and 1.49, respectively. Light emitted from the scintillator core can pass through SciFi only when the reflection angle θ satisfies the relation:

$$\cos\theta \geq \frac{n_2}{n_1} \tag{3.1}$$

where n_1 and n_2 are the core and clad refraction indices.

SciFis are classified by the number of layers (clads) that cover the scintillator core, (e.g. single/multi-cladding fibers). SCSF-78M is multi-cladding fiber with an outer clad of fluoropolymer. Figure 3.2 is a drawing of SCSF-78M. The thickness of the clad in our SciFi is approximately two percent of the radius. Table 3.1 shows the media and refraction indices of the parts.

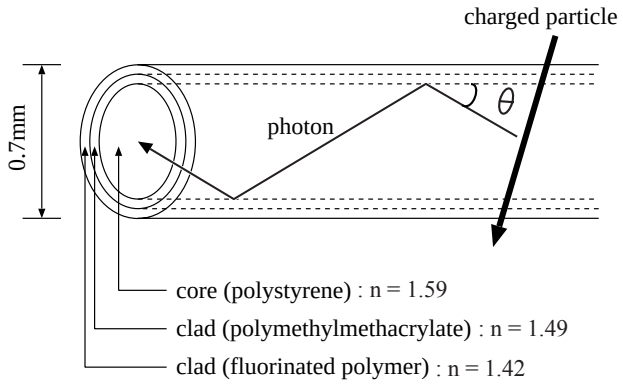

Figure 3.2: Scintillating fiber SCSF-78M (multi-cladding type).

Table 3.1: Refraction indices of SciFi SCSF-78M media.

Part	Media	Refraction index
Core	Polystyrene	1.59
Inner Clad	PMMA	1.49
Outer Clad	Fluoropolymer	1.42

The IIT (Image Intensifier Tube) photocathode shows the best sensitivity to 300∼500nm wavelength light (Figure 3.13), requiring us to use the SciFi, which emits light of approximately 450nm wavelength. The light originally emitted from the core polystyrene is 340nm wavelength yet a wavelength shifter (WLS) is doped in the core and transports it efficiently. The SCSF-78M WLS shifts light from the core to light of 430nm wavelength. (Figure 3.3).

We examined the light yield, attenuation length, and aging effect on SciFi of several scintillators from private companies. SCSF-78M (improved version 11) at less than 20°C showed sufficient life time for our several-year experiment [27] (Figure 3.4). The wavelength of SCSF-78M is shown in Figure 3.3. We measured its attenuation length using a radio isotope electron source (^{90}Sr) at 320cm [27, 28] (Figure 3.5).

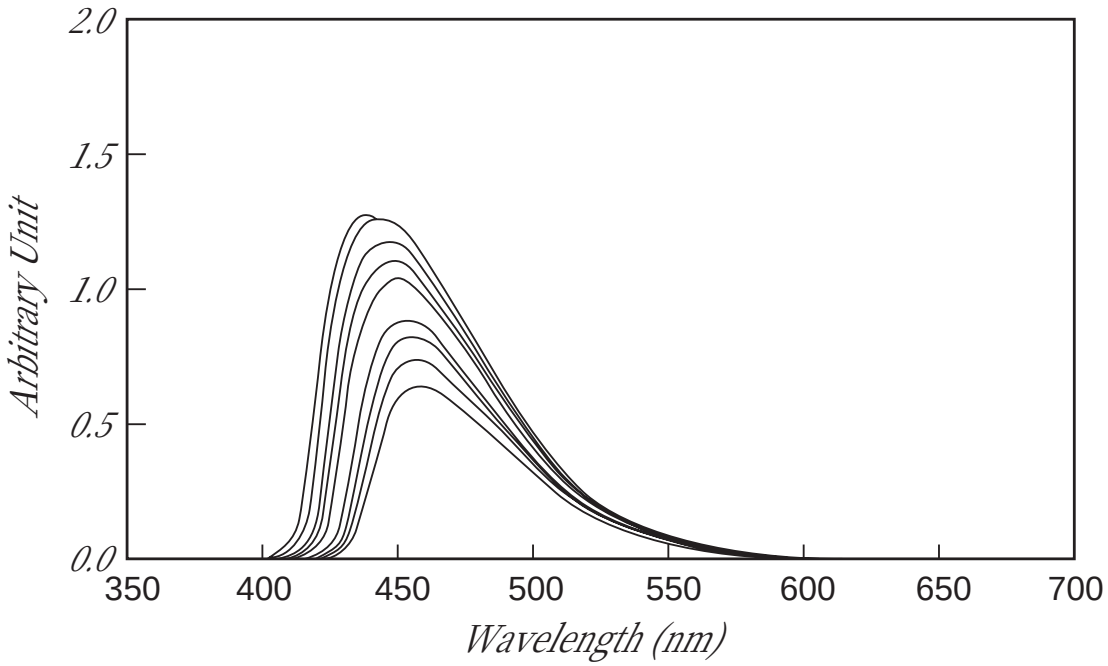

Figure 3.3: SCSF-78M (version 11) light wavelength. The eight lines correspond to measurement at 20cm, 40cm,... 160cm from the entrance point of the light.

3.2.2 Scintillating Fiber Sheets

Tracking layers need SciFi sheets with no space between fibers. The Nagoya University group [29] developed a method of making suitable SciFi sheets. First, fiber is wound around a grooved metal drum, then glued together with silicon paint. The painted SciFi sheets have a suitably long life time [27]. After the paint dries, the fiber is cut and opened. Figure 3.6 and 3.7 show the sheet spooling process.

The SciFi sheet has dimensions of 40cm $\times$ 370cm (on the left in Figure 3.8). One sheet is composed of two fiber layers. Figure 3.8 shows the cross section of a sheet on the right. Six SciFi sheets are glued to each side of the honeycomb panel (Figure 3.9), forming one unit of readout module.

An epoxy resin (Araldite CY221/HY2967) is used to glue the SciFi sheets to the honeycomb panels. When the usual glue was found to damage and age SciFi, the SciFi light yield was carefully tested with different glues. Evaporating a gas dominated by toluene in the glue for approximately five minutes proved to be the best solution. [30].

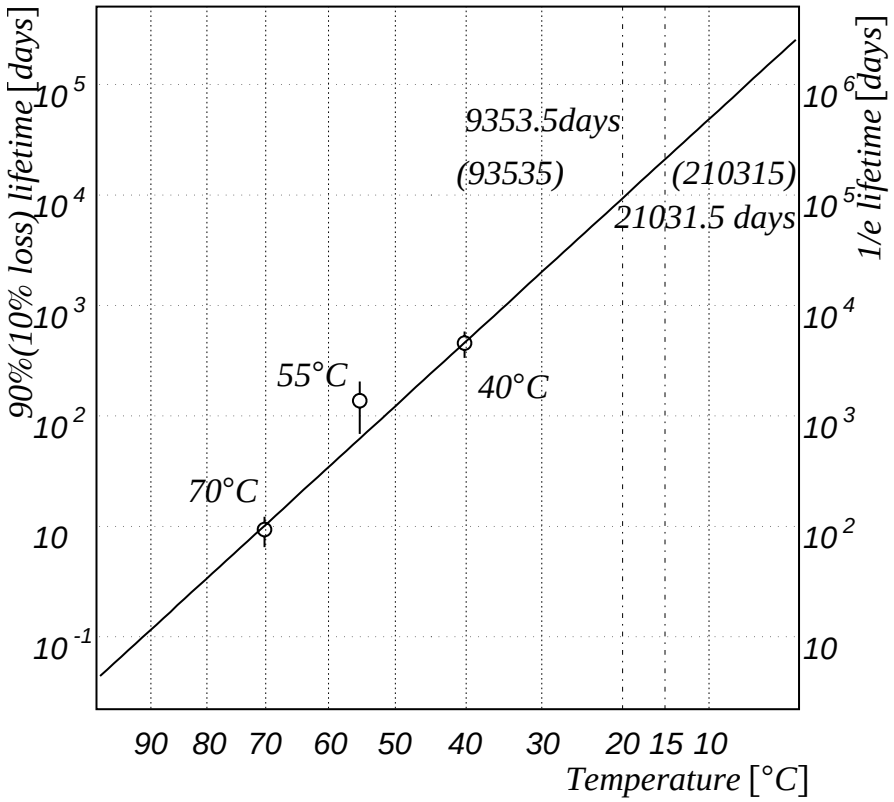

Figure 3.4: Aging of SciFi SCSF-78M. The life times of the product under 40, 50, and 70 °C are plotted. We can estimate the life time light yield falls 10% at under 20 °C.

Both ends of the sheet are polished. To collect more light, the side that is not read out is coated with aluminum. Sheets are cut and bundled as in Figure 3.10 because the photocathode of IIT is circular [31]. A polishing machine for the SciFi bundles was developed by a group from the University of Washington. One of the polished bundles is shown in Figure 3.11.

3.2.3 Water Target

The Boston University group developed the aluminum water tanks. Their size is 240cm × 16cm × 6cm. The wall is 0.18cm thick. There are 19 layers of target, each layer consisting of 15 tanks. Before installation, they were checked

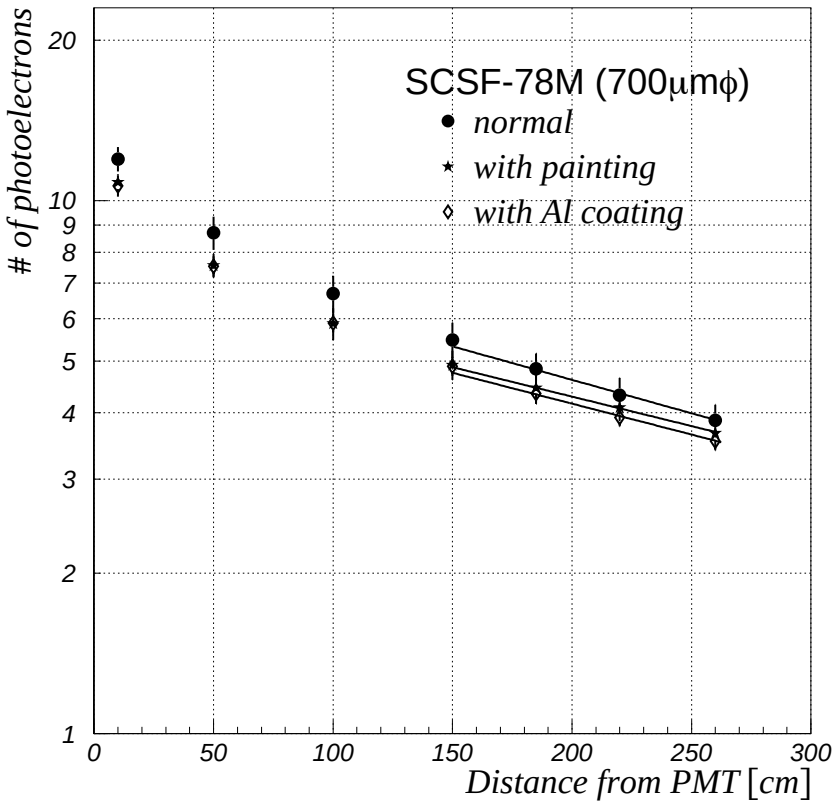

Figure 3.5: SciFi SCSF-78M attenuation measurement. The star and the white circle correspond to measurement with white paint and Al-coated fibers, respectively. An Al-coated fiber has a fitted attenuation length of 320cm.

for leakage with an air compressor. [1]

3.3 Readout System

The SciFi detector readout system consists of serial coupling to IITs (image intensifier tubes) and a CCD (charge coupled device) camera [32].

The IIT is a photo detector which accelerates photo electrons with a high voltage electric field. After the photo electrons are emitted from the photocath-

[1] After installation, 21 out of 285 water tanks leaked and were subsequently emptied. The decrease of fiducial mass was taken into account in our detector simulation.

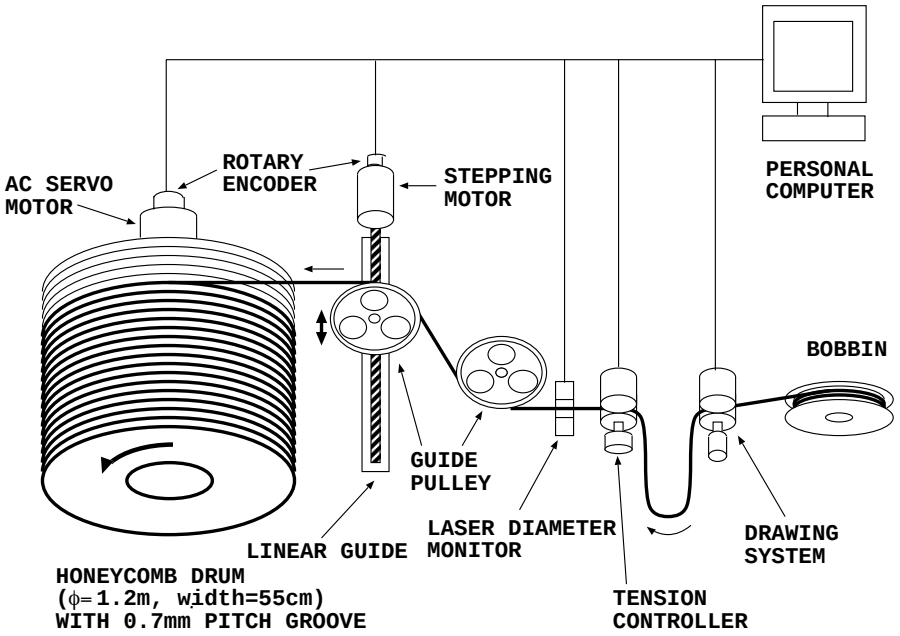

Figure 3.6: SciFi sheet spooling machine.

ode, a phosphor screen converts them into light. The IIT can amplify the light while retaining information about the image.

Our system utilizes two kinds of IIT (Figure 3.12). The front IIT is a Hamamatsu Photonics V5502UX, the rear is a V1366GX. They are coupled by fibers. The front IIT is an electrostatic IIT. The sensitive surface of its photocathode is 100mm ϕ and typical quantum efficiency is 22% at wavelength 430nm (see Figure 3.13). The rear IIT is a micro channel plate (MCP) IIT that accelerates photo electrons. Applying the gate signal turns on the MCP high voltage. The gate is controlled by TTL positive logic and can open from 200nsec. to DC, at a maximum frequency of 100Hz. For K2K, we opened the gate 100 μsec. every 2.2 seconds, synchronizing to neutrino beam timing, because the life time of the phosphor screen is 100 μsec. (Figure 3.14).

Hamamatsu made a 24-channel high voltage supplier for the IITs (Figure /ref-Fig.SFHV). It supplies power to both front and rear IITs. Table 3.2 and 3.3 summarize their applied high voltage. Typical total gain of the IIT chain is 7×10^6, calculated:

$$Total\ Gain\ = \gamma/e_F \times QE_B \times \gamma/e_B \times \text{MCP Gain} \times \eta \qquad (3.2)$$

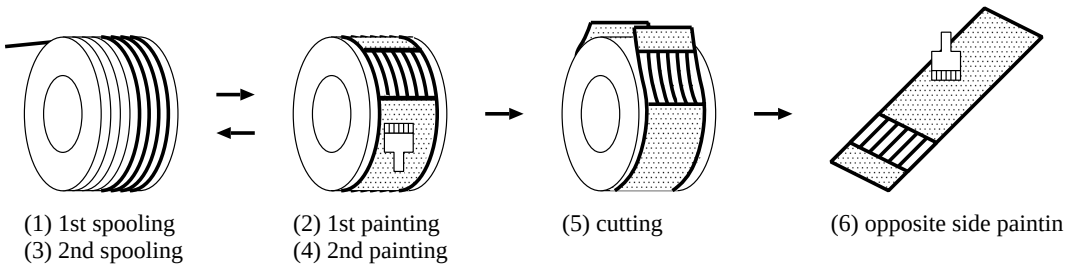

Figure 3.7: SciFi sheet spooling process.

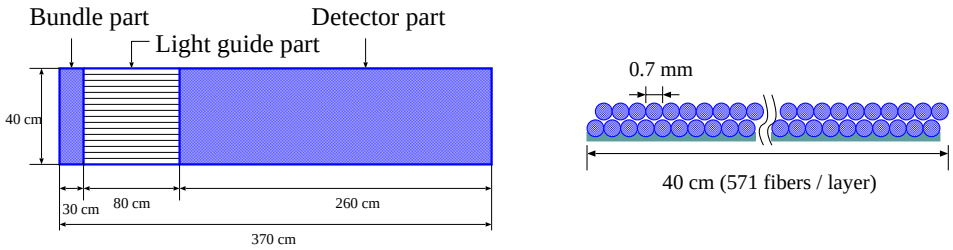

Figure 3.8: Top view (left) and cross section (right) of SciFi sheet.

where suffices F and B correspond to the front and rear IITs. γ/e is the gain of the phosphor screen, 530 for the front IIT and 20 for the rear. QE_B is typically 14. MCP gain is 6×10^3 at applied voltage 900kV. η is 0.8. An image of 100mm ϕ at the photocathode is reduced to 23mm ϕ after output to the phosphor screen.

A CCD camera is a well-known electric appliance. An NTSC Hamamatsu was used. It shoots 8.8mm×6.6mm(2/3 in.) with 768(H)×493(V) pixels. The relay lens has a reduction rate of 3.09:1.

3.4 Data Aquisition (DAQ)

The CCD camera outputs a composite video signal through a BNC cable. Twelve flash ADCs (analog to digital converters) convert each pixel of the video signal from 24 CCD cameras into an 8-bit of brightness. The VME threshold module in each IIT sets the threshold values of ADC brightness. Twenty four FIFO (first in first out) memories (VME) store information on pixels with brightness greater than the threshold and coordinate information from the CCG (clock and coordinate generator). The CCG also sends a 14MHz pixel clock signal to the

Table 3.2: IIT V5502UX applied high voltage.

Part	Voltage	Current(max.)
Photocathode	0V	-
1st Grid	110V	1μA
2nd Grid	1200$\sim$1400V	1μA
3rd Grid	3.4kV	1μA
Anode	20kV	3μA
for Pump	2.5kV	20μA

Table 3.3: IIT V1366GX applied high voltage.

Part	Voltage
Photocathode	0V
Anode	2.7kV
Collimator	700V
MCP in	1.7kV
MCP out	2.2$\sim$2.7kV
Screen	7.3$\sim$7.8kV

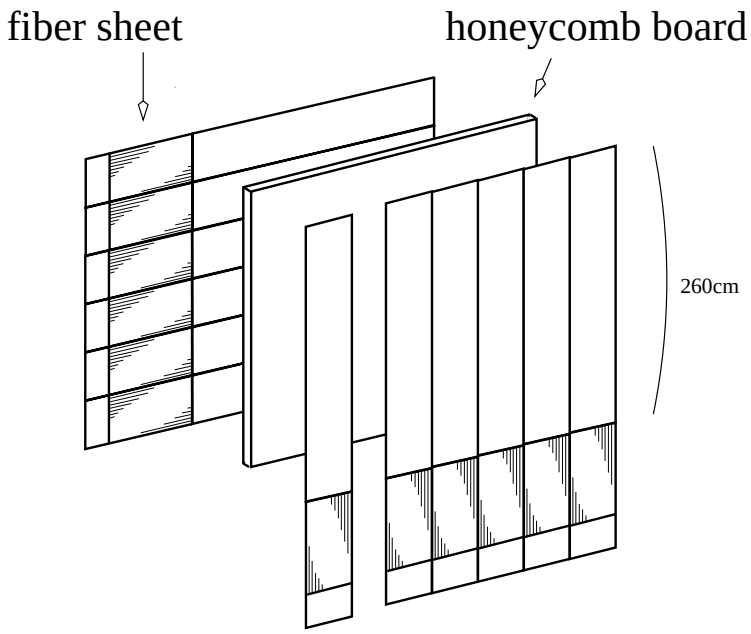

Figure 3.9: Six SciFi sheets are glued to each side of a honeycomb panel.

ADC modules. The size of the data is one word per pixel at this stage. The total data size of a typical beam spill is approximately 2.5kbites. Figure 3.16 shows the DAQ setup of the SciFi detector.

3.5 Calibration System

The analysis procedure will be described in Chapter 5. To reconstruct tracks in SciFi at the analysis stage, we need one-to-one correspondence between the identification of fibers and their position in the CCD camera view. We call this an "EL table" as we developed the technique of position calibration using an EL (electro-luminescent) plate.

Additionally, the IIT light yield was calibrated principally in order to build a simulation of the SciFi detector. Calibrated LED light was used to determine operational high voltage and to understand the response of IIT-CCD system. A detailed description is in Section 4.3.

3.5.1 EL Calibration

An EL (electro-luminescent) plate is a device that emits light when applied voltage is changed. It is thin and easy to cut.

We made 240 EL plate strips. Figure 3.10 shows how the EL plates are placed over the back of the SciFi sheets with the readout at the front. Every 20th or 40th fibers is selected (we call them fiducial fibers) and illuminated as shown in Figure 3.17. We flash the EL plates periodically and take data. To take data, the MCP gate must be delayed approximately 300μ seconds. This procedure is called EL calibration. Identification the fiducial fibers in the CCD view enables calculation the positions of the non-illuminated fibers. The position resolution of an EL map is approximately 100μm [33, 34].

We carry out EL calibration prior to a neutrino beam run and make an EL table for the coming run period. One run period lasts approximately six months, from January to July of each year. The drift of IITs during those six months is within 100μm [33].

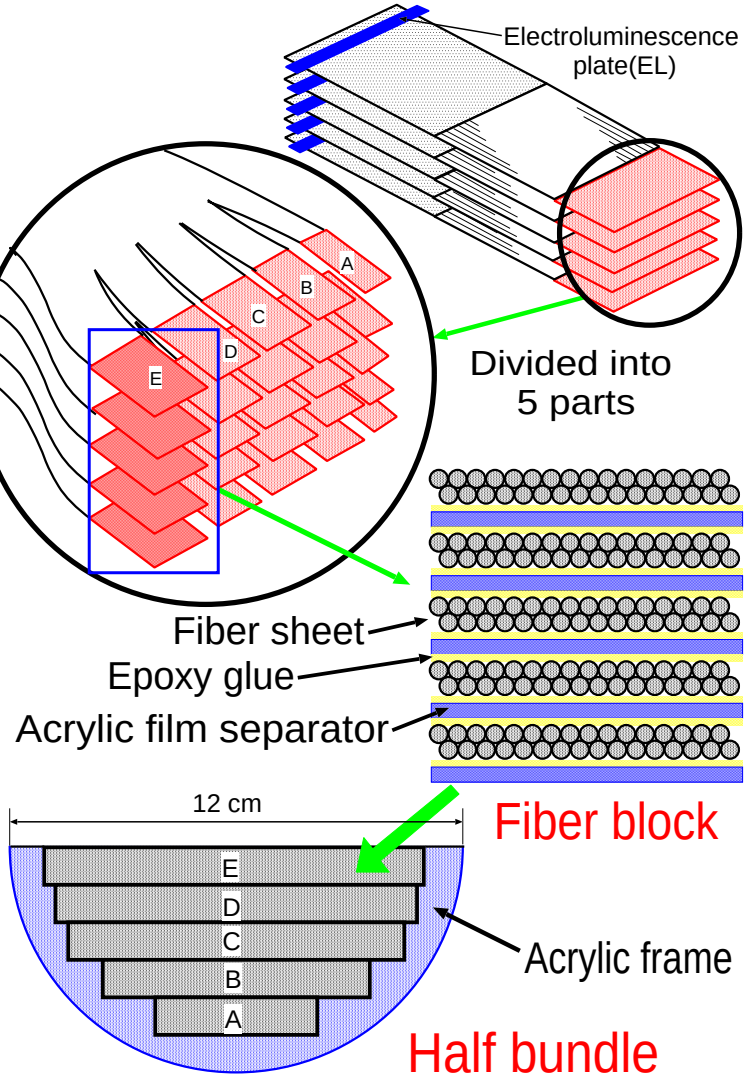

Figure 3.10: How SciFi sheets are bundled.

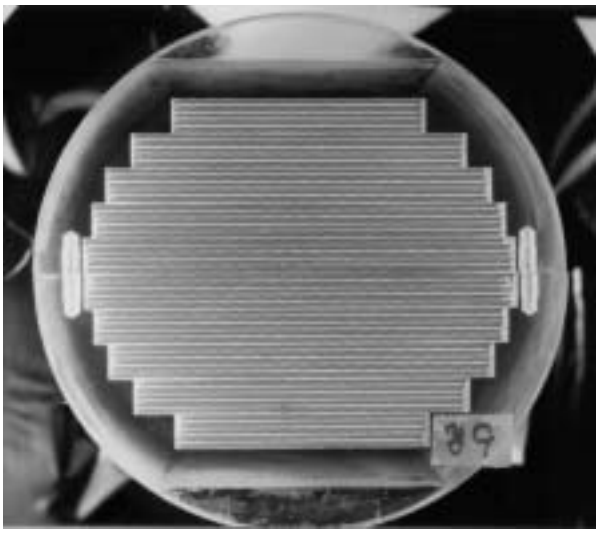

Figure 3.11: Picture of a fiber bundle.

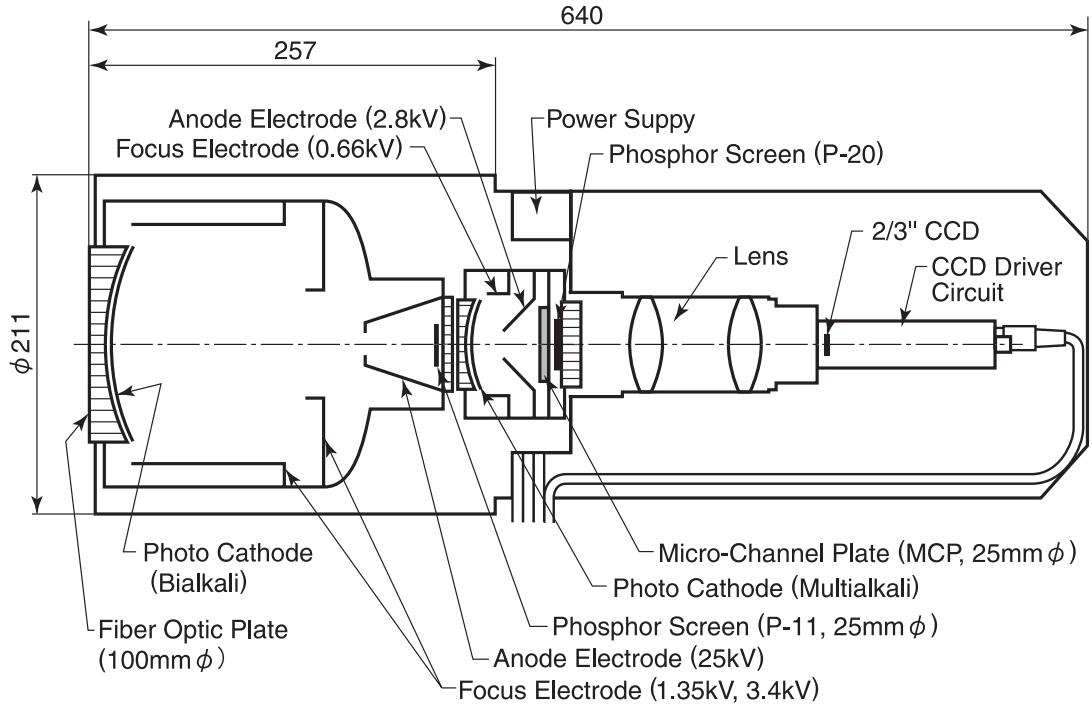

Figure 3.12: IIT-CCD chain.

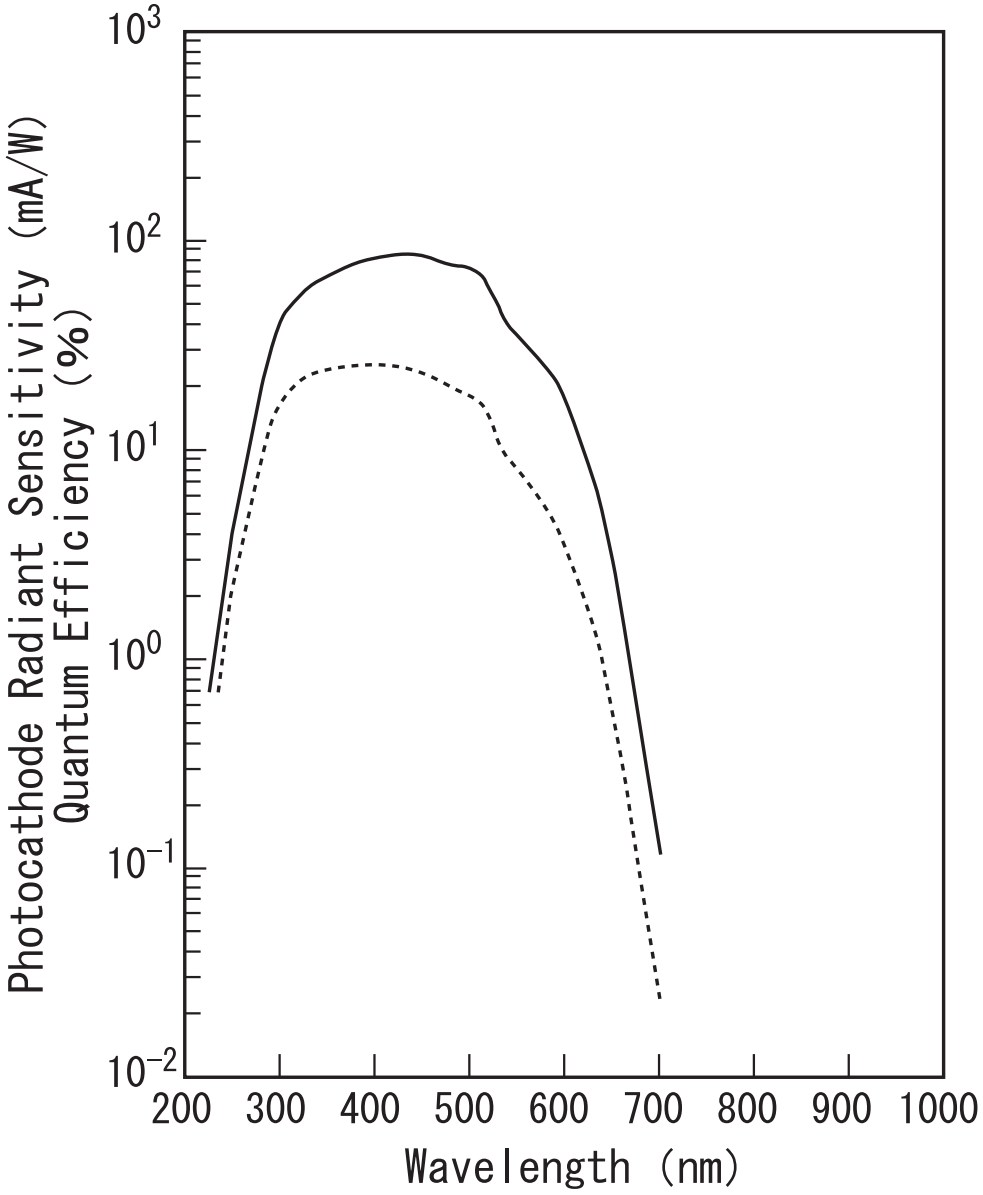

Figure 3.13: Sensitivity of front IIT (V5502UX) photocathode. The most sensitive region is 400nm∼600nm. The dashed line shows quantum efficiency of a photocathode.

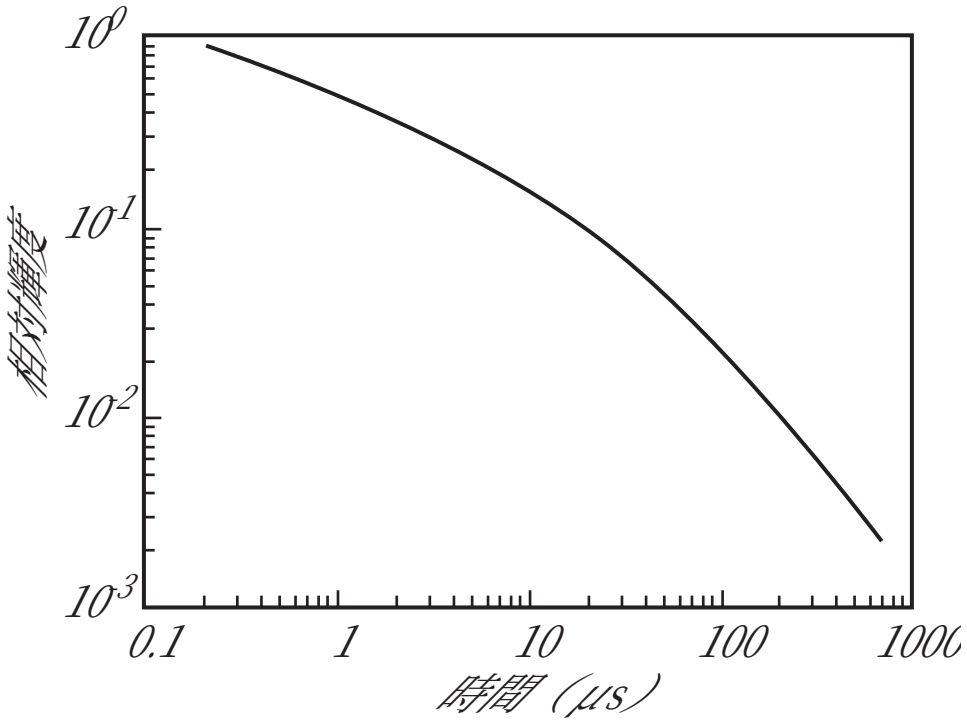

Figure 3.14: Lifetime of phosphor screen. X-axis is time (μsec.), Y-axis is relative brightness.

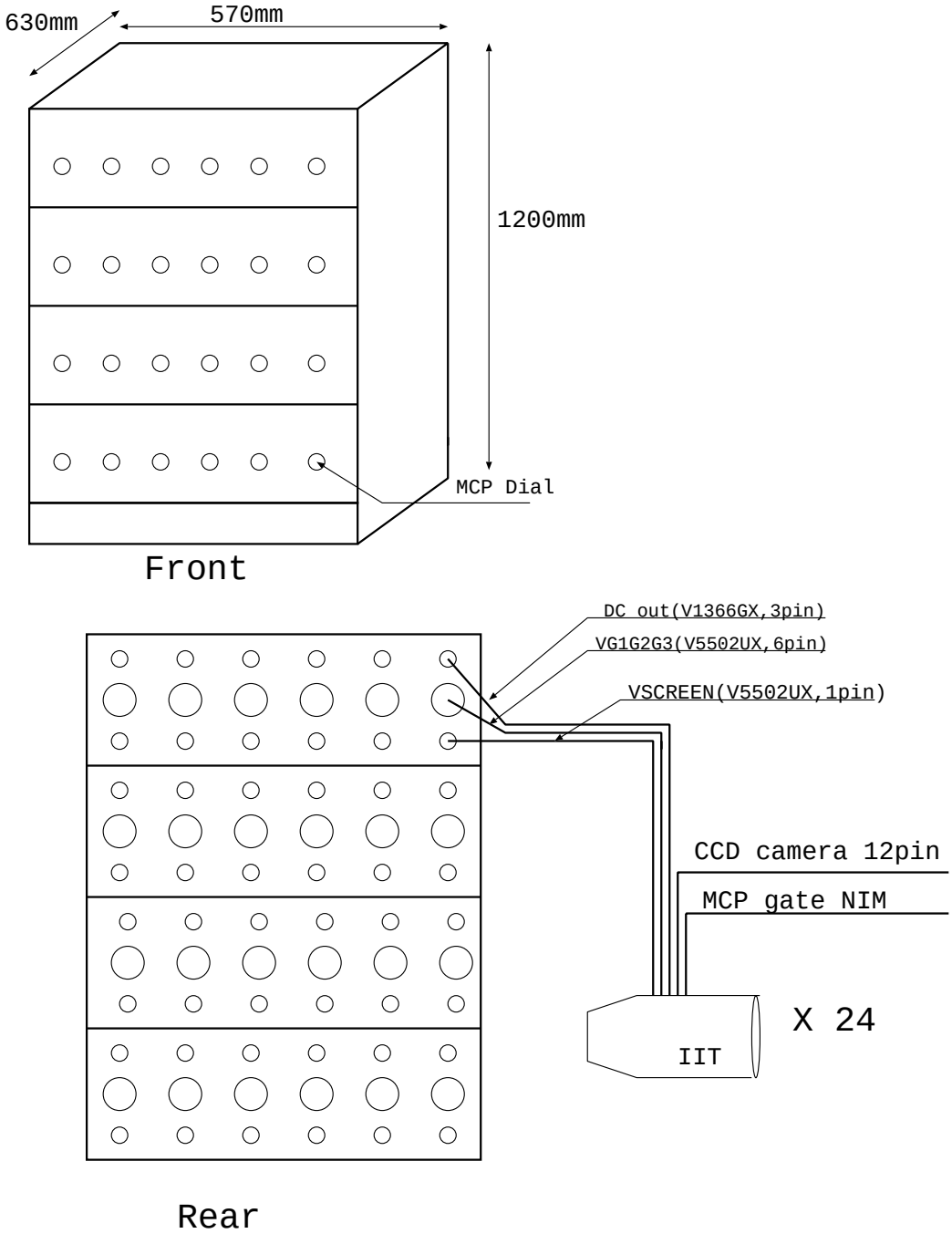

Figure 3.15: HV supplier for 24 IITs.

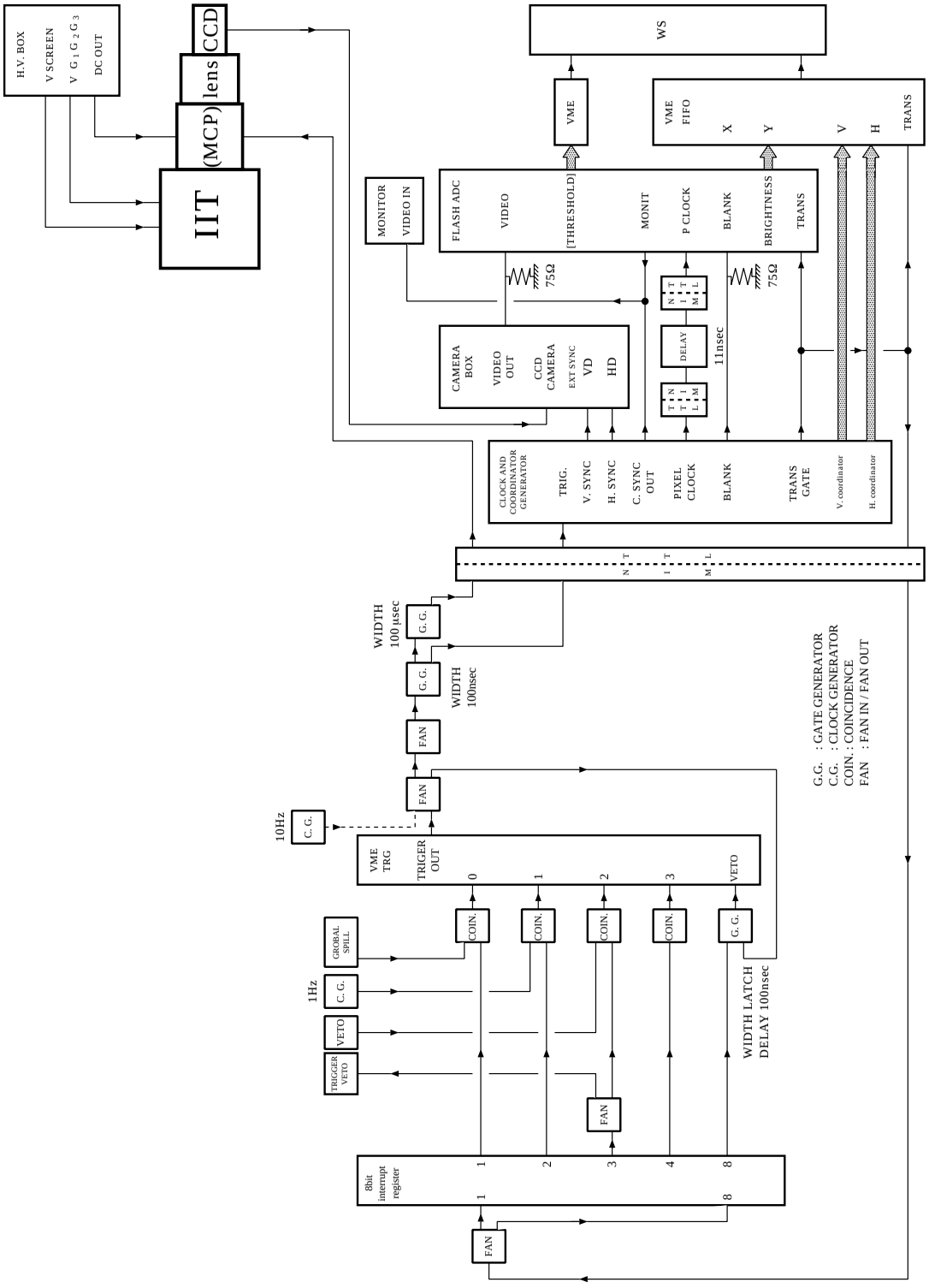

Figure 3.16: DAQ setup of the SciFi detector.

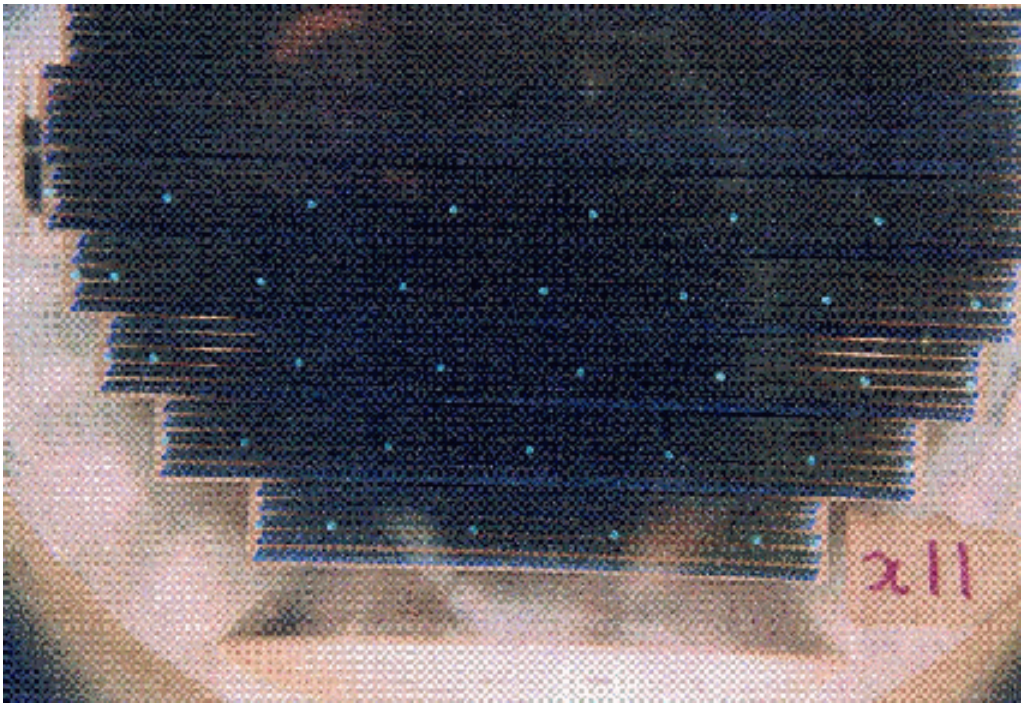

Figure 3.17: Picture of fiducial fibers in a fiber bundle illuminated by the EL.

Chapter 4

Simulations

Simulations are an important aspect of high energy physics. They enable us to estimate detector feasibility and performance prior to construction. Additionally, simulations are used to estimate the uncertainty of measurements at the analysis stage. Various computer programs have been developed that simulate physical processes and/or detector response. These commonly utilize the Monte Carlo (MC) method Bib.PDG2000. For this reason, the simulation or simulation result is often referred to as "MC".

K2K runs three simulations:

1. **Neutrino beam simulation**
   This simulates proton injection to the aluminum target, pion production, pion focusing by magnetic horn, and the tracking of pions until their decay to neutrinos. It delivers a neutrino flux at near and far detectors.

2. **Neutrino interaction simulation**
   This simulates neutrino interaction on target nuclei. It provides information on daughter particles of neutrinos.

3. **Detector response simulation**
   This simulates the transportation of daughter particles through the detector and detector response. The input for this simulation is the four-vectors of secondary particles from the neutrino interaction simulation.

4.1 Neutrino Beam

For neutrino beam simulation, the following is taken into account:

1. Proton profile at the target,
2. Production of secondary particles,
3. Magnetic horn focusing,
4. Particle decay.

Two SPICs (silicon pad ionization chambers) measure proton beam emittance between the last beam line magnet and the target horn. The SPICs are V39SPIC and TGTSPIC, respectively. The measurements are the input for beam simulation.

The hadron interaction is one of the largest ambiguities of the simulation. Pion production simulation adopts the Cho model [38], with Sanford-Wang parameterization [39] determined experimentally. In this model, the differential yield of the secondary particle is as follows;

$$\frac{d^2n}{d\theta dp} = C_1 \cdot p^{C_2} \left(1 - \frac{p}{p_B - 1}\right) \cdot exp\left(-\frac{C_3 \cdot p^{C_4}}{p_B^{C_5}} - C_6 \cdot \theta(p - C_7 \cdot p_B \cos^{C_8}\theta)\right) \tag{4.1}$$

where p, p_B are the momentum of the secondary particle and the beam momentum, respectively. θ is the angle between the secondary particle and the beam axis. C_1, C_2,...C_8 are the fitted parameters for π^+ according to Cho.

The GEANT package developed by CERN [37] is used to simulate the transportation of particles in the magnetic field of the horn. GEANT also simulates the decay of pions in the gas decay volume. The simulation is expected to deliver a 98% pure ν_μ beam with an average energy $< E_\nu > 1.3$GeV. Contributions from kaons etc. are expected to be quite small.

The resulting neutrino flux at KEK and SK is shown in Figure 4.1. From the beam MC, ν_e /ν_μ is estimated to be 1.3%, $\bar{\nu_\mu}/\nu_\mu$ to be 0.5%, and $\bar{\nu_e}/\nu_\mu$ to be $\sim 2 \times 10^{-4}$.

4.2 Neutrino Interaction

Neutrino interactions in the energy region of the K2K experiment are categorized into the following types:

1. Charged current (CC) and neutral current (NC) elastic scattering off electron ($\nu + e^- \rightarrow \nu + e$)

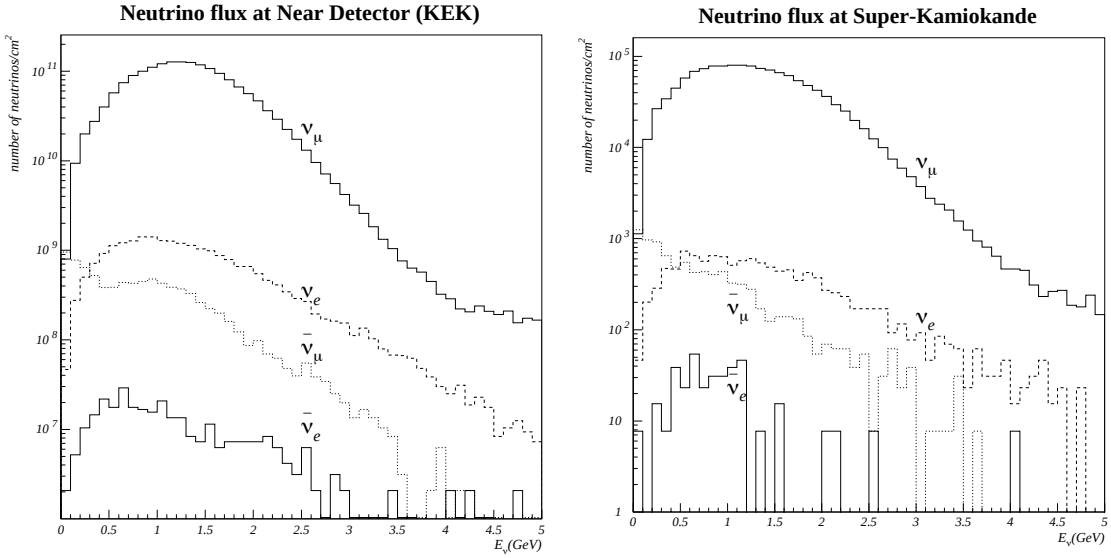

Figure 4.1: Neutrino flux calculated by beam simulation. The hadron production model selected is the Cho model. Left figure: Neutrino flux at KEK. Right figure: Neutrino flux at SK.

2. CC quasi-elastic scattering off nucleon ($\nu + N \rightarrow l + N'$)
3. NC elastic scattering off nucleon ($\nu + N \rightarrow \nu + N$)
4. CC single meson production ($\nu + N \rightarrow l + N' + meson$)
5. NC single meson production ($\nu + N \rightarrow \nu + N' + meson$)
6. CC deep inelastic scattering ($\nu + N \rightarrow l + N' + hadrons$)
7. NC deep inelastic scattering ($\nu + N \rightarrow \nu + N' + hadrons$)
8. CC coherent pion production ($\nu + ^{16}\mathrm{O} \rightarrow l + ^{16}\mathrm{O} + \pi$)
9. NC coherent pion production ($\nu + ^{16}\mathrm{O} \rightarrow \nu + ^{16}\mathrm{O} + \pi$)

where l represents a charged lepton and N and N' represent nucleons.

4.2.1 Elastic Scattering off Electron

The cross section of this interaction is approximately three orders of magnitude smaller than the other modes ($\sim 10^{-41} cm^2$ at E_ν=1.0GeV) and therefore it is simply omitted from the simulation.

4.2.2 Quasi-Elastic Scattering off Nucleon

This reaction is the dominant mode in the K2K neutrino beam energy region. Our simulation of the interaction is based on Llewellyn Smith's formula [40]. The amplitude is described as a product of hadronic and leptonic weak currents:

$$T = \frac{G_F}{\sqrt{2}}\bar{u}(k_2)\gamma^\mu(1-\gamma_5)u_\nu(k_1) < N'(p_2)|J_\mu^{hadron}|N(p_1) > \tag{4.2}$$

where G_F is the Fermi coupling constant, $p_1(p_2)$ is the initial (final) nucleon 4-momentum, and $k_1(k_2)$ is the initial (final) lepton 4-momentum. The hadronic weak current is expressed as:

$$< N'|J_\mu^{hadron}|N >= cos\theta_c \bar{u}_{N'}(p_2)\left[\gamma_\mu F_V^1(q^2) + \frac{i\sigma_{\mu\nu}q^\nu \xi F_V^2(q^2)}{M} + \gamma_\mu\gamma_5 F_A(q^2)\right] u_N(p_1) \tag{4.3}$$

where $F_V^1(q^2)$ and $F_V^2(q^2)$ are the vector form factor, $F_A(q^2)$ is the axial vector form factors, $q \equiv k_1 - k_2$ is the 4-momentum transfer, M is the target nucleon mass, and θ_c is the Cabbibo angle. If we assume the conserved vector current hypothesis, $F_V^1(q^2)$ and $F_V^2(q^2)$ are written in terms of the electric and magnetic form factors, G_E and G_M:

$$\begin{aligned} F_V^1(q^2) &= \left(1 - \frac{q^2}{4M^2}\right)^{-1}\left[G_E(q^2) - -\frac{q^2}{4M^2}G_M(q^2)\right] \\ \xi F_V^2(q^2) &= \left(1 - \frac{q^2}{4M^2}\right)^{-1}\left[G_E(q^2) - G_M(q^2)\right] \end{aligned} \tag{4.4}$$

where $\xi \equiv \mu_p - \mu_n = 3.71$. μ is the anomalous magnetic dipole moment of nucleon. G_E and G_M have dipole forms which have been determined by electron scattering experiments:

$$G_E(q^2) = (1+\xi)^{-1}G_M(q^2) = \frac{1}{\left(1 - \frac{q^2}{M_V^2}\right)} \tag{4.5}$$

where M_V is vector mass which is set at 0.84 GeV/c^2 in our simulation.

By analogy with the vector form factor, we assume the axial vector form factor F_A has a dipole form:

$$F_A(q^2) = -\frac{1.23}{\left(1 - \frac{q^2}{M_A^2}\right)^2} \tag{4.6}$$

where M_A is the axial vector mass. Several experiments suggested that 0.9 GeV/c^2 $\leq$ M$_A$ $\leq$1.1 GeV/c^2 [41]. We adopt 1.01 GeV/c^2 in our simulation. The constant value 1.23 came from neutron β decay experiments [42].

The differential cross section is expressed as follows:

$$\frac{d\sigma^{\nu(\bar{\nu})}}{dq^2} = \frac{M^2 G_F^2 \cos^2\theta_c}{8\pi E_\nu^2}\left[A(q^2) \mp B(q^2)\frac{s-u}{M^2} + C(q^2)\frac{(s-u)^2}{M^4}\right] \tag{4.7}$$

where s and u are Mandelstam variables, E_ν is a neutrino energy, and m is an outgoing lepton mass. $A(q^2)$, $B(q^2)$, and $C(q^2)$ are written as follows:

$$\begin{aligned}
A(q^2) &= \frac{m^2-q^2}{4M^2}\left[\left(4-\frac{q^2}{M^2}\right)|F_A|^2 - \left(4+\frac{q^2}{M^2}\right)|F_V^1|^2 - \frac{q^2}{M^2}|\xi F_V^2|^2\left(1+\frac{q^2}{4M^2}\right)\right. \\
&\quad \left. -\frac{4q^2 F_V^1 \xi F_V^2}{M^2} - \frac{m^2}{M^2}\left((F_V^1+\xi F_V^2)^2 + |F_A|^2\right)\right] \\
B(q^2) &= \frac{q^2}{M^2}\left(F_A(F_V^1+\xi F_V^2)\right) \\
C(q^2) &= \frac{1}{4}\left(|F_A|^2 + |F_V^1|^2 - \frac{q^2}{4M^2}|\xi F_V^2|^2\right)
\end{aligned} \tag{4.8}$$

For the nucleons in oxygen nuclear, we also consider both the Fermi motion of the target nucleon and the Pauli blocking effect. We use the Fermi momentum distribution in ^{16}O estimated by the electron scattering experiment on ^{12}C target [43]. The Pauli blocking effect is reproduced in this simulation. It gives the outgoing nucleon's momentum, which must be larger than the Fermi surface momentum. This sets a limit of 217MeV/c for ^{16}O [43]. In other cases quasi-elastic interaction is forbidden.

Neutral current (NC) QE cross-sections are derived by multiplying factors and charged current (CC) QE cross-sections. The factors come from neutrino experiments [44, 45]:

$$\begin{aligned}
\sigma(\nu p \to \nu p) &= 0.153 \times \sigma(\nu n \to e^- p) \\
\sigma(\bar{\nu} p \to \bar{\nu} p) &= 0.218 \times \sigma(\bar{\nu} p \to e^+ n) \\
\sigma(\nu n \to \nu n) &= 1.5 \times \sigma(\nu p \to \nu p) \\
\sigma(\bar{\nu} n \to \bar{\nu} n) &= 1.0 \times \sigma(\bar{\nu} p \to \bar{\nu} p)
\end{aligned} \tag{4.9}$$

4.2.3 Single Meson Production via Baryon Resonances

Single meson production via resonance is the dominant hadron process in the region where the invariant mass of the hadron system is less than approximately 2.0 GeV/c^2.

The simulation of single meson production via resonance is based on Rein and Sehgal's model [46]. This model was originally developed for single pion productions. We extend their method to encompass η and the K meson productions.

In this model, single meson production is considered in two steps:

$$\begin{aligned} \nu + N &\rightarrow l(\nu) + N^* && \text{Resonance production} \\ N^* &\rightarrow N' + \pi(\eta, K) && \text{Resonance decay} \end{aligned}$$

where N^* is baryon resonance, N and N' are nucleons, and l is an outgoing charged lepton. The amplitude of the baryon excitation is:

$$T(\nu N \rightarrow l N^*) = \frac{G_F}{\sqrt{2}} \bar{u}_l \gamma^\mu (1 - \gamma_5) u_\nu < N^* | J_\mu^h | N > \tag{4.10}$$

where $< N^* | J_\mu^h | N >$ is the weak hadronic current for this process. The matrix element of the hadronic current is calculated by the FKR (Feynman, Kislinger, Ravndal) model [47], which describes the baryon as a relativistic three-body system.

The amplitude of resonance decay is expressed by Breit-Wigner formula with an experimentally measured decay width and a branching ratio of each resonance. These interactions are characterized by q^2 and W, and the differential cross section can be written:

$$\frac{d^2\sigma}{dq^2 dW} = \frac{1}{32\pi M E_\nu^2} \cdot \frac{1}{2} \left| \sum_{j,spin} T(\nu N \rightarrow l N_j^*) \cdot \sqrt{\chi_E} \cdot \left(sign(N_j) \sqrt{\frac{\Gamma_j}{2\pi}} \cdot \frac{1}{W - M_j + i\frac{\Gamma_j}{2}} \right) \right|^2 \tag{4.11}$$

where N_j^* is j's baryon resonance, E_ν is the neutrino energy, $\sqrt{\chi_E}$ is the branching ration of N_j^* to N'+meson, M_j is N_j^*'s mass, Γ_j is the total decay width of N_j^*, and $sign(N_j)$ is the sign of the decay amplitude of N_j^*. The $sign(N_j^*)$ is the sign of decay amplitude of N_j^* which is lost when the decay width is experimentally measured. in order to consider the interference effects of the neighboring resonances correctly. Summation in Eq.4.11 is done over all relevant resonances and their spin, In our simulation, a region where W$\leq$2.0 GeV/c^2 was covered and 18 resonances were taken into account.

In Rein and Sehgal's method, the final kinematics of the hadron system are determined so that the effects of the polarization of the produced resonances and the interference are properly considered. In our simulation, we employ their detailed calculations only for $\Delta(1232)$. We simply assume that mesons are emitted isotropically in the resonance rest frame for other resonances.

It is known that a baryon resonance in a nucleus can sometimes be absorbed with no mesons being generated via the following interaction:

$$N^* + N \rightarrow N' + N'' \tag{4.12}$$

where N^* is a baryon resonance and N, N', N" are nucleons. The rate of their interactions is estimated by theoretical calculation [48]. We assume that 20% of the resonances in ^{16}O disappear without meson emissions.

Fermi momentum of nucleons is considered as in the case of quasi-elastic interaction. The Pauli blocking effect on the nucleon from the baryon resonances decay is also taken into account by correcting pion momentum so that the momentum of the nucleon may be larger than 217MeV/c.

4.2.4 Coherent Pion Production off ^{16}O

Coherent pion production is a neutrino interaction with a nucleus as a whole. The differential cross-section of coherent pion production is calculated by Rein and Sehgal [50] as:

$$\frac{d^3\sigma}{dxdyd|t|} = \frac{G_F^2 M}{2\pi^2} f_\pi^2 A^2 E_\nu (1-y) \frac{1}{16\pi} \left[\sigma_{tot}^{\pi^0 N}(E_\nu y)\right]^2 \left(1 + \left(\frac{Re(f_{\pi N}(0))}{Im(f_{\pi N}(0))}\right)^2\right) \times \left(\frac{M_A^2}{M_A^2 + Q^2}\right)^2 exp\left(-\frac{1}{3}R^{2/3}|t|\right) F_{abs} \tag{4.13}$$

where x and y are the Bjorken parameters, t is the square of three-momentum transfer, f_π is the pion decay constant($=0.93 m_\pi$), $f_{\pi N}$ is the pion-nucleon scattering amplitude, A is the atomic number of oxygen, M_A is the axial vector mass, M is the nucleon mass, R is the radius of the oxygen nucleus, $\sigma_{tot}^{\pi^0 N}$ is the averaged cross-section of pion-nucleon scattering, and F_{abs} is the t-independent factor representing the effect of pion absorption in the nucleus.

4.2.5 Deep Inelastic Scattering

The differential cross section for the process is described as follows:

$$\begin{aligned}
\frac{d^2\sigma^{\nu(\bar{\nu})}}{dxdy} &= \frac{G_F^2 M E_\nu}{\pi}\left(\left(1-y+\frac{y^2}{2}+C_1\right)F_2(x,q^2) \pm y\left(1-\frac{y}{2}+C_2\right)\left(xF_3(x,q^2)\right)\right), \\
C_1 &= \frac{ym^2}{4ME_\nu x} - \frac{xyM}{2E_\nu - \frac{m^2}{4E_\nu^2}} - \frac{m^2}{2ME_\nu x}, \\
C_2 &= -\frac{m^2}{4ME_\nu x}
\end{aligned} \tag{4.14}$$

where x, y are Bjorken parameters, $F_2(x,q^2)$ and $xF_3(x,q^2)$ are the nucleon structure functions, M and m are the target nucleon and the outgoing lepton mass, respectively. We adopt the GRV94 parton distribution function [51, 52] for the calculation of F_2 and xF_3.

To remain consistent with the other interaction modes, this interaction is considered in the region where $1.3\mathrm{GeV}/c^2 < W$. The number of produced pions is required to be greater than one a region where $1.3\mathrm{GeV}/c^2 < W < 2.0\mathrm{GeV}/c^2$.

The final kinematics of the hadron system is obtained in two different ways. For a region where $1.3\mathrm{GeV}/c^2 < W < 2.0\mathrm{GeV}/c^2$, the produced mesons are assumed to be pions. We determine the pion multiplicity from a measurement from the FNL seven-foot hydrogen bubble chamber experiment [54]:

$$< n_{\pi^\pm} >= (0.06 \pm 0.06) + (1.22 \pm 0.03)\ln(W^2) \tag{4.15}$$

where $< n_{\pi^\pm} >$ is the mean multiplicity of charged pions. Assuming $< n_{\pi^+} >=< n_{\pi^-} >=< n_{\pi^0} >$, the mean multiplicity of pion $< n_\pi >$ is described as:

$$< n_\pi >= 0.09 + 1.83\ln(W^2) \tag{4.16}$$

For individual Monte Carlo events, the pion multiplicity is determined using KNO (Koba-Nielsen-Olesen) scaling, which describes pion multiplicity distribution with mean multiplicity $< n_\pi >$. We also consider the forward-backward asymmetry of pion multiplicity $(n_\pi^F)/(n_\pi^B)$ in the hadronic center of the mass system [55]:

$$\frac{n_\pi^F}{n_\pi^B} = \frac{0.35 + 0.41\ln(W^2)}{0.5 + 0.09\ln(W^2)} \tag{4.17}$$

where forward is the direction of the hadronic system in the laboratory frame.

For the region where $W > 2.0\mathrm{GeV}/c^2$, the final kinematics of hadrons is determined by the JETSET7.4 package [53], commonly used in high energy physics. The package considers other particle production (K, η, ρ, etc.).

For NC deep inelastic scattering, differential cross-sections are calculated by multiplying factors and CC cross sections estimated from the experimental results shown in Ref. [56, 57]:

$$\frac{\sigma(\nu N \to \nu X)}{\sigma(\nu N \to \mu^- X)} = \begin{cases} 0.26 & (E_\nu \leq 3\text{GeV}) \\ 0.26 + 0.04 \times \frac{E_\nu - 3}{3} & (3\text{ GeV} < E_\nu < 6\text{GeV}) \\ 0.30 & (E_\nu \geq 6\text{GeV}) \end{cases}$$

$$\frac{\sigma(\bar{\nu} N \to \bar{\nu} X)}{\sigma(\bar{\nu} N \to \mu^+ X)} = \begin{cases} 0.39 & (E_\nu \leq 3\text{GeV}) \\ 0.39 - 0.02 \times \frac{E_\nu - 3}{3} & (3\text{ GeV} < E_\nu < 6\text{GeV}) \\ 0.37 & (E_\nu \geq 6\text{GeV}) \end{cases}$$

4.2.6 Nuclear Effects

Particles produced in neutrino interaction undergo secondary interaction before leaving the ^{16}O nucleus. Our simulation considers interactions of π, K, η mesons.

For pions, inelastic scattering, charge exchange, and absorption are considered. The mean free paths are calculated using a model by L. Salcedo *et al.* [58] The momentum and angular distribution of the scattered pions are determined by phase shift analysis using the experimental results on π-N scattering [59]. The density of the nucleon inside ^{16}O is assumed to be in the form of the Saxon-Woods potential [60]:

$$\rho(r) = \frac{Z}{A}\rho_0 \frac{1}{1 + e^{\frac{r-c}{a}}} \tag{4.18}$$

where r is the distance from the center of ^{16}O. $\rho_0 = 0.48 m_\pi^3$, a = 0.41fm, c = 2.69fm, Z = 8 and A = 16, respectively.

Pauli blocking effects in π-N scattering are also considered. Assuming the Fermi gas model, Fermi surface momentum is calculated as follows:

$$P_f(r) = \left(\frac{3}{2}\pi^2 \rho(r)\right)^{\frac{1}{3}}. \tag{4.19}$$

For kaons, elastic scattering and charge exchange are considered. The cross section of the scattering is based on $K^{\pm}N$ scattering measurement [11].

For η, interactions via baryon resonance:

$$\eta + \mathrm{N} \to \mathrm{N}^* \to \mathrm{N} + \mathrm{X} \tag{4.20}$$

are considered. Where X is either η, π, or $\pi\pi$, N* is either N(1535) or N(1650) [11]. Cross section of interactions are given by Bright-Wigner form:

$$\sigma(k) = \frac{\pi}{k^2} \frac{\Gamma_{\eta \mathrm{N}} \Gamma_{\mathrm{X}}}{(W - M_{\mathrm{N}^*})^2 + \Gamma_{tot}^2/4} \tag{4.21}$$

where k is the momentum of η, $\Gamma_{\eta N}$ is a partial decay width of the interaction $N^* \rightarrow N + \eta$, and Γ_X is a partial decay width of $N^* \rightarrow N + X$, respectively.

4.2.7 Rescattering of Proton

The recoil proton in charged current interaction can be rescattered by the nucleon inside the nucleus. The probability of this nucleon-nucleon final state interaction is estimated from the measurement of a scattered angle of protons in electron scattering on ^{12}C target [61];

$$e + {}^{12}C \rightarrow e' + p + X. \tag{4.22}$$

The proton at scatter angle θ at 66° and 120° was measured at their experiment. The ratio between the two angles is:

$$R(120 \pm 8^\circ)/(66 \pm 8^\circ) = 0.019 \pm 0.0001 \tag{4.23}$$

We tuned the probability of the final state interaction in our ν_e simulation by observing the proton scattering angle. Figure 4.2 shows the scattering angle distributions for ν_e MC with and without final state interaction. $R(120\pm8^\circ)/(66\pm 8^\circ)$ is $0.023 \pm 0.002(stat.)$ for our MC.

4.3 Detector Response

4.3.1 FGSIM

Our detector simulation utilizes GEANT 3.21, developed by CERN [37]. GEANT is fed detector geometry input and then simulates the passage of elementary particles through matter. In K2K, GEANT transports particles through the FGD. The simulation of detector response obtained graphically represents both the FGD and particle trajectories. This is known as FGSIM. The GEANT package includes a variety of materials. When the exact material used in the detector is unavailable, GEANT can create a similar compound from atoms inside the program.

We set up the program to describe the response of the SciFi detector under FGSIM. It is divided into two parts: the calculation of the light yield of SciFi and pixel simulation.

Light Yield of SciFi We made a conversion table of the deposit energy inside SciFi calculated by GEANT and the light yield (the number of photo electrons measured by the PMT). The light yield of SciFi is calibrated using a cosmic ray muon or ^{90}Sr source [28]. Attenuation in the SciFi and reflection from the aluminum coating at the edges is also considered.

Pixel Simulation To construct a reliable MC detector simulation, data of the response of the IIT-CCD part is taken using a calibrated LED. The data is parameterized and reproduced by the MC [62]. The set up of the calibration is shown in Figure 4.3. We can analyze simulated CCD pixels and reconstruct neutrino events with this data as if it were raw data from a neutrino beam run. (The analysis procedure is described in Chapter 5.)

4.3.2 Water Čerenkov Detectors

The detector simulation programs of 1kt and SK water Čerenkov detectors use the same technique.

Transportation of particles The simulation program is based on the same GEANT package used on the FGD.

Emission and propagation of Čerenkov light A water Čerenkov detector observes relativistic charged particles via their emission of Čerenkov light. Čerenkov radiation is a shock wave created by a relativistic charged particle with a velocity greater than the light velocity in the medium:

$$v \geq \frac{c}{n} \tag{4.24}$$

where v is the particle velocity and n is the refractive index of the medium. Generated photons propagate in water with a group velocity c/n. Rayleigh scattering, Mie scattering, and the absorption of the photon are considered. The parameters of their interactions are tuned with cosmic ray muon data.

Detection of Čerenkov light The number of photons arriving at the surface of the PMT is converted to the number of photoelectrons, with consideration to the quantum efficiency of PMTs.

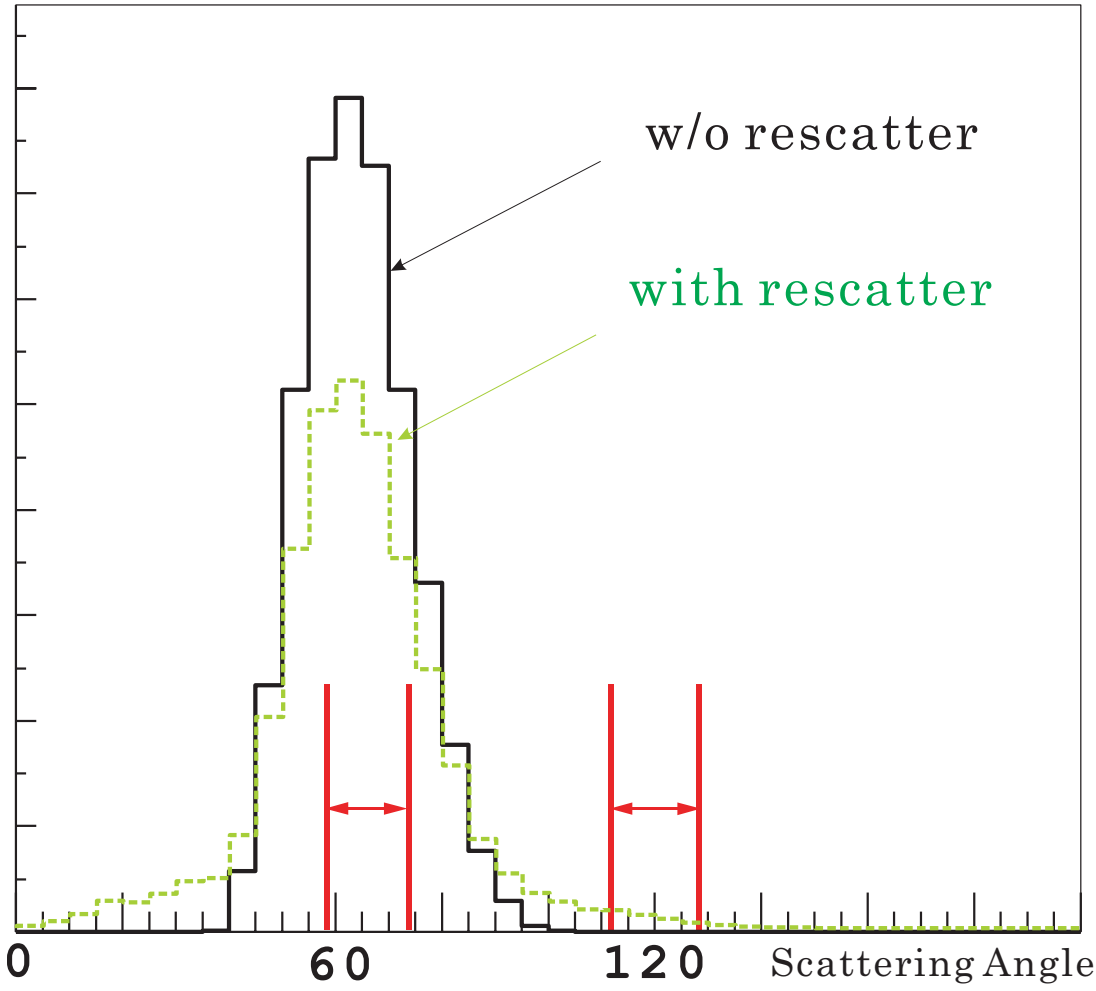

Figure 4.2: Scattering angle distributions for ν_e MC with and without final state interaction. Alanakyan *et, al.* measured proton number ratio between the scattered angle $120 \pm 8°$ and $66 \pm 8°$.

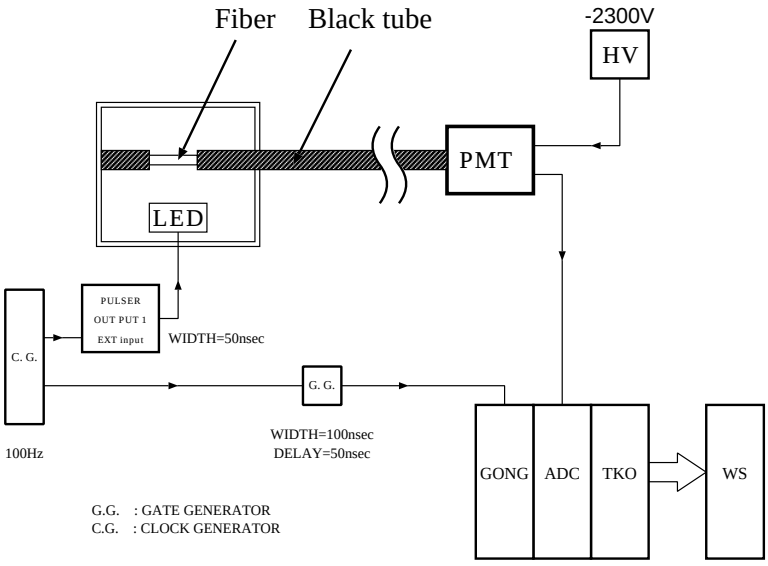

Figure 4.3: Setup of LED calibration.

Chapter 5

Analysis Procedure of the SciFi Detector

This chapter describes neutrino event reconstruction. Analysis begins with the search for fiber hits in CCD pixel information. SciFi tracks are then reconstructed. Hits are connected hits using straight fitting. Additionally, we match tracks between the SciFi and downstream FGD components. Our goal is to reconstruct muon energy and track multiplicity for neutrinos events inside the SciFi.

5.1 Hit Finding

Hits in the SciFi detector are reconstructed from CCD pixel images. Figure 5.1 (a) shows a typical CCD image of a cosmic-ray event from an IIT. Figure 5.1 (b) is an expanded view of (a). The circles in the figures represent the coordinates of the SciFi in an expanded view of (a). The figures illustrate a typical SciFi hit where a cosmic-ray muon passes through the fiber sheet.

There are four steps to hit reconstruction:

1. **Hit Pixels in CCD Camera View**
   As explained in Chapter 3.4, raw data from the SciFi detector consists of hit pixels in CCD coordinates (x, y) in 8-bits of ADC brightness. These are encoded one word per pixel. There are typically 3500 hit pixels in a neutrino event.

2. **Pixel Clustering**

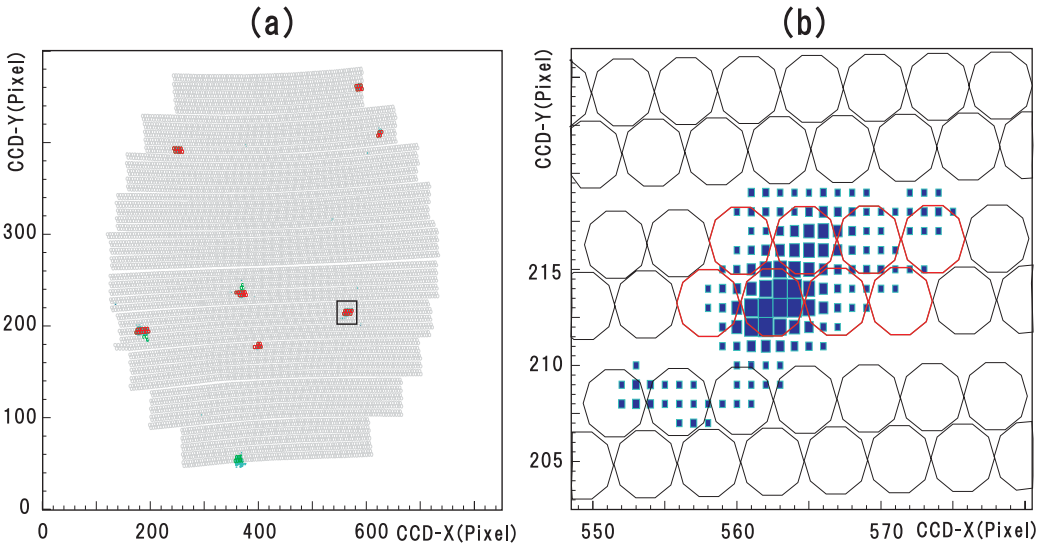

Figure 5.1: (a) A typical CCD image of a cosmic-ray event. (b) This expanded view of (a) shows a typical SciFi hit. Circles inside the figures represent the coordinates of the SciFi in the CCD view. The size of hit pixel is proportional to the brightness in the ADC. Hit fibers are represented by the thick circles. A SciFi hit is defined as a cluster of neighboring hit fibers.

A pixel cluster is a group of neighboring hit pixels. Isolated single-pixel hits from random electrical noise in the CCD are rejected here.

3. **Identifying Hit Fibers**
   Identification of a hit fiber requires a cluster of pixels at the fiber positions. The CCD coordinates of the hit fiber position is determined with a mapping table obtained from EL calibration.

4. **Hit Fiber Clustering**
   A fiber cluster is defined as a group of neighboring hit fibers. We define fiber clusters as hits in the SciFi detector.

We apply two kinds of filtering algorithms to the fiber clusters to improve the signal-to-noise ratio:

- A fiber cluster is required to consist of hit fibers in both the upper and lower layers of a fiber sheet (See Figure 3.8). This eliminates the small pixel clusters caused by dark current in the IIT.

- When a big pixel cluster lies on an adjacent fiber sheet and forms multiple fiber clusters, only fiber clusters with peak ADC brightness are chosen, which eliminates fake fiber clusters formed by the dense bundle arrangement of fiber sheets.

Every hit in SciFi detector must pass these filters. The hit position is defined as the centroid of a fiber cluster, weighted by the ADC value of the hit pixel. The hit position CCD coordinates are then converted into detector coordinates (x, z or y, z) in our experimental hall.

5.2 Event Reconstruction

After finding the hits, we look for neutrino events in the SciFi detector. Tracks are used for event reconstruction. These tracks are then classified and matched with the FGD components and their track information.

Tracks in the SciFi detector are classified as either first or second tracks. The first track is for muons generated in charged current (CC) interaction. The second tracks are for other particles such as protons or pions. When two or more tracks are found, we define the vertex of the tracks as the interaction point of the incoming neutrino.

5.2.1 First Track Finding

The first track-finding algorithm in the SciFi detector is optimized for charged current interactions which contain one muon in the final state [35, 36]. There are three steps to the track-finding algorithm, which is designed to remove combinatorial background or noise tracks.

Firstly, the track finder searches for two-dimensional (2D) track candidates on the (x, z) or (y, z) planes which traverse at least three layers of SciFi detector. A three-dimensional track is reconstructed from the best combination of two 2D tracks. In order to eliminate combinatorial fake tracks, the start and end of hit layers must not differ by more than one layer and the two 2D tracks must overlap at least two layers.

Secondly, a track candidate must reach the edge of the SciFi detector. It cannot be a contained event.

Finally, a track candidate must match a hit in the downstream trigger counter. This will be described in the next subsection, 5.2.2.

5.2.2 Track Matching with TRG Counter

If a muon produced via the charged current interaction inside of SciFi detector goes forward, it will register as a hit in downstream TRG counters. Hits must register in TRG counters on the extrapolated line of SciFi tracks. The matching criteria is $\pm$10cm for the x and $\pm$50cm for the y direction. Only events with at least one track matching TRG counters are classified as "TRG matching" and used in further analysis.

5.2.3 Track Matching Veto with VETO Counter

To avoid incoming muons from neutrino interactions inside 1kt or the beam dump, SciFi tracks with VETO counter hits along the extrapolated line to the upstream detector are eliminated. The matching criteria is $\pm$20cm and $\pm$50cm in directions x and y, respectively.

5.2.4 Track Matching with LG

SciFi tracks that match with TRG counters are extrapolated to the position of the downstream LG. If the extrapolated track lines and LG blocks intersect, the LG hit cluster requires an energy deposit greater than 100MeV for the event to be considered an "LG matching sample".

5.2.5 Track/Hit Matching with MRD

If an LG matching sample has an MRD track or a hit in the first layer of MRD, its track or hit is examined. As low-energy muons can scatter multiple times, a range of positions and angles between the SciFi track and MRD tracks is permitted. Events which pass MRD matching are known as "MRD events". Events which fail MRD matching are known as "LG stopping events", or in the following chapters, "LG events". Only these event samples were used in our analysis.

5.2.6 Second Track and Vertex Finding

Once a good, energetic first track is found, the most upstream hit position is defined as the neutrino interaction point. The second track finder begins searching for extra tracks near this point. These tracks are mostly short tracks with two or more SciFi hits. Many of them come from protons or pions from the interaction.

If no short tracks are found near the starting point of the first track, the event is considered a one-track event. If an event has one short track, it considered a two-track event. If the second track finder identifies more than two tracks, the event is a three-track event (or more).

A vertex is defined as the intersection of the first and second tracks. For one-track events, the vertex is taken from the middle point of the closest upstream water tube to the track.

After locating the second track, we can classify an event by track multiplicity. Figure 5.2 is an example of a two-track MRD event.

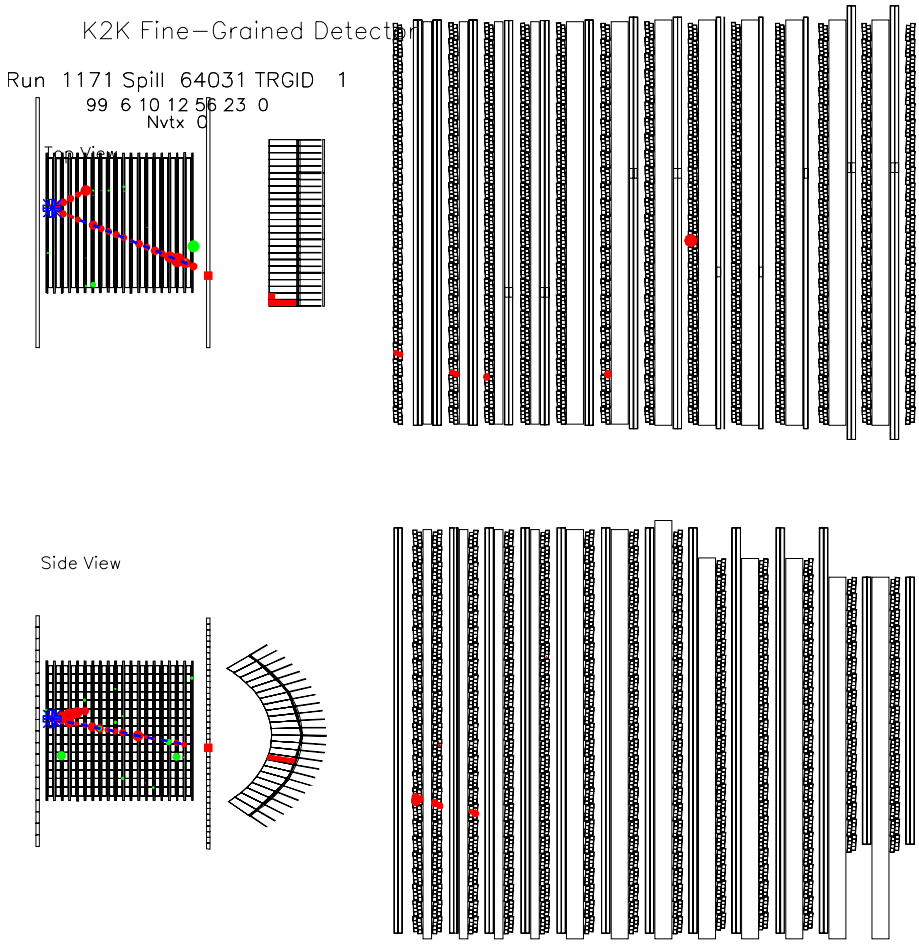

Figure 5.2: Example of a SciFi two-track MRD event. The upper figure is the top view, the lower figure the side view.

Table 5.1: SciFi event summary table. Common selection of FGD requires at least one FGD component has activity.

Selection	Jun 1999	Nov 1999-Jun 2000	Jan 2001-Jul 2001
Common selection of FGD	156747	1135983	1633558
SciFi has track	7035	102081	148284
TRG match	2192	14762	22266
Bad run cut	1582	12588	19417
VETO match veto	1118	8923	13734
MRD match	295	3261	5132
LG stopping	-	1473	2156

5.2.7 Muon Energy Reconstruction

Muon energy is calculated from its range. For the SciFi, LG, and Veto, a GEANT table is used to calculate deposit energy from path lengths in the detectors. For MRD, a conversion table of range in iron and muon energy is used. The difference between the GEANT table and table used for the MRD was confirmed as at most 1.7%. We sum up the deposit energy for all FGD hits or tracks related to the first track muon. Finally, muon mass (=105.658389MeV) is added.

5.3 Event Summary

K2K ran in June 1999, in November 1999, from January to July in 2000, and from January to July in 2001. We collected 8688 MRD events and 3629 LG events in total over two years. The summary table 5.3 shows the reduction of the data at each step of analysis. Common selection of a FGD event requires that at least one of the FGD components has activity. The bad run cut is described in subsection 6.1.1. In total, 12317 SciFi events were obtained.

In June 1999, MRD events with tracks in MRD were counted and LG events and MRD events with hits in first layer of the MRD were discarded. This was done because systematic errors for these samples were not estimated during this period. Until June 1999, a different magnetic horn current and target size were used.

5.4 Performance of SciFi Detector

5.4.1 Hit Finding Efficiency

Hit finding efficiency for all 24 IITs is estimated from cosmic ray data samples. FGD cosmic ray samples are triggered by coincidence of veto/trigger scintillators. For each event, a cosmic ray muon is required to penetrate more than 15 layers of the SciFi detector to be accepted as a SciFi cosmic ray data sample.

The definition of the hit finding efficiency is as follows:

$$Hit\ finding\ efficiency \equiv \frac{Number\ of\ layers\ with\ hits}{Number\ of\ penetrated\ SciFi\ layers.} \tag{5.1}$$

The results are shown in Figure 5.3. Estimated efficiency for 24 IITs in MC detector simulation are shown. MC data agrees remarkably well.

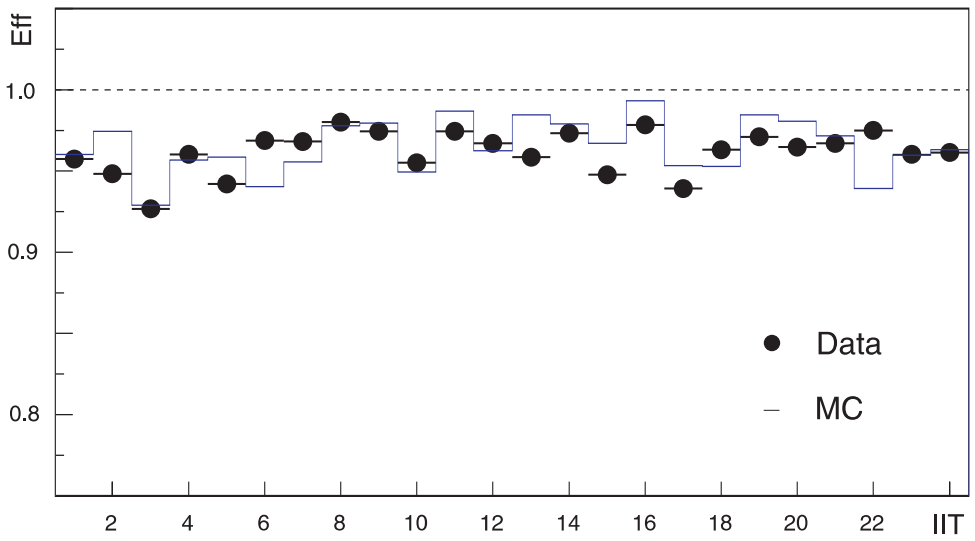

Figure 5.3: Hit finding efficiency of 24IITs.

The stability of the efficiency is also studied. For K2K runs, our accelerator group had machine study time for a few hours on Monday mornings. We obtained cosmic ray data during this time and checked its efficiency over the long term. Figure 5.4 shows the efficiency for this period. It is stable to within ~2%.

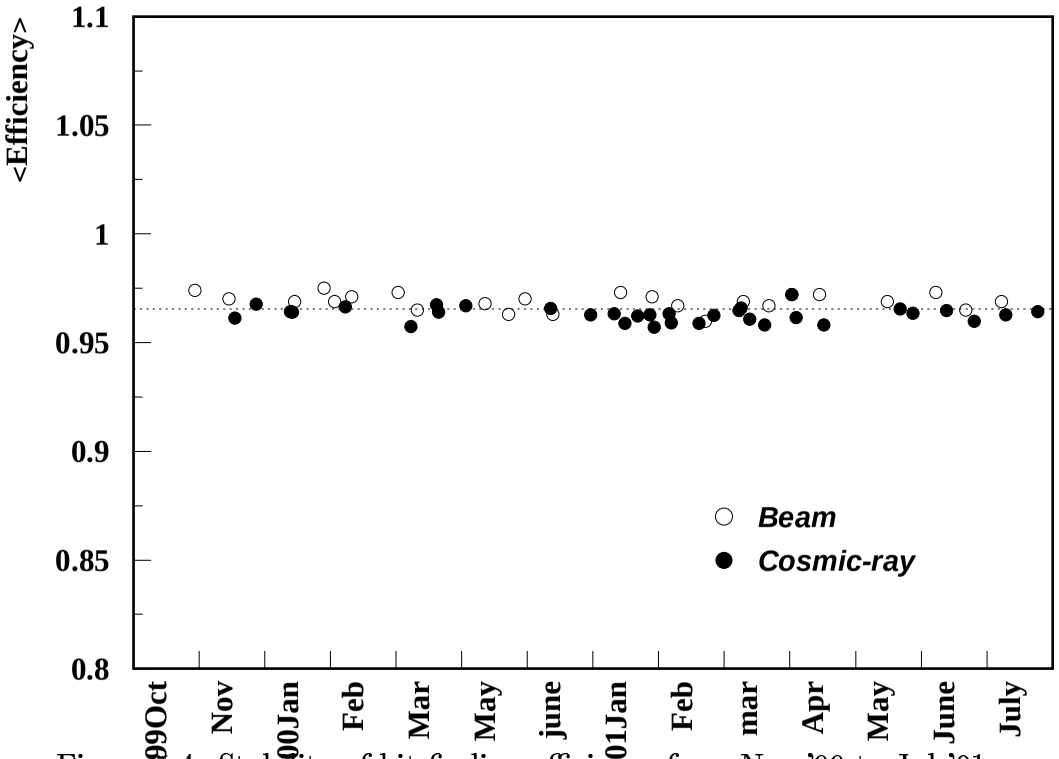

Figure 5.4: Stability of hit finding efficiency from Nov '99 to Jul '01.

5.4.2 Track Finding Efficiency

Figure 5.5 shows track finding efficiency in the SciFi detector as a function of track length, or number of layers. Track finding efficiency is defined as:

$$Track\ finding\ efficiency \equiv \frac{Number\ of\ events\ with\ track\ between\ scintillators}{Number\ of\ cosmic\ ray-triggered\ events.} \tag{5.2}$$

In order to understand the dependence of the track finding efficiency on track length, hits on the upstream side of the track are artificially eliminated. For example, to estimate the efficiency of ten SciFi hit layers using a 19-layer track, the first nine hit layers are eliminated before applying a track-finding algorithm. Figure 5.5 shows track finding efficiency as a function of track length in SciFi layers with cosmic ray data.

Track finding inefficiencies are the result of hit finding failures and imperfections in the track reconstruction.

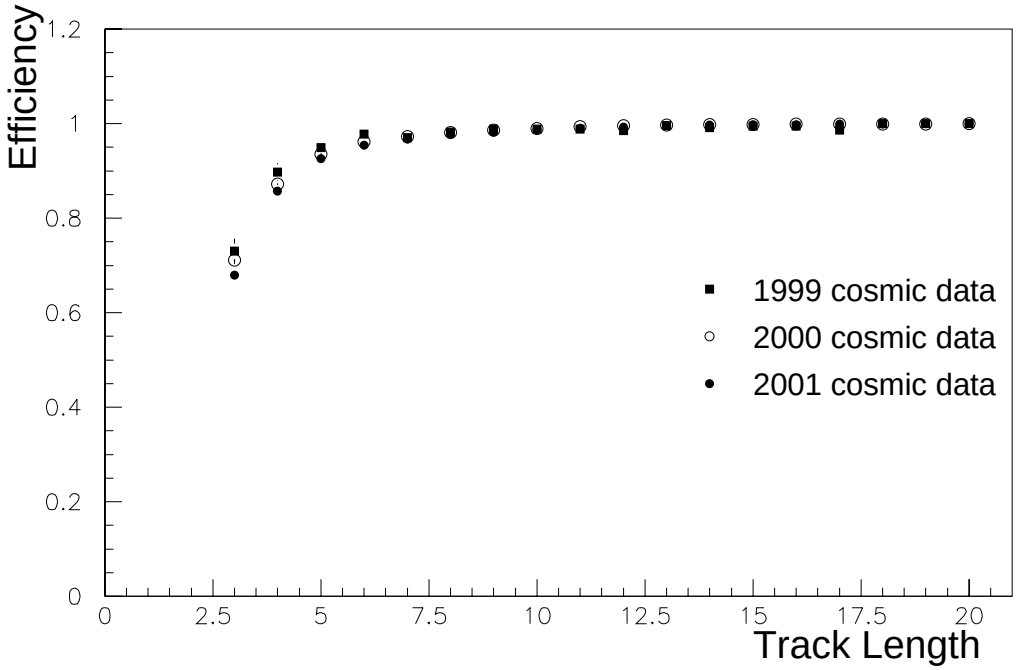

Figure 5.5: Track finding efficiency as a function of the track length. Efficiency is ~70% (~87%) in a track length of the three (four) SciFi layers and approaches 100% in longer tracks.

5.4.3 Hit Position Resolution

The geometry of the SciFi and its support structure was measured after installation. According to this survey, fiber alignment is estimated to be within 5mm. Closer alignment was obtained by minimizing the sum of the squared hit-residuals using a global fit on cosmic ray tracks [36].

Slight curvature of the fiber sheets occurred as they were glued to the fiber modules. This caused displacement from the aligned fiber-position and resulted in rotational misalignment. The curvature of each fiber sheet was measured after fiber module assembly. By fitting the measured points to a forth-order polynomial, the curvature of the sheets was accounted for in corrections of rotational misalignment.

For position resolution, the muon tracks from the neutrino data are used to

obtain the best estimation. Figure 5.6 shows the hit residual distribution of the neutrino data. The position resolution is 0.73mm (0.61mm) for muon energy E_μ < 1GeV (E_μ > 1GeV). The overall position resolution is 0.64±0.07mm.

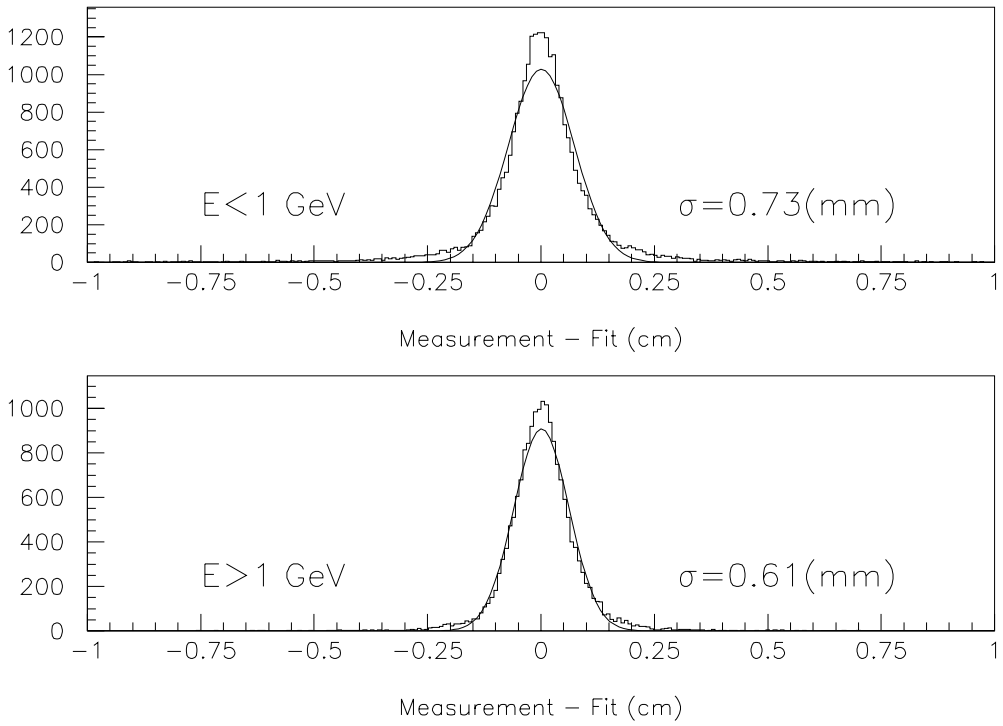

Figure 5.6: Hit residual distributions using neutrino beam data. The curve is a single Gaussian fit to the data with σ = 0.73mm (0.61mm) for muon energy E_μ < 1GeV (E_μ > 1GeV).

5.4.4 Noise Rate

Noise hits in the SciFi detector were tracked to the following sources:

1. Contamination from cosmic rays or penetrating muons
2. Dark current of IIT
3. Fake hits made by large pixel clusters

4. Electrical noise in the CCD

These hits were reproduced in our detector simulation by histograming each noise using cosmic ray or random triggered data. The averaged number of noise hits is 56 per one data event.

Chapter 6

Expected Number of Neutrino Events at SK

In this chapter, we assume a null-oscillation case and calculate the estimated number of neutrino events at SK ($N_{\rm SK}$) from the number of SciFi detector events. As shown in Chapter 1, ν_μ deficit will be observed if neutrinos oscillate. The probability of no oscillation is derived from the $N_{\rm SK}$ statistical estimation in Chapter 9.

6.1 Total Number of Protons on Target (POT)

Figure 6.1 shows the integrated number of protons injected to the target from 1999 to 2001. Following an engineering run from March 1999, our physics run started in June. The number of protons delivered to the target (POT) from June 1999 to July 2001 totaled 5.6×10^{19}. In the June 1999 run, the target was 2cm in diameter and the horn current was 200kA. This is known as "the June configuration". In November 1999, a 3cm diameter target and 250kA horn current were adopted. This is known as "the November configuration". Data from both configurations were used to calculate $N_{\rm SK}$.

6.1.1 $\rm POT_{SK}$ and $\rm POT_{SciFi}$

The observed number of events at the near and far detectors must be normalized to take into account beam condition and detector live time. "Bad run" periods were due to the following reasons:

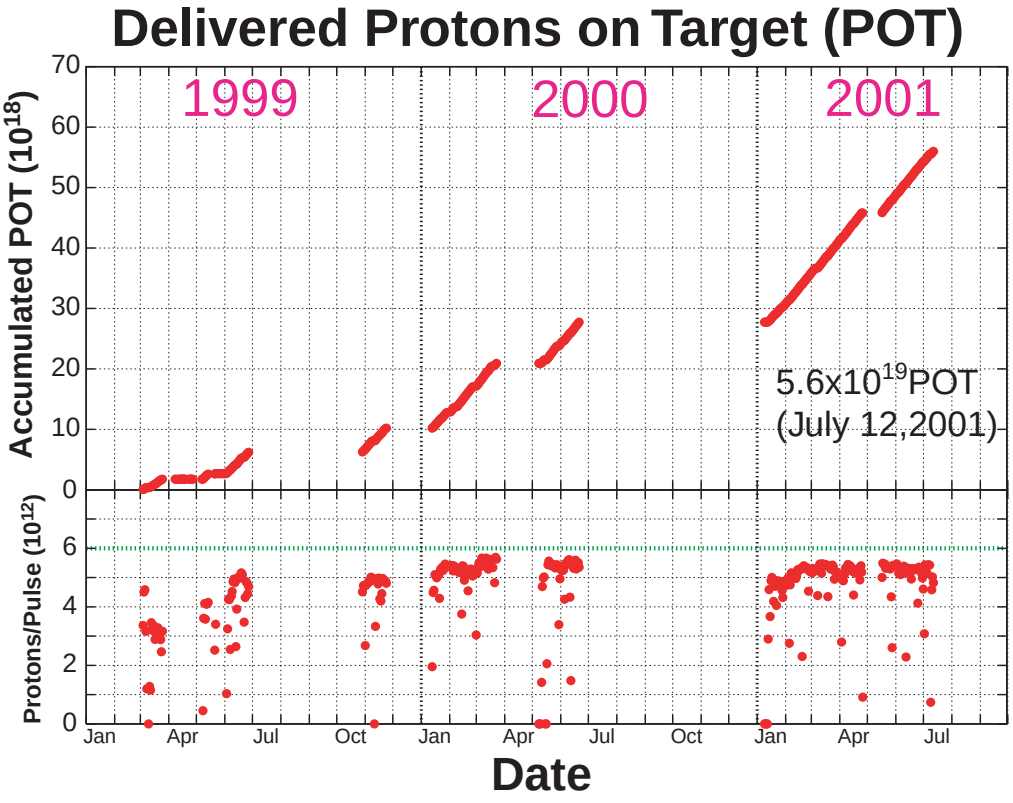

Figure 6.1: Top figure shows integrated number of protons on target from 1999 to 2001. Bottom one shows number of protons per pulse in same period.

- Bad beam conditions or unexpected beam downs (at least 1.0×10^{12} protons per pulse were required)
- Maintenance work on the detectors during beam time
- Calibration runs of the SK detector during beam time
- DAQ failure of the beam line and/or detectors

These periods were subtracted from the delivered POT. $\mathrm{POT_{SK}}$ and $\mathrm{POT_{SciFi}}$ are the integrated POTs for the far and near detectors. They are 4.79×10^{19} and 4.20×10^{19}, respectively.

6.2 Neutrino Beam Aiming and Targeting

Neutrino beam direction is monitored by the muon monitor (subsection 2.4.2). Figure 6.2 shows aiming stability. The solid line points in the direction of the far detector. The broken lines correspond to $\pm$1mrad. difference from this direction. From this we can conclude that the neutrino beam is aimed to within $\pm$1mrad. of SK. [24, 63].

The pion monitor and the beam MC simulation are utilized to study the SK neutrino beam profile. Figure 6.3 shows neutrino beam flux around SK in MC (at 10×20 POT). Neutrino flux reduction at 1km from the axis (4mrad) is within 3%. The muon monitor guaranteed $\pm$1mrad accuracy to the beam direction.

6.3 Neutrino Event Rate at SciFi

Figure 6.4 shows the rate of MRD and LG stopping events per month. After normalization by $\mathrm{POT}_{\mathrm{SciFi}}$, this rate can be considered reasonably stable and we can conclude that a constant neutrino beam was delivered to SK during this period.

6.4 N_{SK} Calculation

The number of neutrino events at SK(N_{SK}) is calculated with the following formula:

$$N_{\mathrm{SK}} = N_{\mathrm{SciFi}} \frac{\epsilon_{\mathrm{SK}}}{\epsilon_{\mathrm{SciFi}}} \cdot R_{\mathrm{SK/Near}} \cdot \frac{\mathrm{POT}_{\mathrm{SK}}}{\mathrm{POT}_{\mathrm{SciFi}}}, \tag{6.1}$$

where

$$R_{\mathrm{SK/Near}} = \frac{\Phi_{\mathrm{SK}} \cdot Nt_{\mathrm{SK}}}{\Phi_{\mathrm{Near}} \cdot Nt_{\mathrm{SciFi}}}, \tag{6.2}$$

N_{SciFi} is the number of observed events at the SciFi detector,
Φ_{SK} is neutrino flux at SK,
Φ_{Near} is the neutrino flux at the SciFi detector,
Nt_{SK} is the number of water target in the SK fiducial volume (25kton),
Nt_{SciFi} is the number of water target in the SciFi fiducial volume (5.9kton),
ϵ_{SK} is the SK detection efficiency, and
$\epsilon_{\mathrm{SciFi}}$ is the SciFi detection efficiency.

6.4.1 Neutrino Flux Ratio of Far and Near Detectors

We estimate $\Phi_{\rm SK}$ and $\Phi_{\rm Near}$ from the pion monitor measurement of neutrinos with energy $\geq$ 1GeV (Subsection 2.4.1). To estimate below 1GeV, we use the MC simulation of models of pion production [49]. Error caused by the uncertainty of the estimated neutrino flux can be reduced by taking the ratio $R_{\rm SK/Near}$:

$$R_{\rm SK/Near} \equiv \frac{\Phi_{\rm SK}}{\Phi_{\rm Near}}. \tag{6.3}$$

Figure 6.5 shows the neutrino spectrum at KEK and SK with $R_{\rm SK/Near}$ the November configuration. Measured and MC estimations are in agreement for neutrinos with energy above 1GeV. We conclude that the MC model utilized is reasonable and $R_{\rm SK/Near}$ from MC is therefore used in the calculation in the next section.

6.4.2 SciFi/SK Efficiency

Figure 6.6 shows SK and SciFi detection efficiency, or MRD events, of neutrinos as functions of neutrino energy. This is defined as (*observed neutrino events) / (generated neutrino events in the fiducial volume*) for both detectors and is estimated by MC simulation. Where SK is sensitive to approximately half of NC (neutral current) events, the SciFi detector is insensitive to most (NC is estimated to be 0.5% of total reconstructed MRD events). The SciFi detector has a low efficiency for neutrinos with an energy of less than 1 GeV as SciFi requires muons from interactions to either have tracks or register as hits in downstream detector (Chapter 5).

6.5 Source of $N_{\rm SK}$ Systematic Error

Summary tables of systematic error terms for $N_{\rm SK}$ are shown in Tables 6.2, 6.3, 6.4. Each term is explained below.

6.5.1 Error Terms from FGD

Fiducial Volume This is examined using a cosmic ray data sample. We masked part of the penetrating cosmic ray track to test that the software finds vertices correctly. We assigned an error of $\pm$1%.

Event Reconstruction We take the difference between the data and MC of the SciFi detector first track finding efficiency as an error. Using cosmic ray data, it is examined and an error of $\pm 3\%$ is assigned. Track connection efficiency between a SciFi track and the downstream detectors hit is counted as an error term. The difference between the data and MC efficiencies is taken. These are $\pm 1\%$, $\pm 1\%$, and $\pm 2\%$ for TRG counters, LG, and MRD respectively. A quadratic sum of all numbers is also taken: $\pm 3.9\%$.

Aluminum Cross Section SciFi detector target water is in 2mm thick aluminum tanks. Each layer of the tank is 4mm of aluminum and 6cm of water. 15% of the total weight is aluminum. Assuming that neutrino cross sections in aluminum differ $\pm 20\%$ from the same weight of water, the SciFi event rate therefore has a $\pm 3\%$ error ($20\% \times 15\%$).

6.5.2 Error Terms from Extrapolation to Far Detector

Neutrino Spectrum Difference between the efficiencies of SciFi($\epsilon_{\rm SciFi}$) and SK($\epsilon_{\rm SciFi}$) are shown in Figure 6.6. Shape difference can contribute to an $N_{\rm SK}$ error. The Eqn. 6.1 can be rewritten as follows:

$$N_{\rm SK} = N_{\rm SciFi} \cdot \left[\frac{N_{\rm SK}}{N_{\rm SciFi}}\right]_{MC} \tag{6.4}$$

where $N_{\rm SK}$ and $N_{\rm SciFi}$ in the MC square parenthesis are

$$\begin{aligned} N_{\rm SK} &= \epsilon_{\rm SK} \cdot \Phi_{\rm SK} \cdot Nt_{\rm SK} \cdot {\rm POT}_{\rm SK}, \\ N_{\rm SciFi} &= \epsilon_{\rm SciFi} \cdot \Phi_{\rm SciFi} \cdot Nt_{\rm SciFi} \cdot {\rm POT}_{\rm SciFi}. \end{aligned} \tag{6.5}$$

If the neutrino flux at near site has an error of $\Delta\Phi$, $N'_{\rm SK}$ will be:

$$N'_{\rm SK} = N_{\rm SciFi} \cdot \left[\frac{N_{\rm SK} + \sum_i \left(\frac{\Delta\Phi}{\Phi}\right)_i \cdot n_i^{\rm SK}}{N_{\rm SciFi} + \sum_i \left(\frac{\Delta\Phi}{\Phi}\right)_i \cdot n_i^{\rm SciFi}}\right]_{MC} \tag{6.6}$$

where i shows energy bin $1 \sim 6$,

$$\sum_{i=1}^{6} n_i = N. \tag{6.7}$$

$N'_{\rm SK}$ can be transformed

$$N'_{\rm SK} = N_{\rm SciFi} \left[\frac{N_{\rm SK}}{N_{\rm SciFi}} \cdot \frac{1 + \sum_i \left(\frac{\Delta\Phi}{\Phi}\right)_i \frac{n_i^{\rm SK}}{N_{\rm SK}}}{1 + \sum_i \left(\frac{\Delta\Phi}{\Phi}\right)_i \frac{n_i^{\rm SciFi}}{N_{\rm SciFi}}}\right]_{MC} \tag{6.8}$$

$$\sim \quad N_{\rm SK}\left[1+\sum_{i=1}^{6}\left(\frac{\Delta\Phi}{\Phi}\right)_i\frac{n_i^{\rm SK}}{N_{\rm SK}}-\sum_{i=1}^{6}\left(\frac{\Delta\Phi}{\Phi}\right)_i\frac{n_i^{\rm SciFi}}{N_{\rm SciFi}}\right]$$

and so the error term is

$$\sum_{i=1}^{6}\left(\frac{\Delta\Phi}{\Phi}\right)_i\cdot\left(\frac{n_i^{\rm SK}}{N_{\rm SK}}-\frac{n_i^{\rm SciFi}}{N_{\rm SciFi}}\right)_{MC}. \tag{6.9}$$

The result for MRD events is $\pm 2.7\%$.

Ratio of charged current interaction and neutral current interaction (CC/NC ratio) Although SK is sensitive to approximately half of NC events, the SciFi detector is insensitive to most, and therefore the CC/NC ratio gives an error of event numbers. The uncertainty of the CC/NC ratio in water is approximately 30%. We estimate the error from the CC/NC ratio by changing it $\pm 30\%$ inside the MC simulation. This gives an overall change of $\pm 4.1\%$

Inelastic/Elastic Interaction Ratio This term also comes from the uncertainty of the interaction. We estimated the error from the inelastic/elastic interaction ratio by changing it $\pm 20\%$ in MC simulation. The result is $^{+5.6\%}_{-7.1\%}$. $\pm 20\%$ is given by the result of spectrum fitting described in Chapter 7.

Far/Near Flux Ratio Far/Near flux ratio is given by the pion monitor. The error comes primarily from fitting and is $^{+5.6\%}_{-7.1\%}$

CT Normalization The near detector monitors the event rate. The dead time of the near detector and SK is corrected by POT. The error is estimated from $RMS\ of\ (neutrino\ interactions/CT)\ \times\ dead\ time$, $\pm 1\%$.

SK Efficiency Vertices in SK events must be inside the 22.5 kt fiducial volume. The vertex is reconstructed using "TDC fit". We checked the vertex position of the selected SK events against an alternative fitting method. In MC simulation, the two results show a $\pm 2\%$ difference. This is taken as an SK event error term. Additionally, the statistical error of the MC event sample is approximately $\pm 1\%$.

Table 6.1: Numbers used in N_{SK} calculation.

Terms	Jun.99	Nov.99-Jun.00	Jan.01-Jul.01
Nt_{SK} (kton)	25000	25000	25000
Nt_{SciFi} (ton)	8.624	8.624	8.624
ϵ_{SK}	0.7810	0.7847	0.7847
ϵ_{SciFi}	0.165	0.2557	0.2557
$POT_{SK}(\times 10^{19})$	0.3099	1.985	2.500
$POT_{SciFi}(\times 10^{19})$	0.2273	1.589	2.381
N_{SciFi}	295	4734	7288
N_{SK}	5.25	35.10	45.55

6.6 N_{SK} from the SciFi Detector

N_{SK} from the SciFi Detector is calculated by Formula 6.2 and the numbers listed in Table 6.1.

$$N_{SK} = 85.9 \pm 1.0(stat.)^{+7.8}_{-8.5}(sys.). \quad (6.10)$$

Note: The official number given by the K2K collaboration refers to N_{SK} from the 1kton water Čerenkov detector, $80.6 \pm 1.0(stat.)^{+6.2}_{-5.4}(sys.)$.

Table 6.2: Systematic error terms table of N_{SK} for MRD events. (November Config.)

Error Source (November config.)	+	-
Fiducial Volume	1.0%	1.0%
Event Reconstruction	3.9%	3.9%
Aluminum Cross Section	3.0%	3.0%
Neutrino Spectrum	3.0%	3.0%
Inelastic/Elastic Ratio	3.3%	4.0%
CC/NC Ratio	4.1%	4.1%
Far/Near Flux Ratio	5.6%	7.1%
CT Normalization	1.0%	1.0%
SK Efficiency	3.0%	3.0%
Total	10.2%	11.4%

Table 6.3: Systematic error terms table of N_{SK} for LG events. (November config.)

Error Source (November config.)	+	-
Fiducial Volume	1.0%	1.0%
Event Reconstruction	3.7%	3.7%
Aluminum Cross Section	3.0%	3.0%
Neutrino Spectrum	2.0%	2.0%
Inelastic/Elastic Ratio	1.0%	1.0%
CC/NC Ratio	3.0%	3.0%
Far/Near Flux Ratio	5.6%	7.1%
CT Normalization	1.0%	1.0%
SK Efficiency	3.0%	3.0%
Total	8.5%	9.6%

Table 6.4: Systematic error terms table of N_{SK} for MRD events. (June config.)

Error Source (June config.)	+	-
Fiducial Volume	1.0%	1.0%
Event Reconstruction	3.9%	3.9%
Aluminum Cross Section	3.0%	3.0%
Neutrino Spectrum	4.4%	4.4%
CC/NC Ratio	4.3%	4.3%
Inelastic/Elastic Ratio	5.6%	7.2%
Far/Near Flux Ratio	13.6%	9.6%
CT Normalization	1.0%	1.0%
SK Efficiency	3.0%	3.0%
Total	17.0%	14.9%

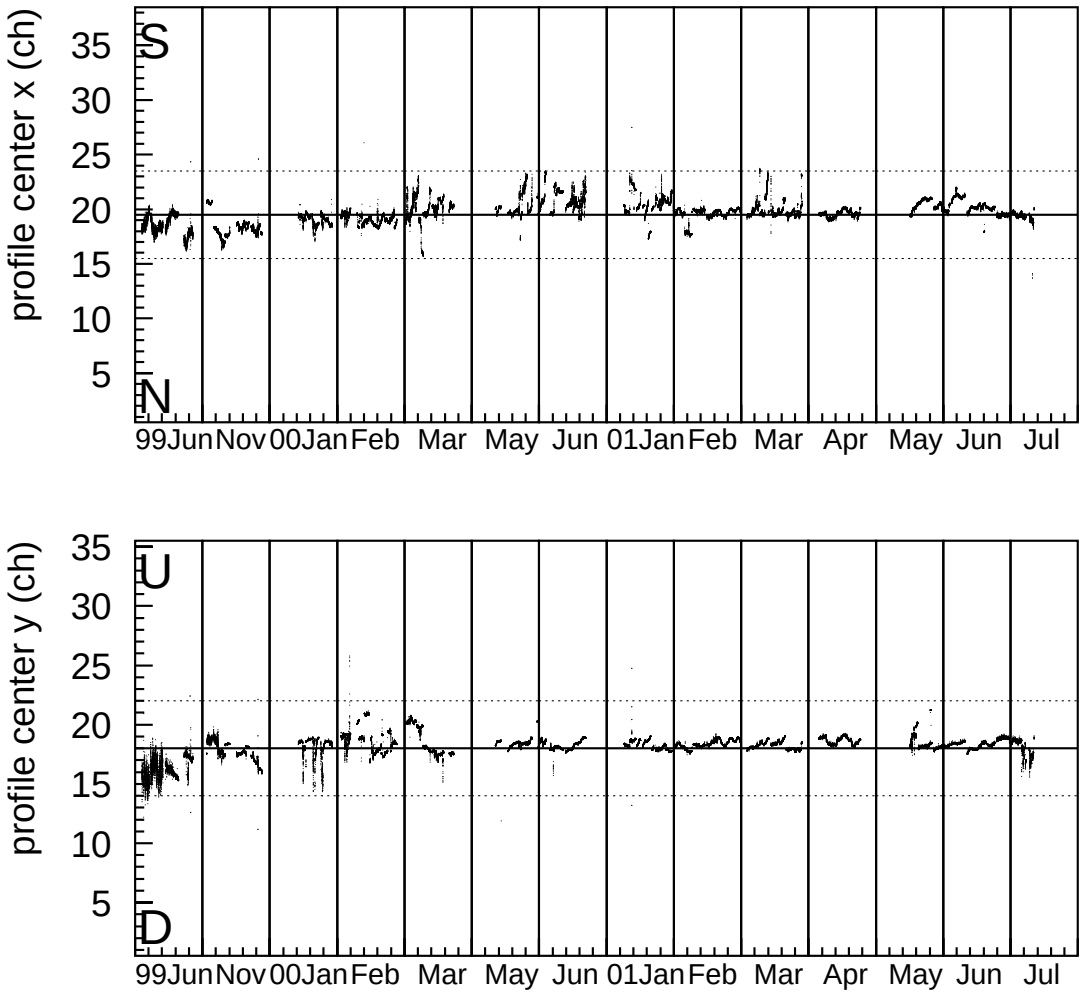

Figure 6.2: Neutrino beam direction stability measured by the muon monitor (ionization chamber). The top figure shows the horizontal profile, the bottom figure the vertical. The X-axis is months; The Y-axis is the readout channel. The solid line points in the direction of the far detector. The broken lines correspond to within $\pm$1mrad. difference from this direction.

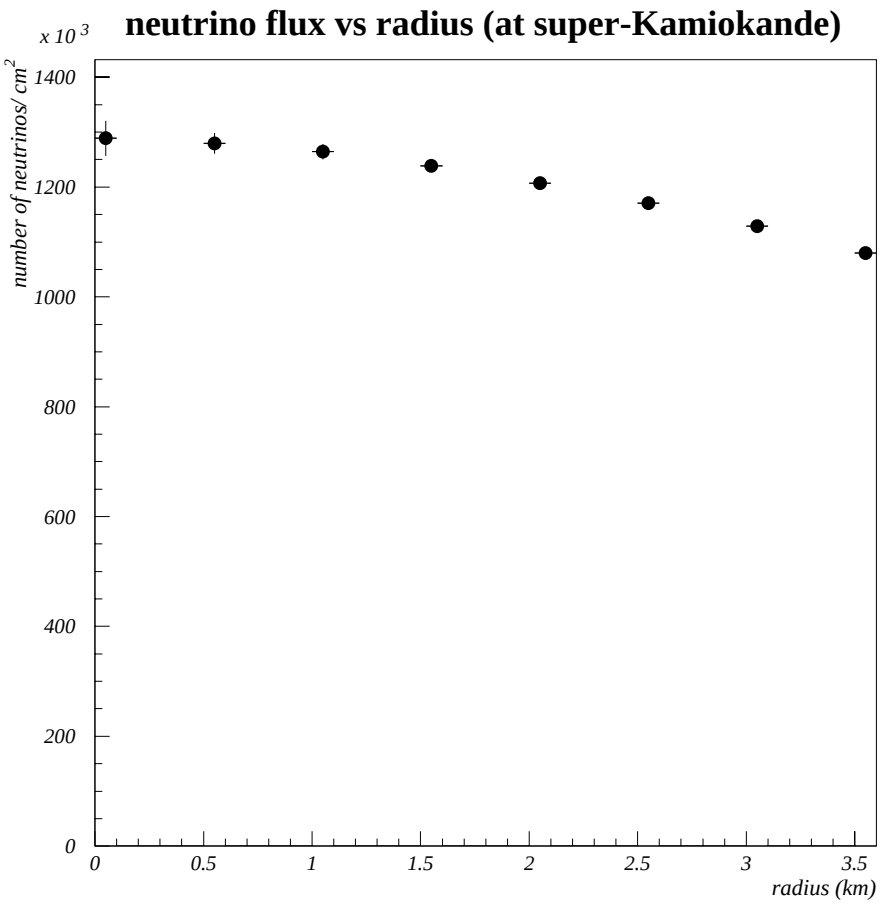

Figure 6.3: Neutrino beam flux around SK in MC (at 10×20 POT). Neutrino flux reduction 1km from axis (4mrad) is within 3%.

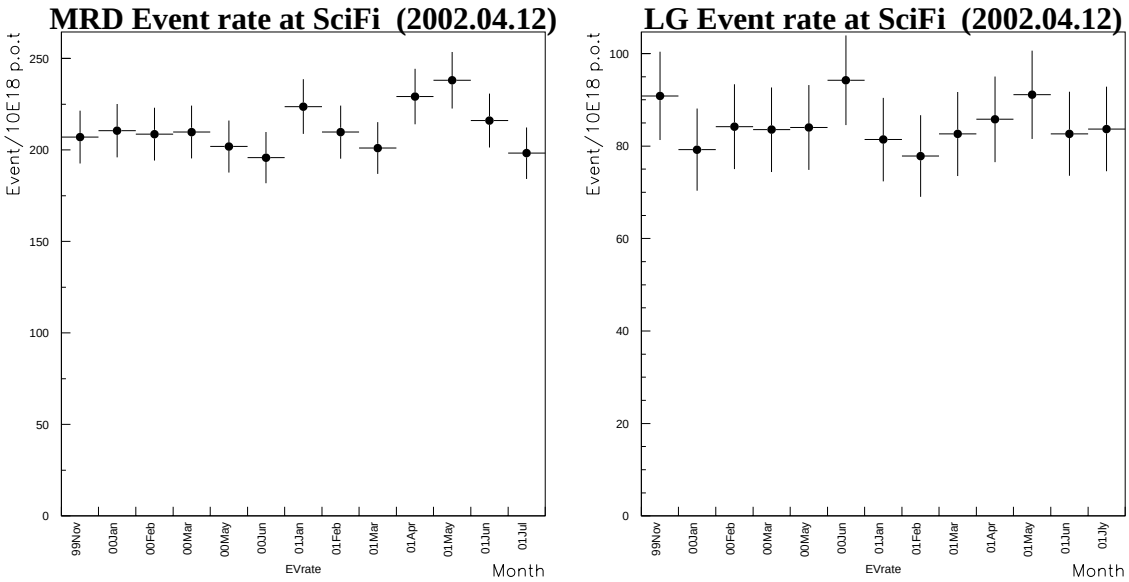

Figure 6.4: SciFi MRD and LG stopping event rate per month normalized by $\mathrm{POT}_{\mathrm{SciFi}}$.

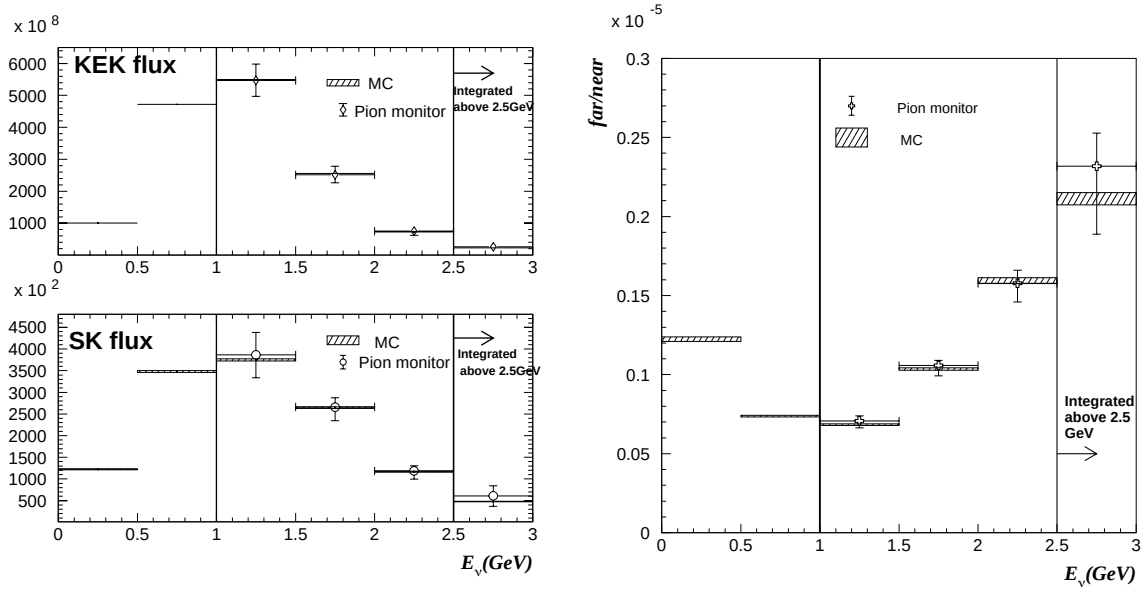

Figure 6.5: Neutrino spectrum (left) and $R_{\mathrm{SK/Near}}$ (right) estimated by pion monitor. MC results (the Cho model) are overlaid. (November configuration)

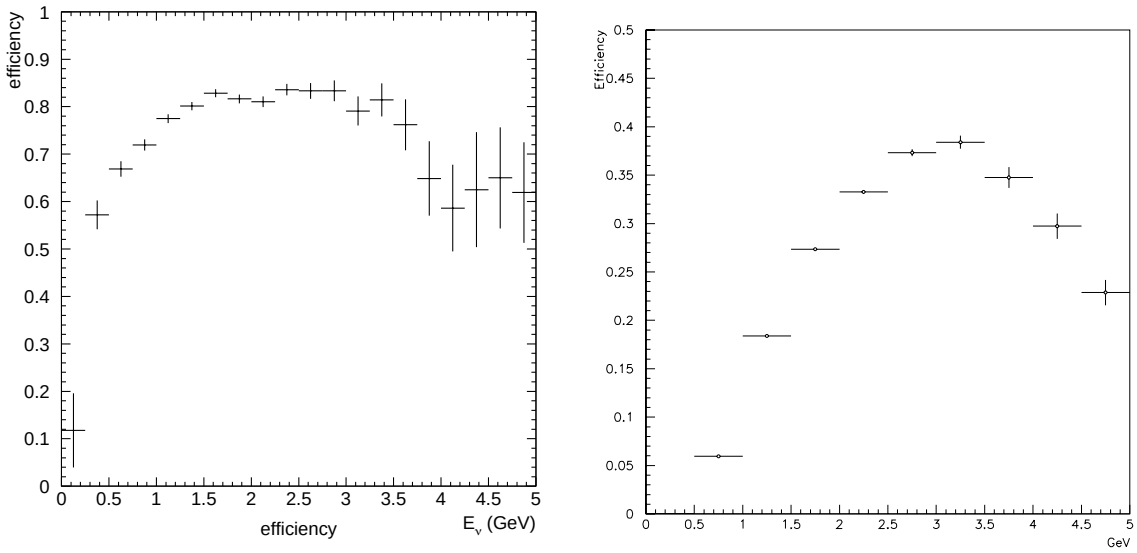

Figure 6.6: SK/SciFi detection efficiency as a function of neutrino energy (GeV).

Chapter 7

Neutrino Energy Spectrum at Near Detector

Oscillation parameters can be determined not only from SK event data but also via spectrum analysis. Spectrum analysis requires the neutrino energy spectrum at the near detector be reconstructed.

7.1 Basic Plots from the SciFi Detector

The muon momentum, the muon production angle with respect to the beam, the number of tracks, and the distribution of vertices are shown for MRD events in Figure 7.1, 7.2, 7.3, and 7.4. The corresponding distributions for LG events are shown in Figure 7.5, 7.6, 7.7, and 7.8. For all plots, dots are data and the histogram is MC. The hatched areas of the histograms represent charged current quasi-elastic (CCQE) interactions in MC. The plots show good MC/data agreement, which suggests we understand the detector and neutrino interaction well.

7.2 Neutrino Energy Reconstruction

For the neutrino spectrum analysis, we need to reconstruct the energy of a mother ν_μ from a daughter muon in our MRD sample. Considering the kinematics, we can reconstruct E_ν in case of a charged current quasi-elastic (CCQE) event

$$\mu + N \rightarrow \nu + p \tag{7.1}$$

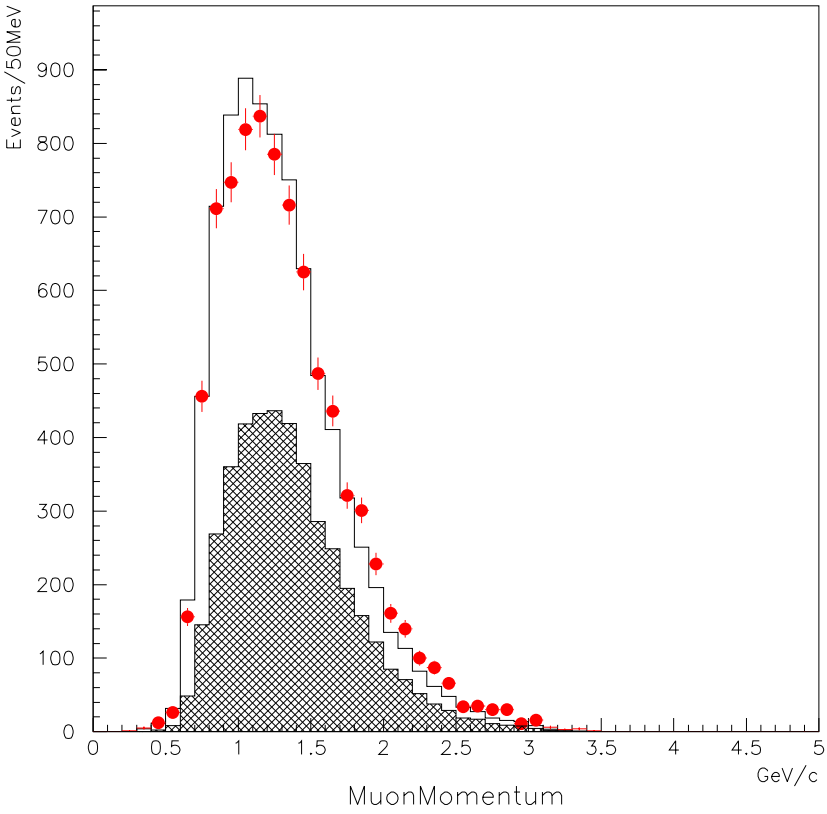

Figure 7.1: P_μ distribution of MRD events.

without regard to proton momentum. The calculation is as follows:

$$\begin{aligned} P_1 + P_2 &= P_3 + P_4 \\ (P_1 + P_2 - P_3)^2 &= P_4^2 \end{aligned} \tag{7.2}$$

where P_1, P_2, P_3 and P_4 are 4-vectors of the incident neutrino, the target neutron, the produced muon, and the recoil proton. Equation 7.2 can be written in the form:

$$(P_1 - P_3)^2 + 2P_2 \cdot (P_1 - P_3) + P_2^2 = P_4^2 \tag{7.3}$$

The right hand side of this:

$$R.H.S. = P_1^2 + P_3^2 - 2P_1 \cdot P_3 + 2(P_2 \cdot P_1 - P_2 \cdot P_3) + P_2^2 \tag{7.4}$$

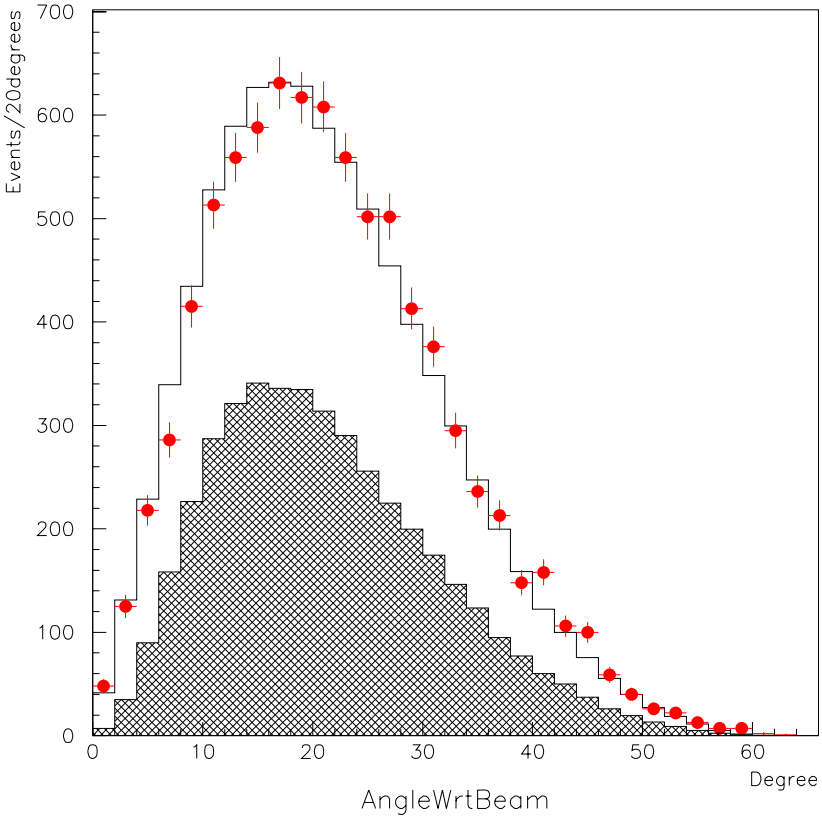

Figure 7.2: θ_μ distribution of MRD events.

$$
\begin{aligned}
&= M_\mu^2 - 2(E_\nu \cdot E_\mu - E_\nu |\vec{P_\mu}| \cos\theta_\mu) + 2(M_n E_\nu - M_n E_\mu) + M_n^2 \\
&= 2E_\nu(-E_\mu + |\vec{P_\mu}| \cos\theta_\mu + M_n) - 2M_n E_\mu + 2M_n E_\mu + M_n^2 + M_\mu^2
\end{aligned}
$$

$$
E_\nu = \frac{M_n E_\mu - M_\mu^2/2}{M_n - E_\mu + P_\mu \cos\theta_l}. \tag{7.5}
$$

M_n, E_μ, P_μ, M_μ, θ_μ are the mass of nucleon, the muon energy, the muon momentum, the mass of muon, and the production angle of muon, respectively.

Because a QE (quasi-elastic) event is a two-body interaction, the daughter muon and the proton are emitted on one plane. From the momentum balance, we can anticipate the direction of the proton. When we observe the second track, we can distinguish if the track comes from the proton or not by comparing the direction of the expected and observed tracks. The expected proton direction is

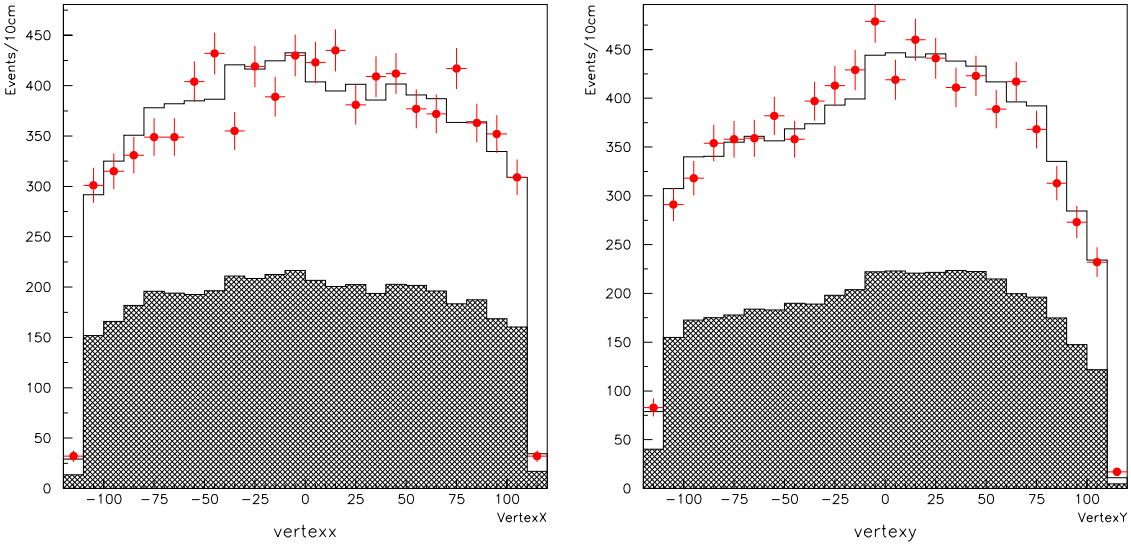

Figure 7.3: Reconstructed MRD-event vertices distribution for X (left), Y (right).

calculated:

$$\vec{P_p} = (-P_{\mu x}, -P_{\mu y}, P_\nu - P_\mu \cos\theta_\mu) \tag{7.6}$$

For the observed second track, we can measure the projected angles θ_{XZ} and θ_{YZ} for the XZ and YZ planes respectively. The unit vectors of their direction are:

$$\vec{P} = (\frac{\tan\theta_{XZ}}{L}, \frac{\tan\theta_{YZ}}{L}, \frac{1}{L}) \tag{7.7}$$

$$L = \sqrt{\tan^2\theta_{XZ} + \tan^2\theta_{YZ} + 1} \tag{7.8}$$

$\Delta\theta$ can be calculated from 7.6 and 7.8:

$$\cos\Delta\theta = \frac{-\tan\theta_{\mu x}\cdot P_{\mu x} - \tan\theta_{\mu x}\cdot P_{\mu x} + P_\nu - P_\mu\cos\theta_\mu}{L\cdot|\vec{P_p}|} \tag{7.9}$$

$\Delta\theta$ will be smaller for QE events than other interaction modes. We can enhance the QE interaction with kinematics information. cos $\Delta\theta$ distribution for all two-track events is shown in Figure 7.9. The dots and the histogram correspond to the data and MC, respectively. The hatched area of the histogram shows QE interactions in MC. In the small $\Delta\theta$ region there are more QE events than we expected. In contrast, the large $\Delta\theta$ region is dominated by non-QE interaction modes.

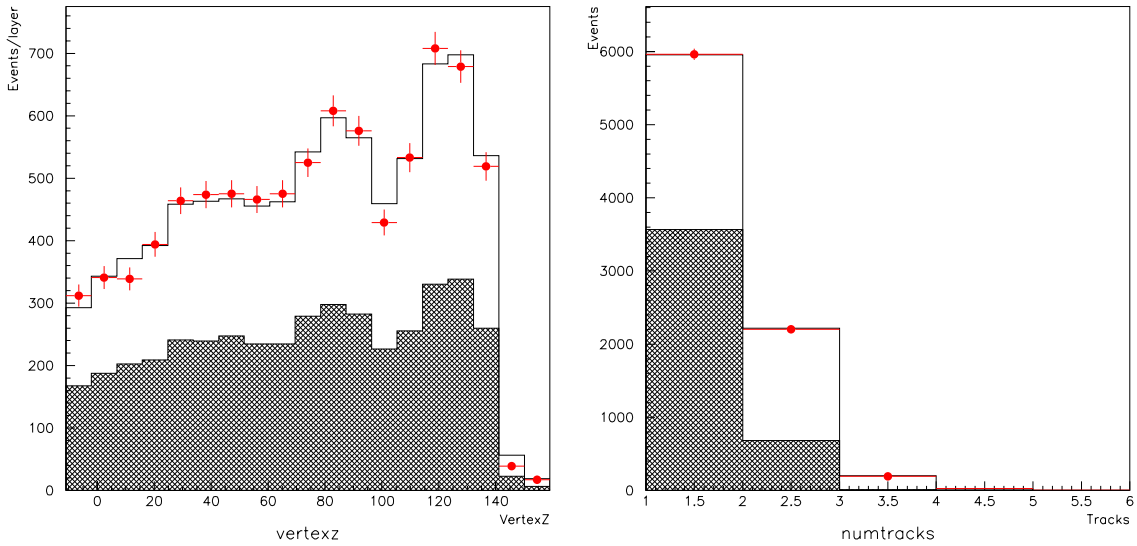

Figure 7.4: Reconstructed event vertices distribution for Z direction (left) and distribution of number of tracks (right). Both plots show MRD sample.

In following analysis, two-track events are divided into two groups: $\Delta\theta \leq 25°$ and $\Delta\theta \geq 30°$. We call these QE samples and non-QE samples. QE samples are 60% CCQE in MC. 85.7% of events in non-QE samples come from interactions other than CCQE. (ex. single meson production mode, see Chapter 4.)

Now we have one-track, two-track QE, and two-track non-QE samples. These three event categories are used to measure the neutrino spectrum and the ratio of the cross section between QE and non-QE interactions.

7.3 Neutrino Energy Spectrum at the Near Detector

The energy spectrum is measured by analyzing muon momentum and angular distributions both in the 1kt water Čerenkov detector (1kt detector) and the SciFi detector. The 1kt detector has a high efficiency for muons with momentum below 1GeV/c and full 4π coverage in solid angle, yet little efficiency for reconstructing muons with momentum above 1.5GeV/c, since the muon exits the detector. The SciFi detector has a high efficiency for measuring muons above 1GeV/c. The

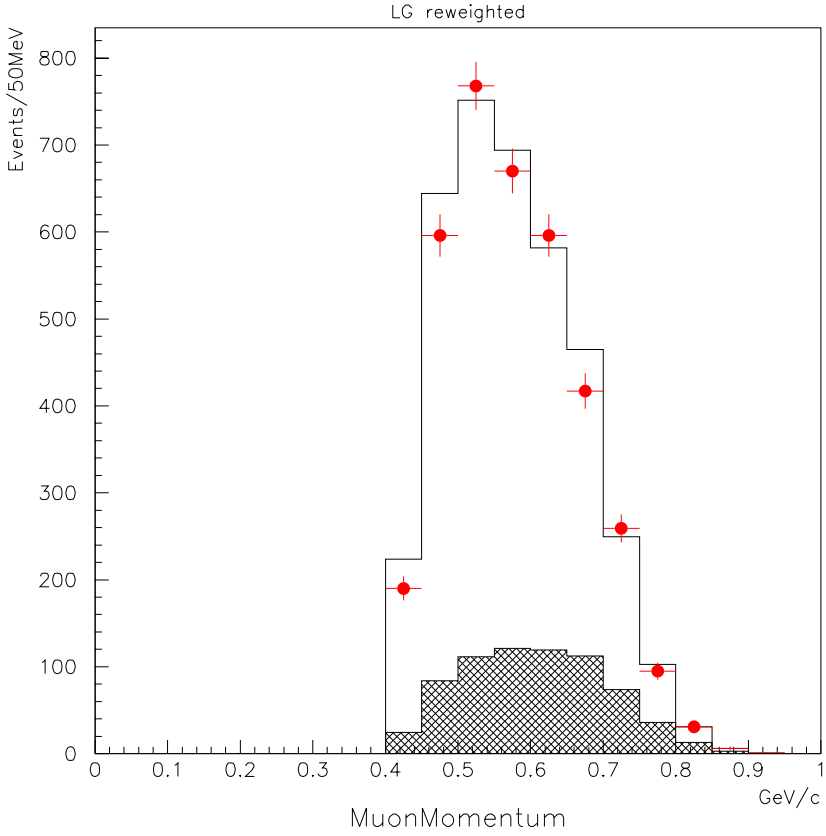

Figure 7.5: P_μ distribution of LG events.

two complementary detectors are thus able to cover the relevant energy range completely.

7.3.1 Neutrino Event Selection at the 1kt Detector

For 1kt detector analysis, the fiducial volume is a 25-ton cylindrical volume that sits lengthwise in the upstream part of the detector. The selection criteria for flux normalization are as follows:

- Good beam selection
  As is described in Subsection 6.1.1. Beam spills in good condition are selected.

- Selection using beam time window

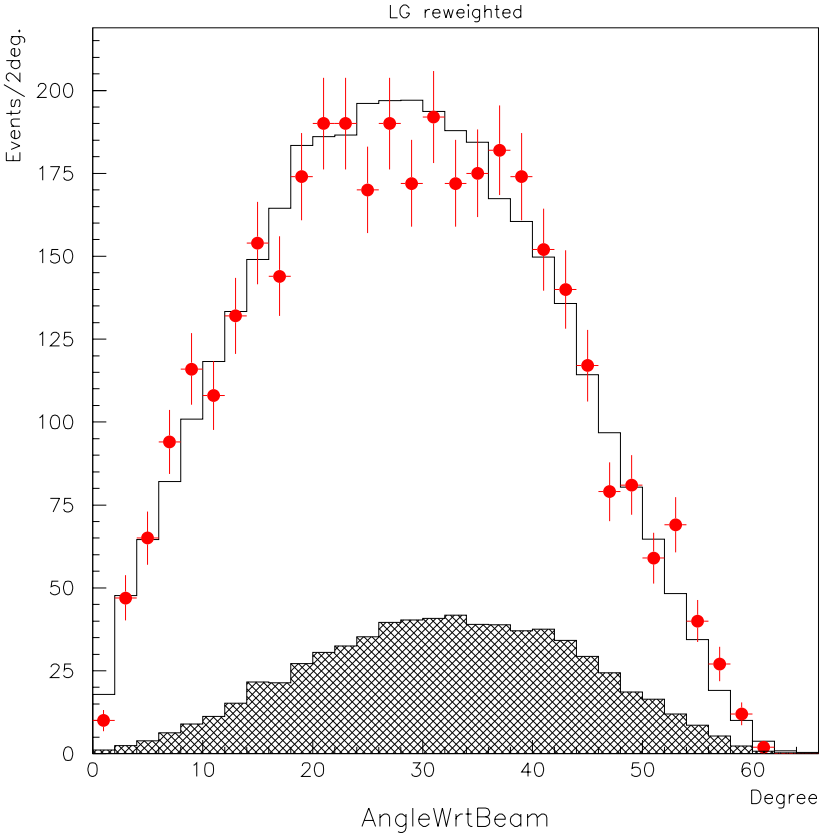

Figure 7.6: θ_μ distribution of LG events.

The 1kt detector is triggered when more than 40 inner PMTs have hits within a 200nsec time window. The triggered events occurring within a 1.1μsec. beam spill are recorded.

- Pre-activity cut
  To avoid fake in-time events caused by reflections off the cables, events with pre-activity within 1.2μsec. of the beam spill are cut.

- Total photo electron cut
  To obtain the sum of all ID PMT, one thousand photoelectrons are required at flash ADC (FADC). This cut is equivalent to an energy deposit of 100MeV.

- Single event selection

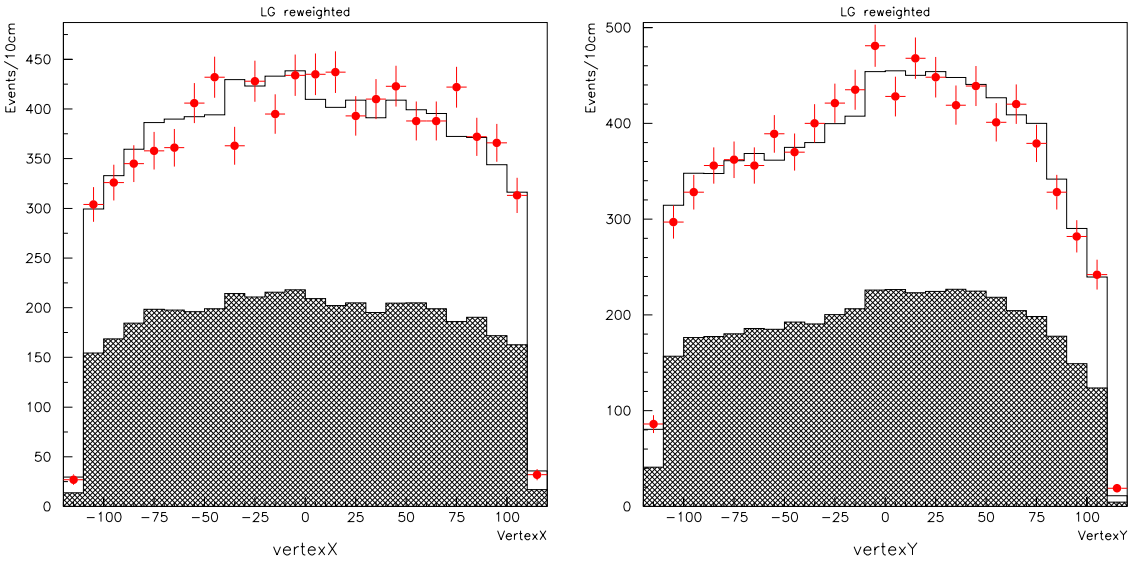

Figure 7.7: Reconstructed LG-event vertices distribution for X (left), Y (right).

Sometimes more than one 1kt event occurs in a 1.1μsec. beam spill (multiple-events). It's difficult to reconstruct the vertex of the multiple events. We rejected events with more than one FADC peak.

- Fiducial volume cut
  The fiducial volume of the 1kt detector used for spectrum analysis is shown in Figure 7.10. The fiducial mass is 25ton for this definition.

The measurement has a 5% systematic uncertainty [67]. The largest contribution is from vertex reconstruction.

For spectrum measurement, events with a one-ring μ are selected from all of events which passed the selection criteria for the flux normalization. The sample is dominated by QE events, as was the case with one-track events in the SciFi detector. Furthermore, to calculate its energy, the muon must be fully contained inside the detector (an FC sample). Muons which meet these criteria are known as "one-ring FC samples". The dominant systematic uncertainty of this spectrum measurement is uncertainty about the energy scale of the detector. The energy scale in the 1kt detector is understood to within $^{+2}_{-3}$ %, which has been confirmed by energy calibration using cosmic rays.

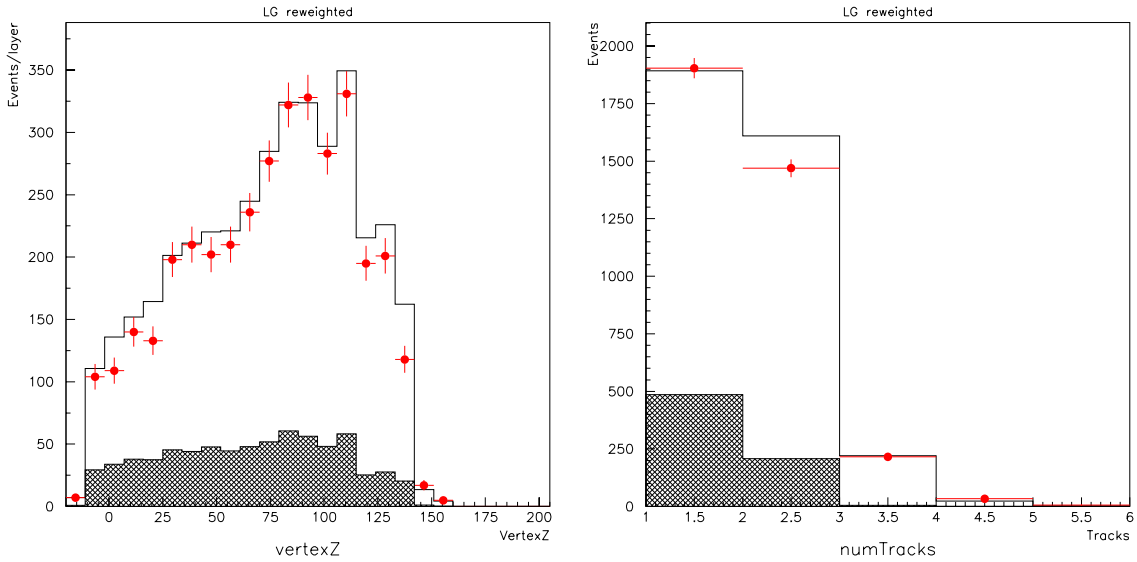

Figure 7.8: Reconstructed LG-event vertices distribution for Z direction (left) and distribution of number of tracks (right). Both plots show LG sample.

7.3.2 χ^2 fitting

The two-dimensional distributions of the muon momentum versus the production angle with respect to the beam of four-event categories (1kt one-ring μ samples, SciFi one-tracks, two-track QEs, and two-track non-QE samples) are used to measure the neutrino energy spectrum. Figure 7.11 shows the distribution of the 1kt detector data.

We use the χ^2 fitting method to compare this data to the MC expectation. The neutrino spectrum is divided into eight energy bins (0-0.5GeV, 0.5-0.75GeV, 0.75-1.0GeV, 1.0-1.5GeV, 1.5-2.0GeV, 2.0-2.5GeV, 2.5-3.0GeV, 3.0GeV-). During the fit, the flux in each energy bin is re-weighted relative to the values in the beam MC. The parameter R_{nqe} is also used to re-weight the ratio between the QE and non-QE cross sections relative to the MC simulation. The systematic uncertainties of the near detectors are also incorporated into the fitting parameter. These are energy scales, track-finding efficiencies, and the detector thresholds. In addition, the spectrum measurement by the pion monitor is used as a constraint on the re-weighting factors.

The value of χ^2 is 227.2/197 D.O.F (degrees of freedom) at the best fit point. Best fit results are summarized in Table 7.1. Measured neutrino energy spectrum

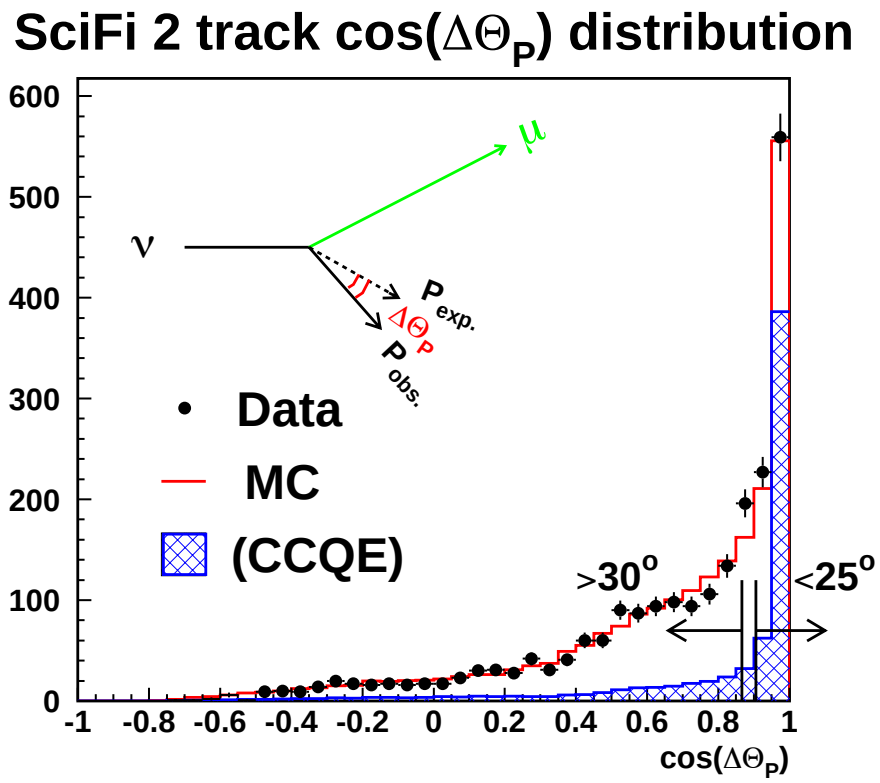

Figure 7.9: cos $\Delta\theta$ distribution for all two-track MRD events. The hatched area shows MC CCQE events. The diagram shows the definition of $\Delta\theta$.

at the near detector is shown in Figure 7.13. All parameters including the detector systematics were found to lie within their expected errors, except R_{nqe} .

Although the fit result for R_{nqe} is 0.93 ± 0.06, the R_{nqe} from the 1kt detector fit alone is 40% lower ($R_{nqe} = 0.73$) than the SciFi detector fit alone ($R_{nqe} = 1.09$). This difference can be attributed to our incomplete knowledge of neutrino-nucleon cross sections. The error on R_{nqe} from the fit is increased to $\pm 20\%$ in order to take this uncertainty into account.

The muon momentum and angular distributions of the one-ring μ samples in the 1kt detector, and the muon momentum distributions of the two-track QE and non-QE samples in the SciFi detector are overlaid with the fitted MC in Figure 7.12. The fit result agrees well with the data.

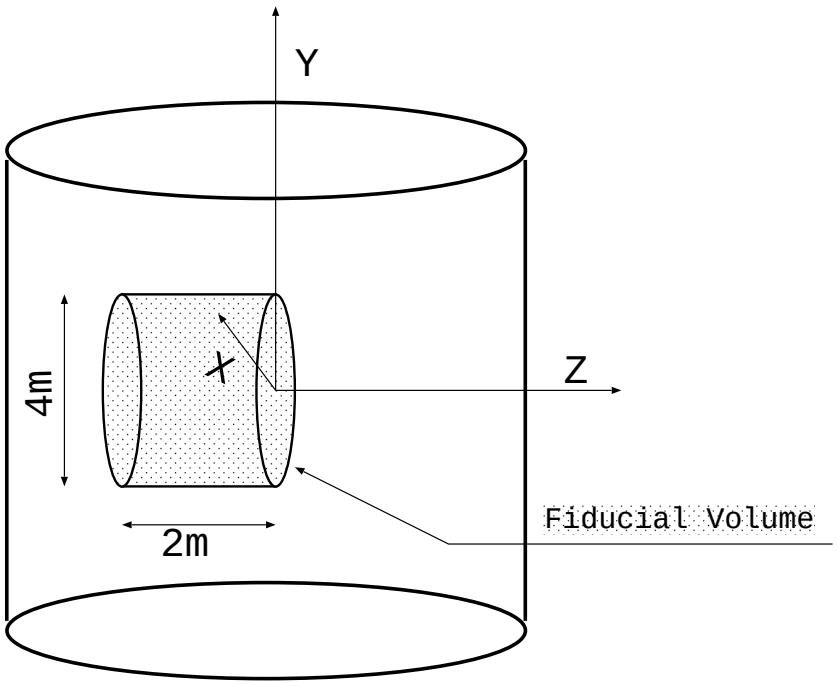

Figure 7.10: Definition of the 25-ton fiducial volume at the 1kt Čerenkov detector.

7.4 Effect of Neutrino Interaction Models on Spectrum Analysis

Changing some parameters, the uncertainty from the neutrino interaction models was studied.

In QE interaction, the axial vector mass M_A (Subsection 4.2.2) was set to a central value of 1.1 GeV/c^2 and varied $\pm 10\%$ in tests. The M_A for single pion production was set at a central value of 1.2 GeV/c^2 and varied $\pm 20\%$. This affected both the q^2 dependence of the cross section and the total cross section. For coherent pion production, two different models were used: one the Rein and Sehgal model [50] and the other a model by Marteau [64]. For deep inelastic scattering, GRV94 [65] and the corrected structure function by Bodek and Yang [66] were studied. The choice of models did not affect the spectrum measurement beyond the size of the fitted errors except for the value of R_{nqe} . The systematic error on R_{nqe} was increased to ± 20 % to take this difference into account.

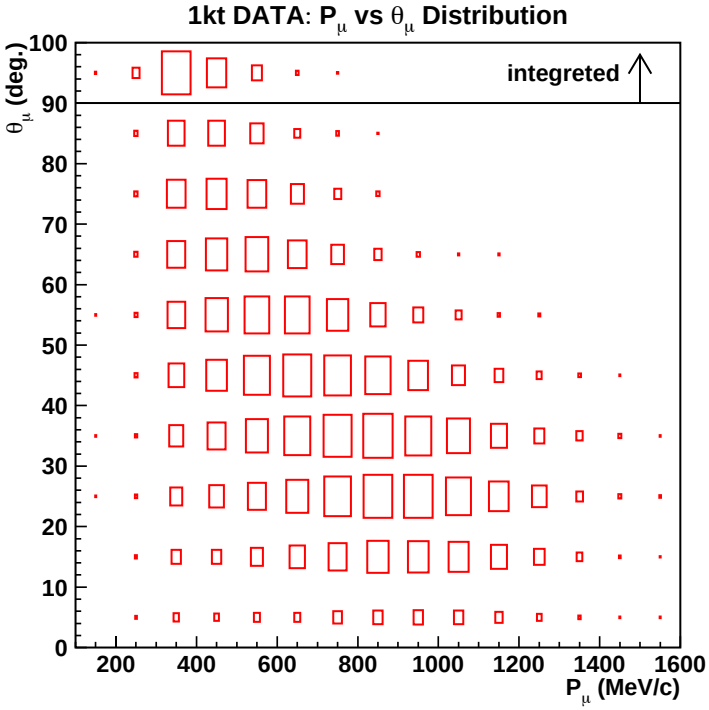

Figure 7.11: Two-dimensional distributions of muon momentum vs. production angle with respect to the beam direction in the 1kt detector.

Table 7.1: Best fit results from spectrum fit of near detector.

E_ν	Fitted flux (R_{nqe}) relative to MC
0.0-0.5	1.3±0.5
0.5-0.75	1.02±0.12
0.75-1.0	1.01±0.09
1.0-1.5	1 (fixed)
1.5-2.0	0.95±0.07
2.0-2.5	0.96±0.08
2.5-3.0	1.18±0.19
3.0-	1.07±0.20
R_{nqe}	0.93±0.20

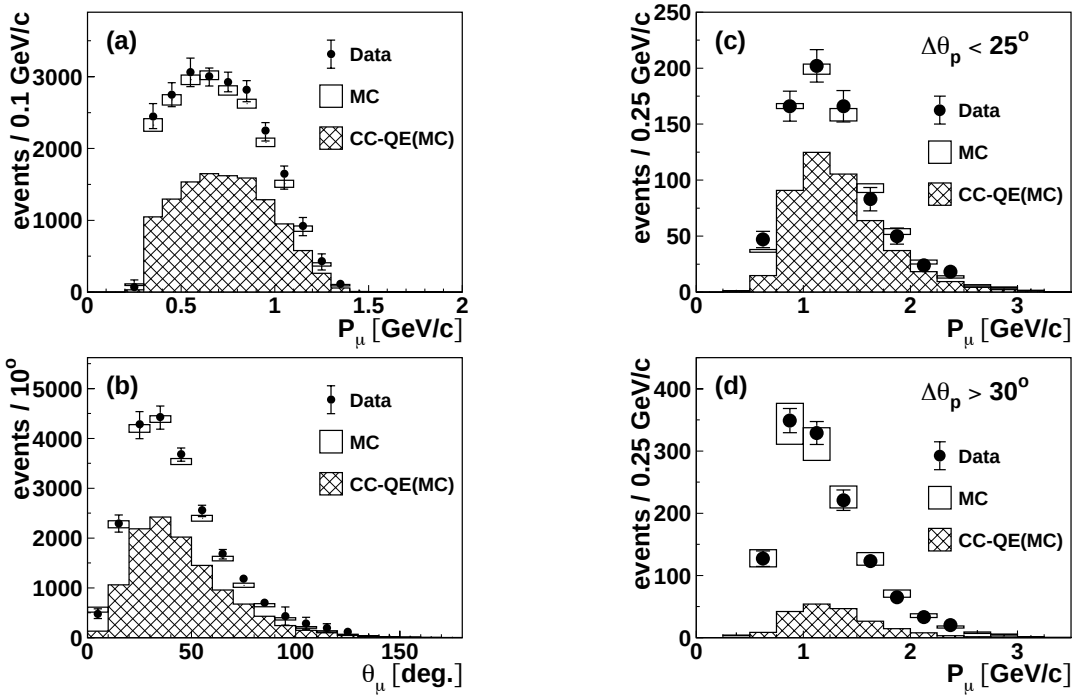

Figure 7.12: (a) The muon momentum distribution of the 1kt detector one-ring μ samples, (b) the angular distribution of the 1kt one-ring μ samples, (c) the muon momentum distribution of the SciFi QE samples, and (d) of the SciFi non-QE samples, The dots are data and the boxes are MC simulation with best fit parameters. The hatched histograms are the CCQE events estimated by the MC simulation.

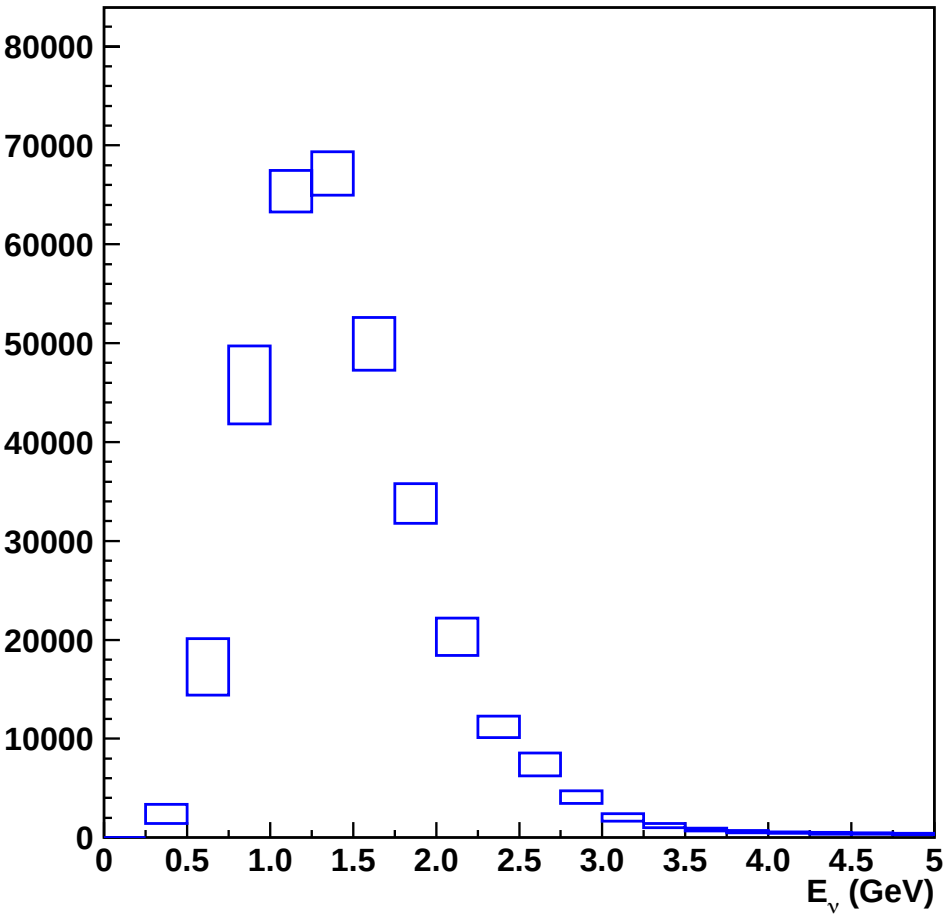

Figure 7.13: Measured neutrino spectrum at near detector.

Chapter 8

Neutrino Events at SK

8.1 Event Selection at Super-Kamiokande

This section describes event selection at SK.

- Rough timing cut
  SK events are selected using timing information from GPS (See Section 2.7). K2K neutrino event selection occurs in a $\pm$ 500 μsec. timing window at beam time. Time difference is defined as follows:

  $$\Delta T \equiv T_{SK} - T_{KEK} - TOF \tag{8.1}$$

  where T_{SK} is the arrival time at SK, T_{KEK} the start time of the beam spill at KEK, and TOF the time of flight from KEK to SK, 833μsec.

- Good beam selection
  As mentioned in subsection 6.1.1, beam spills in good condition are selected.

- Decay electron cut
  If a muon stops in the tank, it decays into an electron and neutrinos:

  $$\mu \rightarrow \mathrm{e} + \nu_{\mu} + \nu_{\mathrm{e}} \tag{8.2}$$

  To avoid this being misidentified as a neutrino event, SK events with activity 30μsec. prior to an event are cut. Dead time factor is less than 1/1000.

- HE (High Energy) trigger
  Hits in the inner detector of more than 31PMTs (corresponds to 50$\sim$100 photoelectrons) in a 200nsec. timing window are triggered.

- Total photo electron cut
  After gain correction of PMTs, The light yield of SK events must be greater than 200 photoelectrons in a 300nsec. timing window (corresponding to a deposit energy of 20MeV).

- OD (outer detector) cut
  SK events must have no activity in the OD to avoid either incoming or outgoing muons. This sample is referred to as the fully-contained (FC) sample.

- 30MeV cut
  We calculate muon energy (or visible energy, E_{vis}) of the FC samples. We require E_{vis} to be greater than 30MeV.

- D-Wall (distance from wall) cut
  Every vertex must be inside the 22.5kton fiducial mass at a distance of 2m or more from the ID wall.

- GPS precise timing cut
  SK events from the K2K neutrino beam must occur within an arrival time window of 1.5 μsec.

The selection efficiency of CC (charged current) interactions is 93%. With the GPS timing cut, approximately 10^{-3} background events caused by atmospheric neutrinos are expected per neutrino event. The procedure is illustrated in Figure 8.1. After reduction, a clear peak can be seen within 1.1 μ sec. of beam spill width and $\pm$ 0.2 μ sec. of GPS precision. Table 8.1 shows the number of events after each cut.

8.2 One-ring μ event

Observed SK events after the above selection are classified by the number of Čerenkov rings in each event. Additionally, particle identification (PID) utilizes Čerenkov ring patterns. Electrons produce electro-magnetic showers. In particular, low-energy electrons exhibit much multiple scattering and produce rather diffuse Čerenkov rings. In contrast to this, muons produce sharp Čerenkov edges, as shown in Figure 8.2.

Table 8.1: Reduced number of events in SK after cuts.

Cut	Number of events
$\pm 500\mu$sec. cut, Decay-e cut	107892
HE Trigger	36560
Total p.e cut	18902
Fully contained	108
$E_{vis} > 30$MeV	100
$-0.2\mu\text{sec.} \leq \Delta T \leq 1.3\mu$sec.	91
$D_{Wall} \geq 2m$	56

8.3 Observed SK Events

From June 1999 to July 2001, 56 FC events were observed after selection. Of these, 30 were one-ring μ events. Figure 8.2 shows a typical one-ring μ SK event. Figure 8.3, 8.4, 8.5 show visible energy, muon momentum, and reconstructed neutrino energy distribution in SK, respectively.

Reconstructed vertices distributions of SK events are shown in Figure 8.6.

The figure includes OD events near the wall. The left figure shows the top view and the right figure the side view with respect to beam direction. The outer circle and box represent the inner detector wall. The inner circle and box represent the fiducial volume boundary. Each circle point shows a reconstructed vertex position. Its line shows the reconstructed particle momentum along the Čerenkov ring. Open circles are events whose vertices fall outside the fiducial volume. Closed circles are events whose vertices lie inside the fiducial volume (FC 56 events, after D_{Wall} cut).

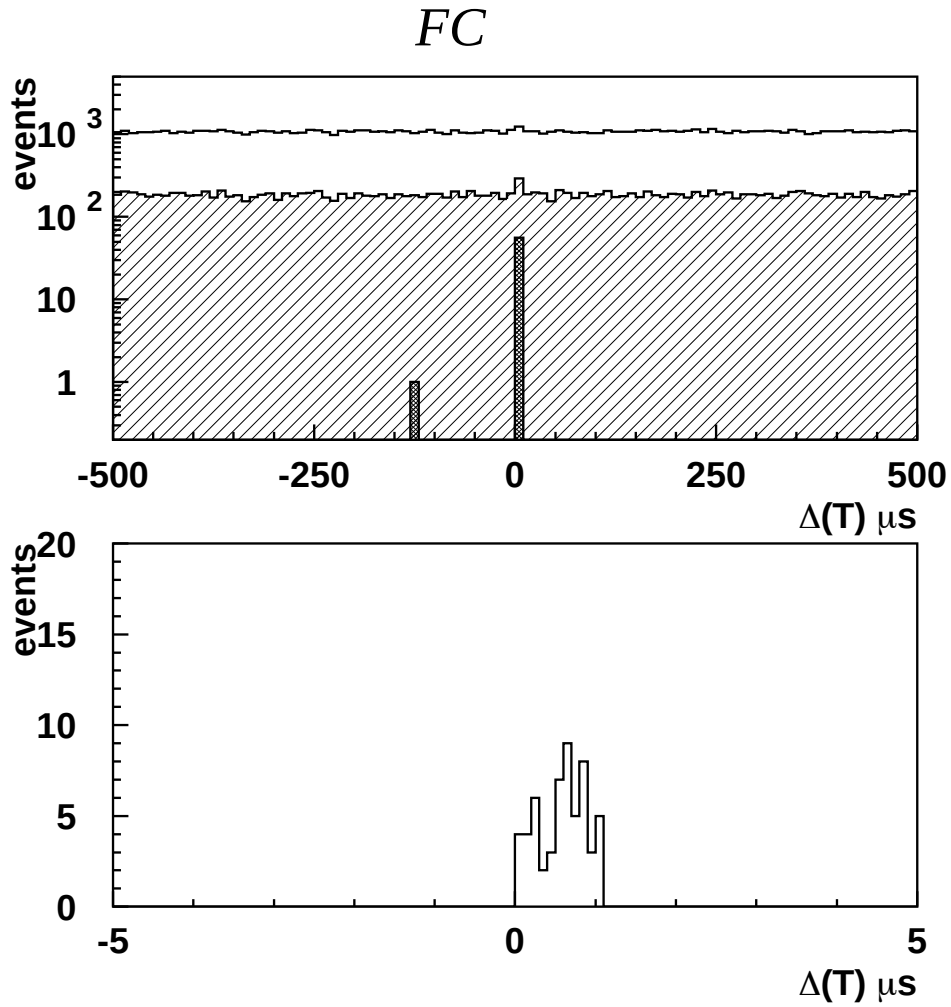

Figure 8.1: Time difference distribution of HE (High Energy) triggered events after decay electron cut (solid line), total photo-electron cut (light hatch), and selected events inside fiducial volume (dark hatch). The upper figure is at ± 500 μsec., the lower figure at ± 5 μsec. A clear peak can be seen within 1.1 μsec. of beam spill width and ± 0.2 μsec. of GPS precision.

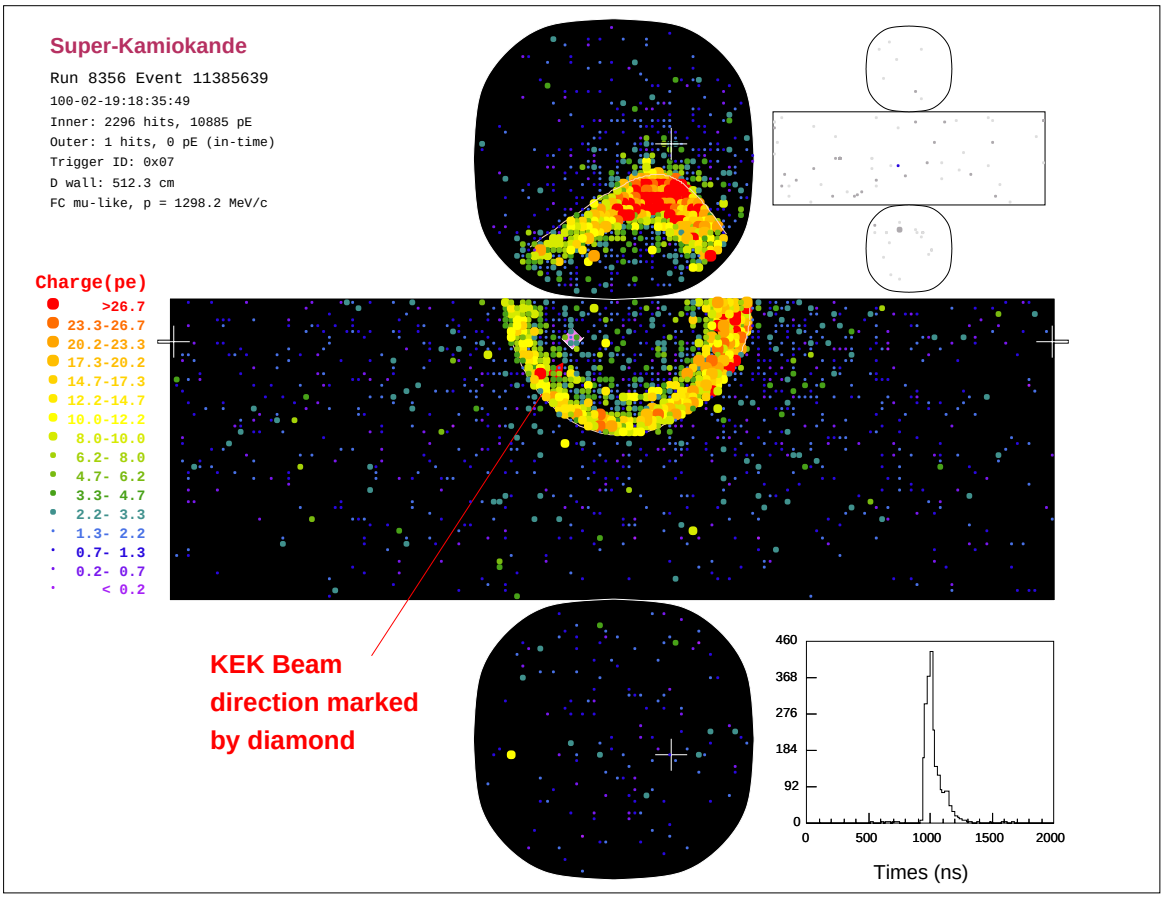

Figure 8.2: Typical neutrino event at SK. The observed charge for each PMT is indicated by the color scale. The black map shows the ID PMTs. The upper white figure shows the OD PMTs. The lower right figure shows the timing distribution in nsec.

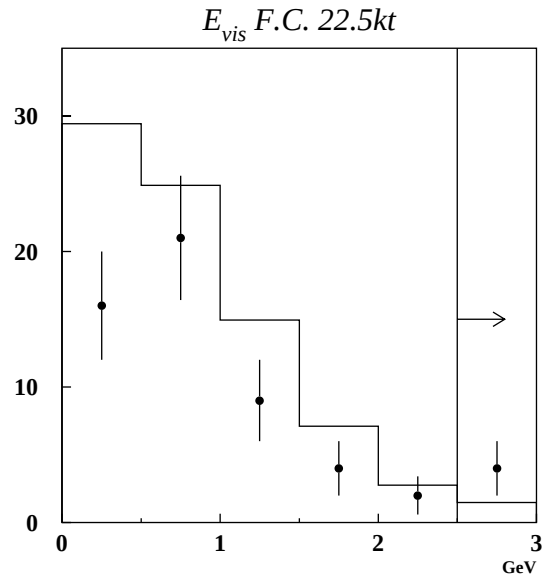

Figure 8.3: Visible energy distribution of SK events.

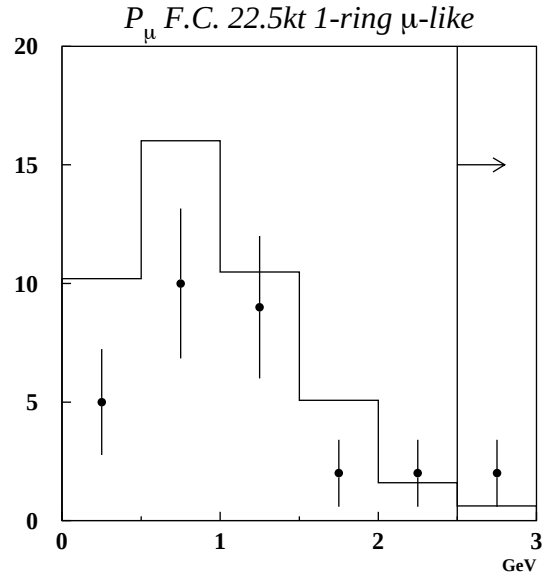

Figure 8.4: Muon momentum distribution of SK events.

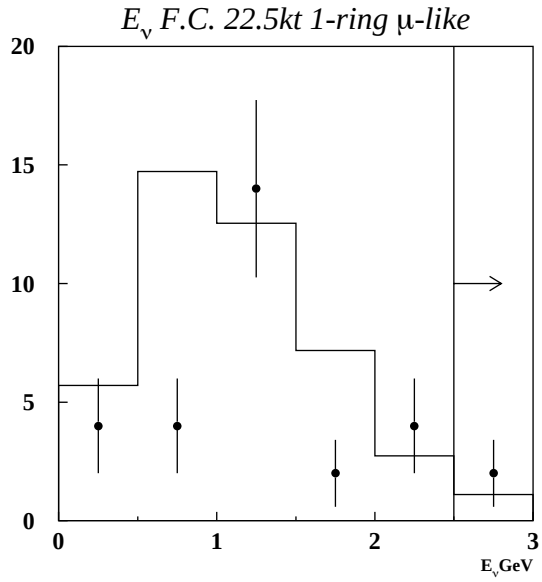

Figure 8.5: Reconstructed neutrino energy distribution of SK events.

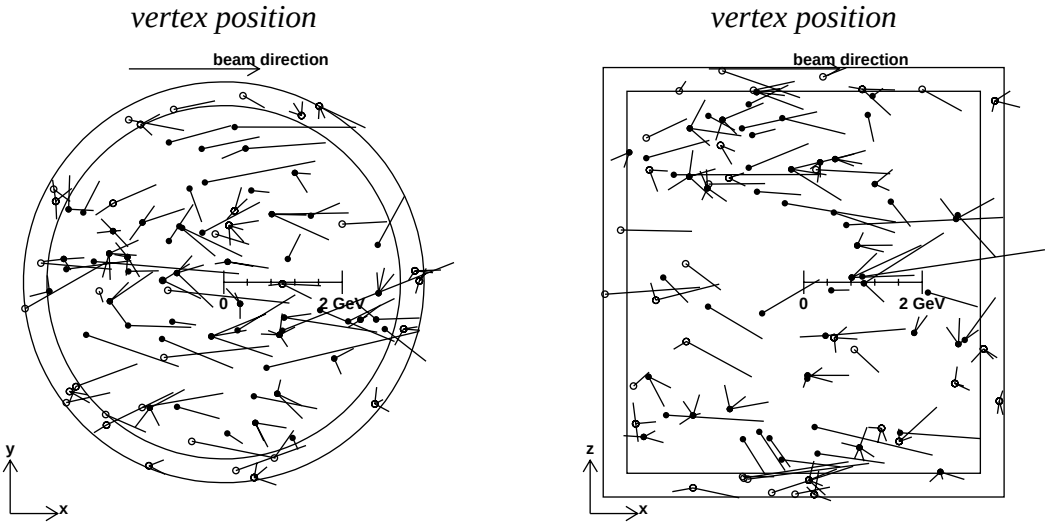

Figure 8.6: Reconstructed vertex distribution of SK events. The left figure shows the top view and the right figure shows the side view with respect to beam direction. The outer circle and box represent the inner detector wall. The inner circle and box represents the fiducial volume boundary. Each circle point shows a reconstructed vertex position. Its line shows the reconstructed particle momentum along the Čerenkov ring. Open circles are events whose vertices fall outside the fiducial volume. Closed circles are events whose vertices fall inside the fiducial volume (FC 56 events after D_{Wall} cut).

Chapter 9

Oscillation Analysis

9.1 Statistical Significance of No Oscillation

Comparing the observed and expected number of fully-contained (FC) events at SK, we can estimate the probability of no oscillation statistically.

With fifty-six FC events observed at SK, we expect $85.9^{+7.9}_{-8.5}$ events at SciFi, assuming no oscillation (Chapter 6). In order to judge this number, the following purely statistical Monte Carlo test is performed.

Poisson distributions are generated repeatedly, which smear the average around 85.9 by a Gaussian function and attach to it an error of ± 8.5 (8.5 is conservative). The probability of this observation is calculated as the integration of the probability of less than or equal to 56 events. The definition of the probability is expressed as follows:

$$P(x \leq n; \mu_0 \pm \Delta\mu) = \frac{\int_0^\infty \sum_{x=0}^{n} \frac{e^{-\mu}\mu^x}{x!} \cdot e^{\frac{-(\mu-\mu_0)^2}{2\Delta\mu}} d\mu}{\sqrt{2\pi\Delta\mu}} \tag{9.1}$$

where n, μ_0, and $\Delta\mu$ are the number of observed events, the center value of the number of expected events, and its error, respectively. In our case, $n = 56$, $\mu_0 = 85.9$, and $\Delta\mu = 8.5$.

By a 10^6 times test, the obtained probability is 0.7% for this observation of 56 events (Figure 9.1). The null-oscillation hypothesis is excluded with a more than 99% C.L. (confidence level).

This result is very consistent with the 1kt Čerenkov detector and the null-oscillation hypothesis is excluded with a more than 99% C.L. for $80.6^{+6.2}_{-5.4}$ events expected.

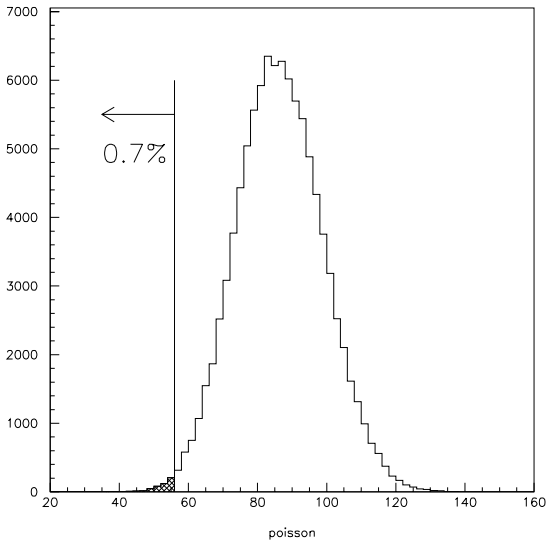

Figure 9.1: A poisson distribution ($\mu_0 = 85.9$, and $\Delta\mu = 8.5$) smeared by Gaussian. By a 10^6 times test, the probability is 0.7% for the observation of 56 events.

9.1.1 KS Test

A Kolgomorov-Smirnov(KS) test of arrival times compared to a random arrival distribution for the FC sample obtains a 43% probability, consistent with constant arrival of neutrinos.

9.2 Maximum-Likelihood Analysis

We also performed a maximum-likelihood analysis to search for the oscillation parameters. The number of FC events and the energy spectrum shape of one-ring μ events are used in the analysis.

The likelihood function is defined as:

$$\mathcal{L} = \mathcal{L}_{norm} \times \mathcal{L}_{shape}. \tag{9.2}$$

The normalization term $\mathcal{L}_{norm}(N_{obs}, N_{exp})$ is the Poisson probability used to observe N_{obs} events when the expected number of events is $N_{exp}(\Delta m^2, \sin^2 2\theta, f)$. The symbol f represents the set of parameters with varied systematic errors during the fit. f consists of the re-weighted neutrino spectrum measured at the near detector (Φ_{near}), the F/N ratio, the reconstruction efficiency (ϵ_{SK}) of SK for one-ring μ events, the re-weighting factor for the CC-QE/non-QE ratio R_{nqe} , the SK

Table 9.1: Percentage of energy dependent systematic errors on the predicted neutrino spectrum at SK.

E_ν GeV	$\Phi_{\rm near}$	$R_{\rm SK/Near}$	$\epsilon_{\rm SK}$
0 - 0.5	37	2.6	8.7
0.5 - 0.75	12	4.3	4.3
0.75 - 1.0	6.7	4.3	4.3
1.0 - 1.5	3.1	6.5	8.9
1.5 - 2.0	4.7	10	10
2.0 - 2.5	8.2	11	9.8
2.5 - 3.0	15	12	9.9
3.0 -	17	12	9.9

energy scale, and the overall normalization. The errors on the first three items are energy dependent and correlated. The diagonal parts of their error matrices are summarized in Table 9.1. The f parameters are treated as fitting parameters with an additional constraint term in the likelihood.

The shape term of likelihood is written as:

$$\mathcal{L}_{shape} = \prod_{i=1}^{N_{1{\rm ring}\mu}} P(E_i; \Delta m^2, \sin^2 2\theta, f). \tag{9.3}$$

This is the product of the probabilities of each one-ring μ event to be observed at the bin of E_i. The reconstructed neutrino energy (E_ν^{rec}) is E_i, P is the normalized E_ν^{rec} distribution estimated by MC, and $N_{1{\rm ring}\mu}$ is the number of one-ring μ events.

We used the whole data sample for the normalization term, i.e. N_{obs}=56. Data taken in June 1999 is discarded for the shape term. This is because in this period the target radius and the horn current were altered and therefore the neutrino spectrum was different; the estimation of correlation in the near detector spectrum and the far/near ratio $R_{\rm SK/Near}$ have not been completed for the June 1999 data. The data in June 1999 correspond to 3.1×10^{18} POT (6.5% of total POT). The number of one-ring μ events from the entire running period is 30. Excluding the June 1999 data, $N_{1-{\rm ring}\mu}$= 29.

The error on R_{nqe} is set to 20%, taking the difference between the 1kt and SciFi detector fit results (subsection 7.3.2). The error on the SK energy scale is 3% [67]. The errors on the normalizations for the June 1999 and subsequent

period data take $^{+1.00}_{-0.85}$% and 5.3%, respectively. Normalization errors do not affect shape part of the likelihood.

The likelihood is calculated at each point in the Δm^2 and $\sin^2 2\theta$ space to find the point where it is maximized. The best fit point in the physical region of the oscillation parameter space is found to be at ($\sin^2 2\theta$, Δm^2)=($1.0, 2.8 \times 10^{-3}$ eV^2). At the best-fit point, the total number of predicted events is 54.2, which agrees within statistical error with the observation of 56. The observed E_ν^{rec} distribution of the one-ring μ sample at SK is shown in Figure 9.2. The expected distribution of the best fit oscillation parameters and the expected spectrum without oscillations are also shown. Consistency between the observed and best-fit E_ν^{rec} spectrum is checked in a KS test, from which a KS probability of 79% is obtained. Both the best fit number of events and the spectrum shape agree with observations.

The allowed regions of oscillation parameters are drawn in Figure 9.3. The 90% C.L. contour crosses the $\sin^2 2\theta = 1$ axis at 1.5 and 3.9×10^{-3} eV^2 for Δm^2 . The allowed regions using only $\mathcal{L}_{norm}$ or $\mathcal{L}_{shape}$ are shown in Figure 9.4. The oscillations parameters preferred by the total flux reduction and the distortion of the energy spectrum agree well.

The best fit oscillation parameters are summarized in Table 9.2.

Table 9.2: Best fit points from the maximum-likelihood analysis. The unit of Δm^2 is 10^{-3} eV^2. Results are shown for the both entire parameter space and for the case where the parameters are constrained to the physical.

	Likelihood Constraint	
	$\sin^2 2\theta$	Δm^2
Shape only	1.0	3.0
(allowing unphysical)	1.09	3.0
Norm + Shape	1.0	2.8
(allowing unphysical)	1.03	2.8

The probability of the observations being due to a statistical fluctuation instead of neutrino oscillation is estimated by computing the likelihood ratio of the best fit point to the null-oscillation case. The null-oscillation probability is

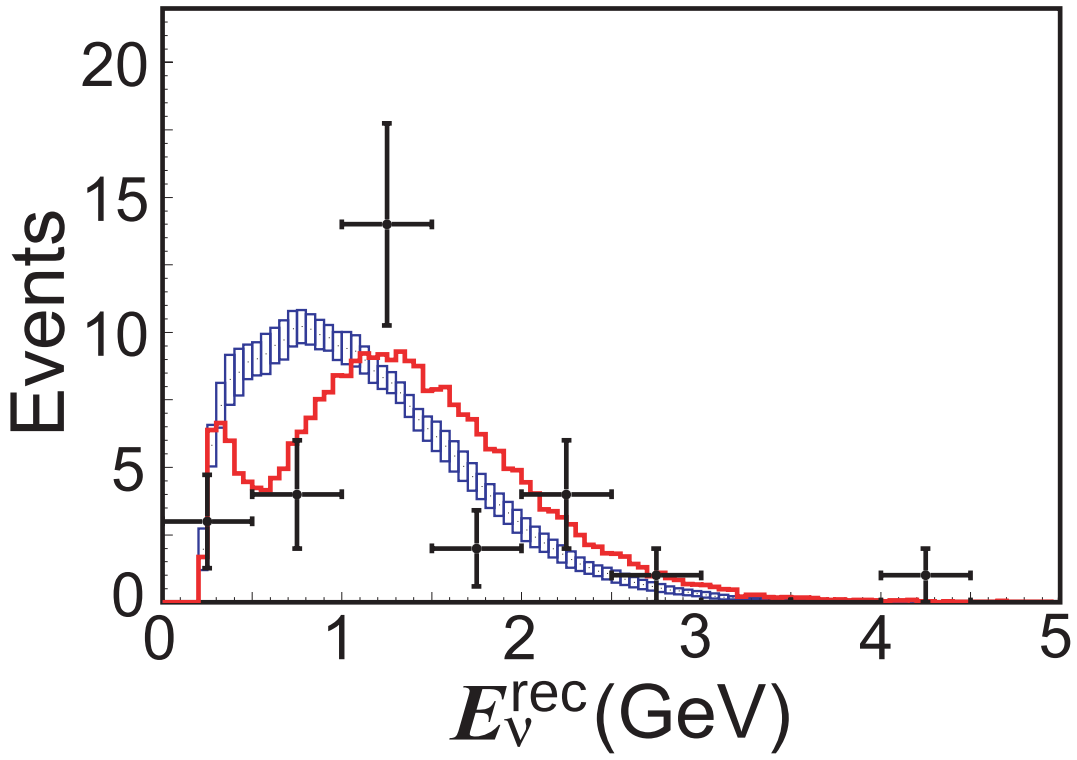

Figure 9.2: The reconstructed E_ν distribution. Dots are observations, the box histogram is the expected spectrum without oscillations. The height of the boxes are the systematic error sizes. The open histogram is the best fit spectrum. The area of both histograms is normalized to the observations.

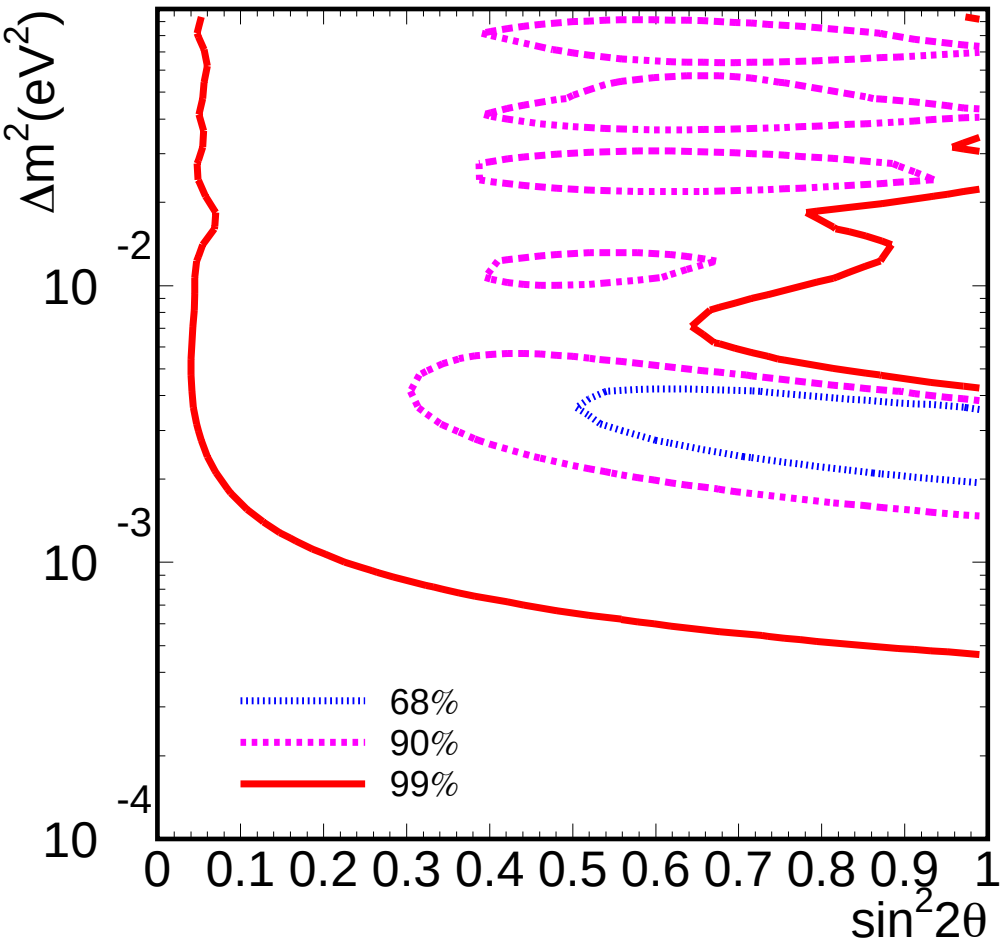

Figure 9.3: Allowed regions of oscillation parameters. The insides of the two solid lines are 99% C.L. The right side of dashed line and the insides of the distorted circles of dashed line are the 90% C.L. The right side of dotted line is 68% C.L.

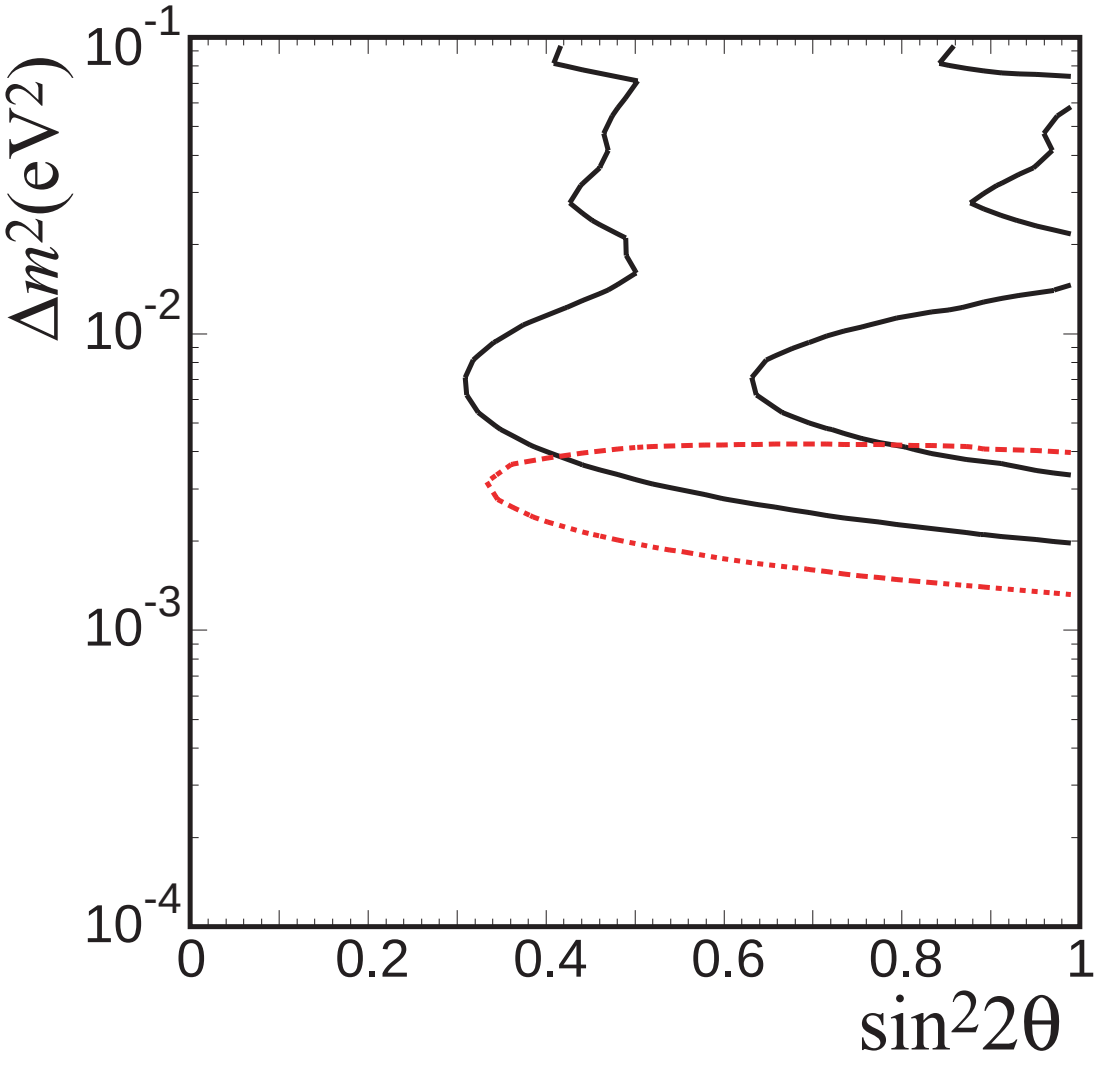

Figure 9.4: Allowed regions (68% C.L.) of oscillation parameters given by normalization only (solid) and shape only (dashed). The inside of the two solid lines and the right side of the dashed curve are the allowed regions.

calculated to be 0.7%. When only normalization (shape) information is used, the probabilities are 1.3% (16%). With the current statistics, the null-oscillation probability is strongly constrained by the normalization part of the likelihood.

The analysis of atmospheric neutrinos at SK (1144day exposure) suggests an allowed region of $\sin^2 2\theta \sim 1$ and $\Delta m^2 \sim 10^{-3} \sim 5 \times 10^{-3} eV^2$ for $\nu_\mu \to \nu_\tau$ mode. Our results are consistent with it.

Finally, study of the uncertainties of neutrino interactions uses the same procedure as spectrum measurement at the near detector. It is found that the effect of interaction model difference on all results is negligible due to cancellation caused by using the same models at both the near detector and SK.

Chapter 10

Conclusion

The SciFi detector, a tracker made of scintillating fiber, was developed as a main component of the near detector for the K2K long baseline experiment. Analysis techniques were also developed for the SciFi detector. The performance of the detector was studied extensively using Monte Carlo simulation.

With the track information from the SciFi detector and the downstream muon chamber, 12317 neutrino events that occurred in the SciFi detector during the three-year K2K run were reconstructed. Combining this with data from the 1kt water Čerenkov detector, we reconstructed the neutrino energy spectrum at the near detector. Fifty-six beam neutrino events were observed at the far detector Super-Kamiokande (SK). The number of events expected at the near detector (the 1kt water Čerenkov detector) is $80.1^{+6.2}_{-5.4}$ without oscillation. Expectation from the SciFi detector data is very consistent with the 1kt detector. Statistical analysis proves the probability of no oscillation is less than 1%.

Additionally, a maximum likelihood analysis of the neutrino energy spectrum was performed. We defined the likelihood function in normalization and spectrum shape terms. All of the 56 neutrino events were used for the normalization terms. The 29 one-ring muon samples were used for the shape terms. Assuming a two-flavor oscillation case, the allowed region of Δm^2 is between 1.5×10^{-3} and 3.9×10^{-3} eV^2 at 90% C.L. at $\sin^2 2\theta = 1.0$, which is consistent with the results of the Super-Kamiokande collaboration using atmospheric neutrinos.

Bibliography

[1] W. Pauli, "Zur älteren un neuen Geschichte des Neutrinos", Collected Papers by W. Pauli, ed. R. Kronig and U.P. Weisskopf (Interscience Pub., N. Y. 1964) Vol. **2**, p.1312.

[2] F. Reines, C. L. Cowan, Jr., Phys. Rev. **92**, 830 (1953).

[3] S. L. Glashow, Nucl. Phys. **22**, 579 (1961).

[4] S. Weinberg, Phys. Rev. Lett. **19**, 1264 (1967).

[5] A. Salam, "Elementary Particle Physics", Nobel Symp. No.8.

[6] Ch. Weinheimer *et. al.*, Phys. Lett. **B460**, 219 (1999).
V. M. Lobashev *et. al.*, Phys. Lett. **B460**, 227 (1999).

[7] K. Assamagan *et. al.*, Phys. Lett. **B335**, 231 (1994).

[8] R. Barate *et. al.*, E. Phys. J. **C2**, 395 (1998).

[9] B. Pontecorvo, Sov. Phy. JETP **10**, 1236 (1960).

[10] M. Nakagawa, H. Okonogi, S. Sakata and A. Toyoda, Prog. Theor. Phys. **30**, 727 (1962).

[11] Particle Data Group, Eur. Phys. J. **C15**, 1-878 (2000),

[12] Particle Data Group, Phys. Rev. **D66**, 1-974 (2002),
`http://pdg.lbl.gov/`

[13] Y. Fukuda *et al.*, Phys. Lett. **B335**, 237 (1994).

[14] R. Becker-Szendy *et al.*, Phys. Rev. **D46**, 3720 (1992).

[15] K. Daum *et al.*, Z. Phys. **C66**, 417 (1995).

[16] M. Agelietta *et al.*, Europhys. Lett. **8**, 611 (1989).

[17] W.W.M. Allison, Phys. Lett. **B391**, 491 (1997).

[18] Y. Fukuda *et al.*, Phys. Rev. Lett. **81**, 1562 (1998).

[19] K. H. Tanaka *et al.*, KEK preprint 91-27.

[20] The PC-CCP interface driver and library is available at `http://neutrino.kek.jp/ kohama/ccp/ccp.html` .

[21] M. Yoshida, Ph.D thesis, Osaka University (2001).

[22] T. Ishii and K2K MRD Group, Nucl. Inst. Meth. **A482**, 244 (2002).

[23] H. G. Berns and R. J. Wilkes, IEEE Trans. Nucl. Sci. **47**, 340 (2000); S. Yamada, Masters thesis, University of Tokyo (1999) *(in Japanese)*.

[24] T. Maruyama, Ph.D. thesis, Tohoku University (2000).

[25] A. Suzuki, H. Park, *et al.*, Nucl. Instr. Meth. **A453**, 165 (2000).

[26] Super-Kamiokande Collaborator, submitted to Nucl. Instr. Meth. A.

[27] S. Echigo, Masters thesis, Kobe University (1998) *(in Japanese)*.

[28] T. Kadowaki, Masters thesis, Science University in Tokyo (1999) *(in Japanese)*.

[29] K. Tashiro, Masters thesis, Kobe University (1998) *(in Japanese)*.

[30] Y. Tanaka, Masters thesis, Kobe University (1998) *(in Japanese)*.

[31] K. Sato, Masters thesis, Kobe University (2000) *(in Japanese)*.

[32] Delft Hitech Inc. "Technical Handbook of the Image Intensifier" (1994) *(in Japanese)*.

[33] M. Onchi, Masters thesis, Kobe University (2000) *(in Japanese)*.

[34] M. Kitamura, Masters thesis, Kobe University (1999) *(in Japanese)*.

[35] H. Park, "SciFi Analysis Manual" (1999) *(unpublished)*.

[36] B. J. Kim, *et, al.*, "Tracking Performance of the Scintillating Fiber Detector in the K2K Experiment", (2002), Submitted to Nucl. Instr. Meth. A, `hep-ex/0206041` .

[37] GEANT–Detector Description and Simulation Tool, Application Software Group, Computing and Networks Division (1993).

[38] Y. Cho, *et, al.*, Phys. Rev. **D4**, 1967 (1971).

[39] J. R. Sanford and C. L. Wang, BNL AGS internal reprots No. BNL11299 and No. BNL11479 (1967);
C. L. Wang, Phys. Rev. Letters **25**, 1068 (1970).

[40] C. H. Llewellyn Smith, Phys. Rep. **3**, 261 (1972).

[41] H. Grabosch *et al.*, Z. Phys. **C41**, 527 (1989).

[42] Particle Data Group, Rev. Mod. Phys. **52**, S1 (1980).

[43] K. Nakamura, *et al.*, Nucl. Phys. **A268**, 381 (1976).

[44] C. H. Albright *et al.*, Phys. Rev. **D14**, 1780 (1976).

[45] K. Abe *et al.*, Phys. Rev. Lett. **56**, 1107 (1986).

[46] D. Rein and L. M. Sehgal, Ann. of Phys. **133**, 1780 (1981).

[47] R. Feynman *et al.*, Phys. Rev. **D3**, 2706 (1971).

[48] M. Hirata *et al.*, Ann. Phys. (N.Y.) **108**, 116 (1977).

[49] Y. Cho *et al.*, Phys. Rev. **D4** 1967 (1971).

[50] D. Rein and L. M. Sehgal, Nucl. Phys. **B233**, 29 (1983).

[51] M. Glück, E. Reya, A. Vogt, Z. Phys. **D57**, 433 (1995).

[52] H. Plothow-Besch CERN Program Library W5051 (1995).

[53] T. Sjöstrand *et al.*, CERN-TH-7112-93 (1994).

[54] S. J. Barish *et al.*, Phys. Rev. **D17**, 1 (1978).

[55] S. Barlag *et al.*, Z.Phys. **C11**, 283 (1982).

[56] Paul Musset and Jean-Pierre Vialle, Phys. Rep. **C39**, 1 (1978).

[57] J. E. Kim *et al.*, Rev. Mod. Phys. **53**, 211 (1981).

[58] L. Salcedo *et al.*, Nucl. Phys. **A484**, 79 (1998).

[59] G. Rowe *et al.*, Phys. Rev. **C18**, 584 (1978).

[60] Baifukan, "Dictionary of Physics".

[61] Alanakyan *et al.*, Phys. Atom. Nucl. **61**, 2 (1998).

[62] T. Iwashita, Masters thesis, Kobe University (2000) *(in Japanese)*.

[63] T. Inagaki, Ph.D. thesis, Kyoto University (2001).

[64] J. Marteau *et al.*, Nucl. Instr. Meth. **A451**, 76 (2000).

[65] M. Gluck, E. Reya, A. Vogt, Z. Phys. **C67**, 433 (1995).

[66] A. Bodek *et al.*, submitted to Nucl. Phys. Proc. Suppl. (2002) `hep-ex/02030` .

[67] S. H. Ahn *et al.*, Phys. Lett. **B511**, 178 (2001).